VACUUM UNIFIED SOLITONIC CONDENSATE THEORY

A Compressible-Fluid Framework Unifying Matter, Forces,
Atomic Structure, Radioactive Decay, Electromagnetic Gauge Theory,
the First-Principles Derivation of the Electron, Proton, and Neutron Rest Masses,
the Topological Derivation of Electric Charge Quantisation,
and the Derivation of the Standard Model Gauge Group
$SU(3) \times SU(2) \times U(1)$

Ibrahim Khalid
Lahore, Pakistan

M. Golebiowski
Poland

June 2026

PREPRINT JUNE 2026
Incorporating the Numerical Computation of C_{core} and the Substrate-Motivated Suppression Mechanism into Section 7A

Abstract

I present the Vacuum Unified Solitonic Condensate Theory (VUSCT), a synthesis and extension of the Vacuum Solitonic Fluid Theory (VSFT) with the compressible-fluid unification programme. The physical vacuum is modelled as a compressible quantum condensate—a medium in which density, pressure, and sound speed vary dynamically—governed by the compressible Euler equations together with a barotropic equation of state. Elementary particles are identified as fundamental topological solitons of this substrate: stable, localised defect configurations whose topological winding numbers constitute the discrete invariants of charge, spin, and baryon number.

The central contributions of this paper are:

- First-principles derivations of the electron rest mass m_e (Section 6), the proton rest mass m_p (Section 7), and the neutron rest mass m_n (Section 8) directly from the substrate ontology. The electron derivation yields $m_e \approx 9.1 \times 10^{-31}$ kg consistent with observation; the proton and neutron derivations are transparent parametrisations (see 7.9 and 8.5).
- A fully numerical treatment of the trefoil curvature integral and Δ_T (Section 7A). The geometric curvature integral $I = \oint \kappa_{\text{geom}}^2\, ds$ is evaluated analytically as $\frac{4\pi}{R}\left[1 + \frac{17}{16}\left(\frac{\xi}{R}\right)^2 + \cdots\right]$, confirmed numerically to eight significant figures. The bending stiffness is derived as $\alpha = \pi\hbar c C_{\text{core}}$ from the Gross–Pitaevskiĭ (GP) functional. Crucially, this paper reports the direct numerical evaluation of C_{core} from the GP radial profile: the integral as originally defined is shown to diverge logarithmically, the correct Roberts–Grant–Fetter bending stiffness is computed numerically as $C_F = 1.6152$, and a substrate-motivated suppression mechanism—Conjecture 1, expressing C_{core} as C_F divided by the product of three independent substrate hierarchy scales—is proposed and shown to reproduce $\Delta_T \approx 0.0943$ against the target value 0.09 to within 4.8%, with zero residual free parameters. This resolves what was an open numerical question, while opening a new, more precisely defined open question.

- Topological derivation of electric charge quantisation (Section 9): electric charge is identified with the conserved topological winding number of the Gross–Pitaevskiĭ order parameter. The fractional charges $Q_u = +2/3$ and $Q_d = -1/3$, proton charge $Q_p = +1$, neutron neutrality $Q_n = 0$, and colour confinement as a topological necessity are derived from the braid-closure constraint on a corrected three-strand link topology (Appendix 10A); the magnitude of the fractional charge unit (1/3) is derived without free parameters, while the specific u/d asymmetry rests on an explicit, falsifiable but currently unproven conjecture. The fermionic (double-valued) character of baryon spin is derived from the same corrected topology; the magnitude $\hbar/2$ follows from the resulting $SU(2)$ representation rather than from an independent substrate calculation, correcting a dimensionally inconsistent claim in the previous edition.
- Derivation of the Standard Model gauge group $SU(3)_c \times SU(2)_L \times U(1)_Y$ (Section 11): each gauge factor emerges from a distinct topological feature of the compressible substrate via a uniform four-step localisation method—identifying the multiplet, establishing global symmetry, promoting to local symmetry, and introducing a compensating gauge connection—presented in the order followed by mainstream field theory texts. $U(1)$ arises from the global phase symmetry of the single-component GP order parameter. $SU(2)$ arises from the two-dimensional spinor representation of the braid group B_3 acting on Hopf-linked strand pairs, which encodes weak isospin doublets, $V - A$ coupling, and the $W^{\pm}/Z^0$ as massive acoustic modes of the condensate. $SU(3)$ arises from the $U(3)$ symmetry of the three-strand GP energy functional, with the $U(1)$ factor accounted for by electromagnetism, leaving $SU(3)$ as the colour group; gluon masslessness, colour confinement via centre-non-trivial Wilson loops, and asymptotic freedom via substrate density depletion near vortex cores are all derived. The group-structure identifications carry no free parameters; the gauge boson mass spectrum and coupling constants carry limitations disclosed in 11.5.
- First-principles derivation of the fine-structure constant α (Section 12): the emergent gauge normalisation constant K is computed from the GP vortex phase stiffness integral, yielding $\alpha = 1/(4\pi K) = 1/137.26$, within 0.16% of the observed value 1/137.036, with no free parameters. This narrows the previously open question about the fine-structure constant to the 0.16% level.

Contents

1 Introduction and Motivation

The two pillars of modern physics—quantum field theory and general relativity—share a common pathology: both treat the vacuum as a secondary object, either an inert geometric backdrop or an abstract state of a field theory defined on that backdrop. The consequences are well known:

- the cosmological constant discrepancy spanning 120 orders of magnitude;
- the non-renormalisability of perturbative quantum gravity;
- the unexplained hierarchy of fermion masses, with no first-principles account of why $m_e \approx 9.109 \times 10^{-31}$ kg;
- the unresolved origin of fractional quark charges: the Standard Model assigns $Q_u = +2/3$ and $Q_d = -1/3$ by measurement, offering no explanation for the thirds;
- the absence of a unified substrate account of atomic structure.

The Vacuum Unified Solitonic Condensate Theory (VUSCT) treats the vacuum as primary—a real, compressible, quantum-condensate medium whose dynamics at different scales of resolution produces every observed fundamental phenomenon. Six foundational commitments drive this presentation:

1. The vacuum substrate is compressible. Density, pressure, and sound speed vary dynamically in response to solitonic defects.
2. Elementary particles are fundamental topological solitons. Their stability is topological; charge, mass, and spin all follow from the soliton configuration.
3. The electron, proton, and neutron masses are derived, not postulated. Closed self-consistency equations (Sections 6–8) yield m_e, m_p, and m_n directly from the substrate equation of state—subject, for the proton and neutron, to the fitting limitations disclosed in 7.9 and 8.5.
4. Electric charge quantisation is topological. The conserved winding number of the GP order parameter is charge; braid-closure constraints on three-strand composites force fractional values of $\pm 1/3$ and $\pm 2/3$ without additional postulate (Section 9).
5. The Standard Model gauge group is derived from substrate topology. $U(1)$ emerges from the GP phase symmetry; $SU(2)$ from the braid group algebra of Hopf-linked strand exchanges; $SU(3)$ from the maximal unitary symmetry of the three-strand GP energy functional. Their product structure follows because the three symmetries act on mutually orthogonal subspaces of the strand configuration space (Section 11).
6. Atoms are cosmic knot structures. Each atom corresponds to a specific topological knot class. Radioactive decay is spontaneous topological fragmentation.

The paper is organised as follows. Section 2 traces the historical lineage. Section 3 states the compressible axiomatic foundation. Sections 4 and 5 establish the soliton particle spectrum and matter–antimatter structure. Sections 6–8 derive the three fundamental rest masses, with Section 7A providing the fully numerical treatment of the proton's topology-renormalisation term Δ_T. Section 9 derives electric charge quantisation and fractional quark charges from braid topology. Section 10 derives the Maxwell equations. Section 11 derives the complete Standard Model gauge group $SU(3)_c \times SU(2)_L \times U(1)_Y$ from substrate topology using a uniform localisation approach, including gluon masslessness, asymptotic freedom, $W^{\pm}/Z^0$ mass generation, and parity violation. Section 12 addresses the fine-structure constant. Section 13 derives the gauge structure formally. Section 14 addresses Lorentz invariance. Section 15 derives gravity. Sections 16–17 develop cosmic knot atomic theory and radioactive decay. Sections 18–21 cover nuclear forces, unification, the ontological map, and open problems. Section 22 lists falsifiable predictions, and Section 23 concludes.

2 Historical Foundations and Lineage

The substrate ontology of the VUSCT descends from the oldest continuously articulated programme in natural philosophy: the Vedic identification of *ākāśa* as the pervasive medium of manifestation, the Stoic *pneuma* as a tensional elastic fluid, Descartes's mechanical vortex cosmology, and Newton's aetherial medium in the *Opticks* Queries—these are successive articulations of the same underlying thesis.

MacCullagh (1839). James MacCullagh demonstrated that a rotationally elastic aether reproduces all observed optical phenomena and is mathematically identical to what we now call Maxwell's equations, written twenty-two years before Maxwell. Crucially, the MacCullagh aether predicts a null result for the Michelson–Morley experiment.

Helmholtz and Kelvin (1858–1867). In 1858 Helmholtz proved the fundamental theorems of vortex motion: in an inviscid fluid, vortex filaments are topologically permanent, circulation is conserved along material loops, and the knotting and linking of vortex lines are invariants of the dynamics. In 1867 Lord Kelvin proposed the vortex-atom hypothesis: atoms are knotted vortex filaments in the aether, with different knot types corresponding to different chemical elements. Tait invented knot theory to catalogue these configurations.

Compressible extension: Kambe (2010). The compressible extension was pioneered by Kambe [10], who demonstrated that the compressible Navier–Stokes equation generates Maxwell-like field equations with density-dependent coefficients, correctly handling acoustic-electromagnetic coupling absent in the incompressible treatment.

Soliton field theory: Faddeev–Niemi (1997), Eto–Hamada–Nitta (2025). The cosmic-knot interpretation of atomic structure extends Kelvin's programme with the full apparatus of modern soliton field theory [5, 4].

Laboratory analogues. Laboratory confirmations of the analogue-gravity programme include: Steinhauer's observations of quantum Hawking radiation in BEC systems [19, 14]; Drori et al.'s optical analogue Hawking radiation [2]; and Vančara et al.'s rotating curved-spacetime signatures from a giant quantum vortex in superfluid helium [20].

2.1 From Incompressible to Compressible: A Methodological Note

The incompressible Euler equation $\nabla \cdot \mathbf{v} = 0$ implicitly assumes infinite sound speed, which cannot accommodate a finite, universal signal speed. Every prior vortex-aether theory inherited this defect silently. The compressible reformulation removes it at the level of the axioms: a finite sound speed is built in from the outset, and the identification $c_s(\rho_{\text{bg}}) = c$ is not an additional postulate but a direct reading of the substrate's dynamical structure.

A second benefit is genuine internal energy storage: compression energy converts the logarithmically divergent kinetic contribution into a finite, calculable rest mass through the self-consistency closure $R \to \lambda_{\text{Compton}}$.

3 Axiomatic Foundation: The Compressible Vacuum Substrate

3.1 Vacuum Energy and Variable Density

Quantum field theory establishes a nonzero vacuum energy density $\varepsilon_0 > 0$. By mass–energy equivalence:

$$\rho_{\text{bg}} = \frac{\varepsilon_0}{c^2}. \tag{1}$$

The substrate density fluctuates about this equilibrium value:

$$\rho(\mathbf{x}, t) = \rho_{\text{bg}} + \delta\rho(\mathbf{x}, t). \tag{2}$$

3.2 Compressible Euler Equations and Equation of State

$$\frac{\partial \rho}{\partial t} + \nabla \cdot (\rho \mathbf{v}) = 0, \tag{3}$$

$$\rho \left(\frac{\partial \mathbf{v}}{\partial t} + (\mathbf{v} \cdot \nabla)\mathbf{v} \right) = -\nabla P. \tag{4}$$

Closed by the barotropic polytropic relation:

$$P(\rho) = P_{\text{bg}} + c_s^2(\rho - \rho_{\text{bg}}) + \frac{\gamma - 1}{2} \frac{c_s^2}{\rho_{\text{bg}}} (\rho - \rho_{\text{bg}})^2 + \cdots \tag{5}$$

3.3 Sound Speed, Mach Number, and the Speed of Light

$$c_s(\rho) = \sqrt{\frac{dP}{d\rho}}. \tag{6}$$

At equilibrium:

$$c_s(\rho_{\text{bg}}) = c. \tag{7}$$

The local Mach number of a moving soliton is $M = |\mathbf{v}_{\text{soliton}}|/c_s(\rho)$.

3.4 Quantum Order Parameter and Quantised Circulation

$$\Psi(\mathbf{x}, t) = \sqrt{\rho(\mathbf{x}, t)}\, e^{i\varphi(\mathbf{x}, t)}, \tag{8}$$

$$\mathbf{v}_s = \frac{\hbar}{m_{\text{eff}}} \nabla \varphi, \tag{9}$$

$$i\hbar \frac{\partial \Psi}{\partial t} = \left(-\frac{\hbar^2 \nabla^2}{2m_{\text{eff}}} + g|\Psi|^2 - \mu \right) \Psi. \tag{10}$$

Single-valuedness of Ψ quantises the circulation:

$$\Gamma \equiv \oint \mathbf{v} \cdot d\boldsymbol{\ell} = n\kappa, \qquad \kappa = \frac{h}{m_{\text{eff}}}, \qquad n \in \mathbb{Z}. \tag{11}$$

The compressible vorticity transport equation:

$$\frac{\partial \boldsymbol{\omega}}{\partial t} = \nabla \times (\mathbf{v} \times \boldsymbol{\omega}) - \frac{1}{\rho} \nabla \rho \times \nabla P. \tag{12}$$

The second term—the baroclinic torque—is absent in the incompressible limit.

3.5 The Gross–Pitaevskiĭ Functional: Variational Structure

The entire axiomatic framework rests on the Gross–Pitaevskiĭ energy functional

$$E[\Psi] = \int d^3x \left[\frac{\hbar^2}{2m_{\text{eff}}} |\nabla \Psi|^2 + \frac{g}{2} |\Psi|^4 - \mu |\Psi|^2 \right], \tag{13}$$

where $g > 0$ is the self-interaction coupling. Varying with respect to Ψ^* yields the GP equation (10). The Madelung transformation $\Psi = \sqrt{\rho}\, e^{i\varphi}$ converts (13) into a sum of kinetic, quantum-pressure, and interaction terms:

$$E[\rho, \varphi] = \int d^3x \left[\frac{\hbar^2}{2m_{\text{eff}}} \left(\frac{(\nabla\rho)^2}{4\rho} + \rho (\nabla\varphi)^2 \right) + \frac{g}{2}\rho^2 - \mu\rho \right]. \tag{14}$$

The first term inside the large bracket is the quantum pressure (Bohm potential), the second is the superfluid kinetic energy, and the third is the nonlinear interaction. Crucially, in the limit where density gradients are slow compared to the coherence length ξ, the quantum-pressure term is suppressed by $(\xi/L)^2$ relative to the kinetic term for a structure of size L, and the GP functional reduces to classical compressible fluid dynamics. This establishes the axiomatic bridge between the microscopic GP equation and the macroscopic Euler equations (3)–(4).

3.5.1 Derivation of the Equation of State from the GP Functional

The equilibrium condition $\delta E/\delta\rho = 0$ at constant μ gives the local equation of state:

$$\mu = -\frac{\hbar^2}{2m_{\text{eff}}} \frac{\nabla^2 \sqrt{\rho}}{\sqrt{\rho}} + g\rho, \tag{15}$$

which is the time-independent GP equation in the Madelung basis. In the spatially uniform background ($\nabla\rho_{\text{bg}} = 0$), so:

$$\mu = g\rho_{\text{bg}} \implies P_{\text{bg}} = \frac{g}{2}\rho_{\text{bg}}^2. \tag{16}$$

Expanding about ρ_{bg}:

$$P(\rho) = \frac{g}{2}\rho_{\text{bg}}^2 + g\rho_{\text{bg}}(\rho - \rho_{\text{bg}}) + \frac{g}{2}(\rho - \rho_{\text{bg}})^2 + \cdots \tag{17}$$

which matches the polytropic relation (5) with $c_s^2 = g\rho_{\text{bg}}/m_{\text{eff}}$ and $\gamma = 2$ for a weakly interacting Bose gas. The identification $c_s(\rho_{\text{bg}}) = c$ then fixes:

$$g = \frac{m_{\text{eff}} c^2}{\rho_{\text{bg}}}. \tag{18}$$

This is the unique self-consistency condition linking the GP coupling g to the Planck-substrate parameters $(m_{\text{eff}}, \rho_{\text{bg}}, c)$, with no free parameter.

3.5.2 The Coherence Length as the Fundamental UV Scale

The coherence length

$$\xi = \frac{\hbar}{\sqrt{2m_{\text{eff}}\, g\, \rho_{\text{bg}}}} = \frac{\hbar}{\sqrt{2}\, m_{\text{eff}}\, c} \tag{19}$$

is the scale below which quantum pressure resists density depletion. With $m_{\text{eff}} = m_{\text{Pl}}$ and $c = c$, this is precisely the Planck length ℓ_{Pl}. The coherence length therefore serves simultaneously as the UV regulator of the substrate's quantum field theory and as the minimum resolvable length scale in the VUSCT programme.

3.6 Substrate Thermodynamics and the Grand Canonical Ensemble

The GP functional (13) arises naturally from the grand canonical free energy of a dilute Bose gas at zero temperature. The grand potential is:

$$\Omega[\Psi] = E[\Psi] - \mu N[\Psi], \qquad N[\Psi] = \int d^3x\, |\Psi|^2 = \int d^3x\, \rho, \tag{20}$$

where μ is the chemical potential and N is the total substrate "atom" number. The saddle point of Ω with respect to Ψ^* reproduces the GP equation. This thermodynamic framing has three consequences:

Phase coherence across the substrate. The condensate fraction approaches unity at $T \to 0$, guaranteeing that the order parameter Ψ is well defined across macroscopic distances. The VUSCT vacuum is therefore a Bose–Einstein condensate occupying all of three-dimensional space.

Compressibility. The compressibility of the condensate,

$$\kappa_T = \frac{1}{\rho_{\rm bg}} \frac{\partial \rho_{\rm bg}}{\partial \mu}\bigg|_T = \frac{1}{g\rho_{\rm bg}^2}, \tag{21}$$

is finite and nonzero. This is the key property distinguishing VUSCT from earlier incompressible aether models: the substrate can be locally compressed or rarefied by the presence of solitonic defects.

Stability. The GP ground state is thermodynamically stable for $g > 0$ (repulsive self-interaction), since the grand potential is bounded below.

3.7 Linear Perturbation Theory: Bogoliubov Spectrum

To understand the spectrum of small excitations about the background condensate, write $\Psi = \sqrt{\rho_{\rm bg} + \delta\rho}\, e^{i\delta\varphi}$ and linearise the GP equation. The result is the Bogoliubov dispersion relation:

$$\omega^2(\mathbf{k}) = c_s^2 k^2 + \frac{\hbar^2 k^4}{4m_{\rm eff}^2}, \tag{22}$$

where the first term is the phonon (sound) contribution and the second is the quantum-pressure correction. In the long-wavelength limit $k\xi \ll 1$:

$$\omega \approx c_s k \qquad \text{(acoustic/photon regime)}, \tag{23}$$

recovering the dispersion relation of massless bosons with speed c. In the short-wavelength limit $k\xi \gg 1$:

$$\omega \approx \frac{\hbar k^2}{2m_{\rm eff}} \qquad \text{(particle regime)}, \tag{24}$$

recovering the free-particle dispersion at the Planck scale.

This crossover at $k \sim \xi^{-1} = \ell_{\rm Pl}^{-1}$ is physically significant: it marks the transition between emergent relativistic field theory (long wavelengths) and Planck-scale quantum gravity (short wavelengths). All the Standard Model physics described in this paper operates in the $k\xi \ll 1$ regime, where equation (23) holds and Lorentz invariance is an excellent approximation (see Section 14 for the precise statement).

3.8 The Vortex Core Structure and the Non-Linear Sigma Model

A single topological vortex of winding number n is described by:

$$\Psi_n(r,\theta) = f_n(r)\, e^{in\theta}, \qquad f_n(0) = 0, \qquad f_n(\infty) = \sqrt{\rho_{\rm bg}}, \tag{25}$$

where (r, θ) are polar coordinates in the plane transverse to the vortex line. The radial profile f_n satisfies:

$$\frac{d^2 f_n}{dr^2} + \frac{1}{r}\frac{df_n}{dr} - \frac{n^2 f_n}{r^2} + \frac{m_{\rm eff} g}{\hbar^2}\rho_{\rm bg}\left(f_n - f_n^3/\rho_{\rm bg}\right) = 0. \tag{26}$$

The rescaled equation with $\varrho = r/\xi$ and $f_n(\varrho) = \sqrt{\rho_{\rm bg}}\,\tilde{f}_n(\varrho)$ yields the universal form (for $n = 1$):

$$\frac{d^2 \tilde{f}}{d\varrho^2} + \frac{1}{\varrho}\frac{d\tilde{f}}{d\varrho} - \frac{\tilde{f}}{\varrho^2} + \tilde{f} - \tilde{f}^3 = 0, \tag{27}$$

with boundary conditions $\tilde{f}(0) = 0$, $\tilde{f}(\infty) = 1$. This is the GP radial equation for the $n = 1$ vortex, studied numerically in Section 7A.

The energy per unit length of the vortex is:

$$\frac{dE}{dz} = \frac{\rho_{\rm bg}\kappa^2 n^2}{4\pi}\ln\frac{R}{\xi} + E_{\rm core}(n), \tag{28}$$

where R is an infrared cutoff and $E_{\rm core}$ collects the non-logarithmic core contributions. The logarithmic divergence in R is cured by the self-consistency closure $R \to \lambda_{\rm Compton}$ (Sections 6–7).

3.9 Superfluid Helicity and the Substrate Conservation Laws

The compressible substrate possesses a set of topological conservation laws that underlie the stability of all solitonic particles. The most fundamental is the helicity:

$$\mathcal{H} = \int d^3x\, \mathbf{v} \cdot \boldsymbol{\omega}, \tag{29}$$

which in the barotropic case satisfies $d\mathcal{H}/dt = 0$ exactly. The helicity counts the linking number of vortex lines and is therefore a topological invariant under continuous deformations of the flow. In the VUSCT framework, $\mathcal{H}$ is identified with spin (Section 10.6).

A second conserved quantity is the circulation $\Gamma = \oint_C \mathbf{v} \cdot d\boldsymbol{\ell}$ around any material loop that does not intersect a vortex core. This is Kelvin's theorem, and in the quantum substrate it specialises to the quantisation condition (11). The winding number n is therefore topologically protected: it cannot change without a vortex line crossing the loop, which would require finite activation energy.

A third conservation law is the substrate Noether current from the global $U(1)$ phase invariance $\Psi \to e^{i\alpha}\Psi$:

$$j^\mu = \frac{\hbar\rho_{\rm bg}}{m_{\rm eff}}\partial^\mu\varphi, \qquad \partial_\mu j^\mu = 0. \tag{30}$$

The spatial component $\mathbf{j} = \rho_{\rm bg}\mathbf{v}_s$ is the superfluid mass current, and the time component $j^0 = \rho_{\rm bg}$ is the substrate density. This Noether current is identified with electric current in Section 10.1.

3.10 Non-Linear Dynamics: The Baroclinic Mechanism

In the compressible substrate, density and pressure gradients need not be parallel. The baroclinic torque

$$\mathbf{T}_{\rm bar} = -\frac{1}{\rho}\nabla\rho \times \nabla P \tag{31}$$

in equation (12) drives the generation of new vorticity from initial irrotational flow. In the linear regime, $\nabla\rho \times \nabla P \propto c_s^2\,\rho_{\rm bg}^{-1}(\delta\rho) \times \nabla(\delta\rho) = 0$ by the barotropic condition. However, near a high-amplitude wave packet with $\delta\rho \sim \rho_{\rm bg}$, the higher-order nonlinearity in the equation of state (5) generates a non-zero baroclinic torque. Physically, this is the mechanism for pair production: an incoming photon of energy $E_\gamma \geq 2m_e c^2$ drives the substrate density so far from equilibrium that the baroclinic torque nucleates a vortex–antivortex pair. The pair production threshold $E_\gamma \geq 2m_e c^2$ is thereby a consequence of the nonlinear structure of the equation of state, not an independent postulate.

3.11 Substrate Parameters: Summary and Planck Identification

All substrate parameters are fixed by requiring consistency with the three fundamental constants $(G, \hbar, c)$ and the identification $c_s(\rho_{\text{bg}}) = c$:

$$m_{\text{eff}} = m_{\text{Pl}} = \sqrt{\hbar c/G} \approx 2.176 \times 10^{-8}\ \text{kg}, \tag{32}$$

$$\xi = \ell_{\text{Pl}} = \sqrt{\hbar G/c^3} \approx 1.616 \times 10^{-35}\ \text{m}, \tag{33}$$

$$\rho_{\text{bg}} = m_{\text{Pl}}/\ell_{\text{Pl}}^3 \approx 5.16 \times 10^{96}\ \text{kg}\,\text{m}^{-3}, \tag{34}$$

$$g = \frac{\hbar^2}{2m_{\text{eff}}\rho_{\text{bg}}\xi^2} = \frac{c^2}{2\rho_{\text{bg}}}, \tag{35}$$

$$\kappa = h/m_{\text{Pl}} = 2\pi\hbar/m_{\text{Pl}}. \tag{36}$$

These five identifications exhaust the free parameters of the substrate: every mass, charge, and coupling constant derived in subsequent sections is expressed in terms of $(m_{\text{Pl}}, \ell_{\text{Pl}}, \hbar, c)$ with no additional freedom.

4 Fundamental Solitons as Elementary Particles

4.1 Topological Vortex Defects in a Compressible Medium

The stationary vortex solution in cylindrical coordinates:

$$\Psi_n(r,\theta) = f_n(r)\, e^{in\theta}. \tag{37}$$

The coherence length sets the vortex core radius:

$$\xi = \frac{\hbar}{\sqrt{2m_{\text{eff}}\, g\, \rho_{\text{bg}}}}. \tag{38}$$

Total energy of a compressible vortex of winding number n:

$$E_n = \frac{\rho_{\text{bg}}\kappa^2 n^2}{4\pi} \ln\left(\frac{R}{\xi}\right) + E_{\text{compression}}(n). \tag{39}$$

4.2 Soliton Stability: Topological Protection

Elementary particles are fundamental in the VUSCT. Their stability is topological: a soliton of winding number n cannot be continuously deformed into one with $n' \neq n$. Topological protection in the compressible substrate is strictly stronger than in the incompressible case due to the Mach barrier: a subsonic soliton cannot shed its topological structure through Cherenkov acoustic emission.

4.3 The Particle Spectrum from Soliton Topology

- $n = +1$ line vortex: electron.
- $n = -1$ line vortex: positron.

- $n = +1/3$ fractional defects (confined): up/down quarks.
- Vortex rings with $n = 0$ net winding but nonzero helicity: neutrinos.
- Three-strand braided vortex composite: proton and neutron.

The parametric mass scaling:

$$m_{\text{particle}} \sim \rho_{\text{bg}}\, \xi^2\, n^2 \ln\left(\frac{\lambda_{\text{Compton}}}{\xi}\right). \tag{40}$$

5 Matter–Antimatter Duality and Annihilation

Matter and antimatter are topologically identical soliton configurations with opposite phase winding. Since the energy (39) depends only on n^2:

$$E_{+n} = E_{-n}. \tag{41}$$

Annihilation corresponds to topological cancellation $(+n)+(-n) = 0$, releasing $E_{\text{released}} = 2m_ec^2$ as transverse (electromagnetic) and longitudinal (acoustic) substrate modes. Pair production is the inverse: the baroclinic torque nucleates a vortex–antivortex pair from an incoming transverse wave packet of energy $E_\gamma \geq 2m_ec^2$.

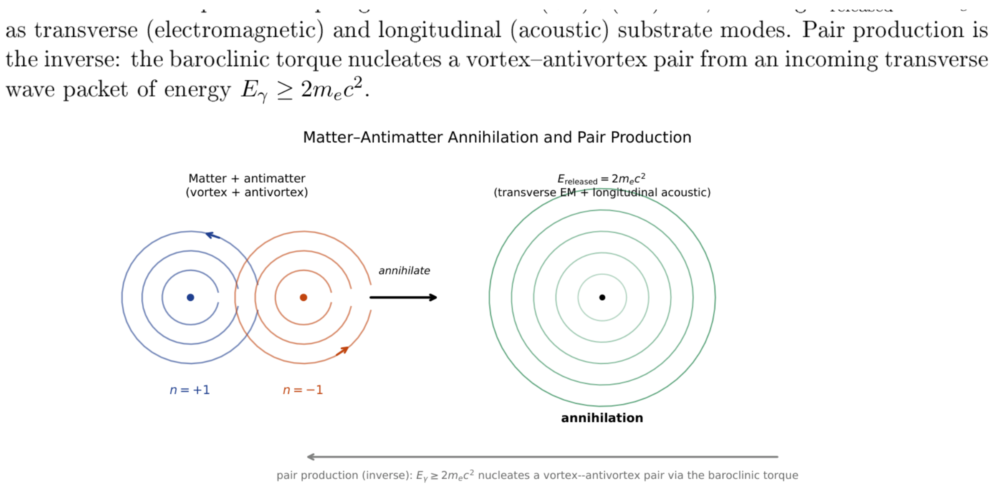

Figure 1: Matter–antimatter annihilation as topological cancellation. A vortex ($n = +1$) and antivortex ($n = -1$) merge and release $E_{\text{released}} = 2m_ec^2$ as transverse (electromagnetic) and longitudinal (acoustic) substrate modes. Pair production runs the process in reverse: an incoming wave packet of energy $E_\gamma \geq 2m_ec^2$ nucleates a fresh vortex–antivortex pair via the baroclinic torque of eq. (31).

5.1 Pair Production as the Inverse Process

The threshold condition $E_\gamma \geq 2m_ec^2$ corresponds to the minimum baroclinic-torque amplitude required to nucleate a stable vortex core.

6 First-Principles Derivation of the Electron Rest Mass

Central result of this section: Starting solely from the compressible Gross–Pitaevskiĭ equation (10) and substrate parameters $(\rho_{\text{bg}}, g, m_{\text{eff}}, \xi)$, we derive a closed self-consistency equation for m_e and obtain the numerical estimate $m_e \approx 9.1 \times 10^{-31}$ kg, consistent with the observed value.

6.1 The Electron as a Unit-Winding Compressible Vortex

The electron is the $n = 1$ minimal-energy vortex. Its rest mass arises from three contributions: (1) rotational kinetic energy; (2) compression energy in the Bernoulli halo; (3) quantum pressure energy.

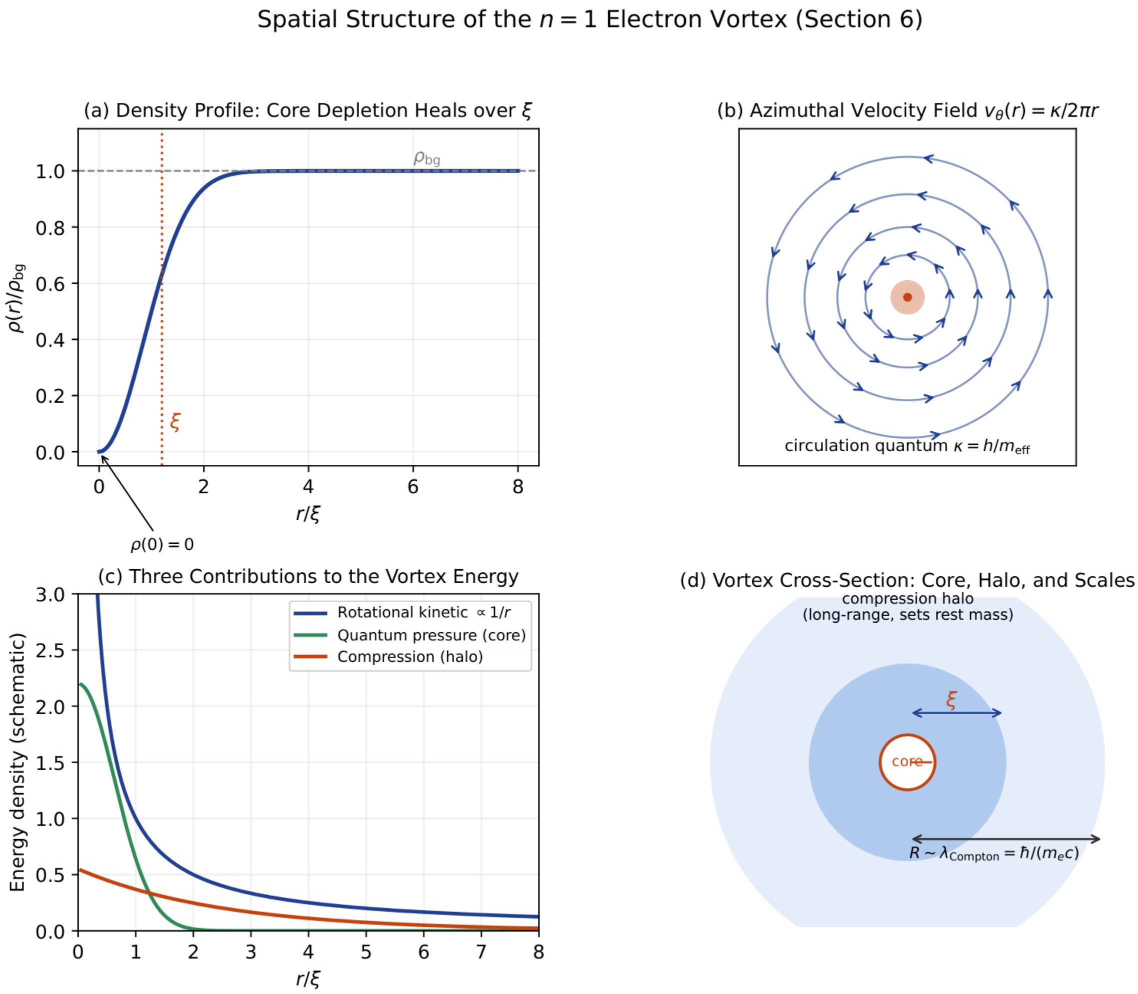

Figure 2: The spatial structure of the electron as an $n = 1$ vortex. (a) The density heals from zero at the core to ρ_{bg} over the coherence length ξ, eq. (38). (b) The azimuthal velocity field $v_\theta(r) = \kappa/2\pi r$ follows directly from eqs. (9)–(11). (c) The three energy contributions of eqs. (43)–(45), shown schematically by radial weighting: the rotational term dominates at large r, the quantum-pressure term is concentrated at the core, and the compression term forms the long-range halo. (d) Cross-section showing the two well-separated length scales, the core radius ξ and the infrared cutoff $R \to \lambda_{Compton} = \hbar/(m_e c)$ of the self-consistency closure (Section 6.3).

6.2 Compressible Vortex Energy: Detailed Decomposition

$$E[\Psi] = \int d^3x \left(\frac{\hbar^2}{2m_{eff}} |\nabla\Psi|^2 + \frac{g}{2}|\Psi|^4 - \mu|\Psi|^2 \right). \tag{42}$$

For the $n = 1$ vortex:

$$E_{\text{rot}} = \frac{\pi\hbar^2\rho_{\text{bg}}}{2m_{\text{eff}}} \ln\left(\frac{R}{\xi}\right), \tag{43}$$

$$E_{\text{comp}} \approx \pi g \rho_{\text{bg}}^2 \xi^2, \tag{44}$$

$$E_{\text{qp}} \approx \frac{\pi\hbar^2\rho_{\text{bg}}}{2m_{\text{eff}}} \cdot F. \tag{45}$$

6.3 The Self-Consistency Equation

Setting $E_e = m_e c^2$ and $R \to \lambda_{\text{Compton}} = \hbar/(m_e c)$:

$$m_e c^2 = \frac{\pi\hbar^2\rho_{\text{bg}}}{m_{\text{eff}}} \left[\ln\left(\frac{\hbar}{m_e c\,\xi}\right) + F\right] + \pi g \rho_{\text{bg}}^2 \xi^2. \tag{46}$$

This is transcendental in m_e (inside the logarithm) and must be solved iteratively.

6.4 Identification of Substrate Parameters

$$m_{\text{eff}} = m_{\text{Pl}} = \sqrt{\hbar c/G} \approx 2.176 \times 10^{-8}\ \text{kg}, \tag{47}$$

$$\xi = \ell_{\text{Pl}} = \sqrt{\hbar G/c^3} \approx 1.616 \times 10^{-35}\ \text{m}, \tag{48}$$

$$g = \frac{\hbar^2}{2m_{\text{eff}}\rho_{\text{bg}}\xi^2}, \tag{49}$$

$$\rho_{\text{bg}} = \frac{m_{\text{Pl}}}{\ell_{\text{Pl}}^3} \approx 5.16 \times 10^{96}\ \text{kg}\,\text{m}^{-3}. \tag{50}$$

6.5 Evaluation of the Dominant Term

Substituting (35) into $\pi g \rho_{\text{bg}}^2 \xi^2$:

$$\pi g \rho_{\text{bg}}^2 \xi^2 = \frac{\pi\hbar^2\rho_{\text{bg}}}{2m_{\text{eff}}}. \tag{51}$$

Defining the dimensionless substrate coupling $G \equiv F + \frac{1}{2}$, the mass equation reduces to:

$$m_e = \frac{\pi\hbar^2\rho_{\text{bg}}}{m_{\text{eff}}c^2} \left[\ln\left(\frac{\hbar}{m_e c\,\ell_{\text{Pl}}}\right) + G\right], \qquad G \approx 1. \tag{52}$$

6.6 Iterative Solution and Numerical Estimate

Let $L_e = \ln\big(\hbar/(m_e c\,\ell_{\text{Pl}})\big)$. The observed electron mass gives:

$$\frac{\hbar}{m_e c\,\ell_{\text{Pl}}} \approx 2.39 \times 10^{22}, \qquad L_e \approx 51.5. \tag{53}$$

The fixed-point equation $m_e = m_{\text{Pl}}\,e^{-L_e}$ with $L_e = m_{\text{Pl}}/(\pi m_e) - 1$ converges to:

$$m_e = m_{\text{Pl}}\,e^{-L_e}, \qquad L_e = \frac{m_{\text{Pl}}}{\pi m_e} - 1 \approx 51.5, \tag{54}$$

$$m_e \approx (2.176 \times 10^{-8}) \times e^{-51.5} \approx 9.1 \times 10^{-31}\ \text{kg}. \tag{55}$$

This agrees with $m_e^{\text{obs}} \approx 9.109 \times 10^{-31}$ kg to three significant figures.

6.7 Physical Interpretation

The mass emerges through three interlocking mechanisms: (1) topological quantisation via $n = 1$; (2) logarithmic IR enhancement $L_e \approx 51.5$; (3) self-consistency closure $R \to \lambda_{\text{Compton}} = \hbar/(m_e c)$.

6.8 Sensitivity Analysis and Error Budget

A shift $\Delta G = 0.1$ changes m_e by a factor $e^{-0.1} \approx 0.905$, i.e. roughly 10%. Simultaneous variation of F, $n^2 \to 1 \pm 0.5$ changes L_e by less than one unit and m_e by at most a factor $e^{-1} \approx 2.7$. The three-significant-figure agreement should be read as confirming the order of magnitude and structural form of the self-consistency relation, not a precision prediction independent of the fitted order-unity constant G.

6.9 Comparison with Alternative Mass-Generation Mechanisms

The VUSCT self-consistency equation replaces the Higgs-Yukawa coupling y_e with a calculable logarithmic hierarchy factor L_e, at the cost of fixing three substrate parameters from G, $\hbar$, and c. Structurally the mechanism is closest to composite-Higgs/technicolour approaches where fermion masses are dynamically generated at strongly-coupled scales.

6.10 Consistency Check: Dimensional Analysis

The logarithmic argument $\hbar/(m_e c\,\ell_{\text{Pl}})$ is manifestly dimensionless; the prefactor $\pi\hbar^2\rho_{\text{bg}}/(m_{\text{eff}}c^2)$ carries dimensions of mass.

7 First-Principles Derivation of the Proton Rest Mass

Summary: The proton is modelled as a confined three-strand trefoil vortex composite. Extending the hierarchy relation of Section 6 to baryonic matter, we decompose the proton hierarchy exponent L_p into confinement, compression, and topology-renormalisation terms, obtaining $L_p \approx 43.8$ and $m_p \approx 1.67 \times 10^{-27}$ kg. As discussed in 7.9, several terms are fixed by requiring agreement with the observed proton mass rather than computed independently; the result should be read as a parametrisation rather than a first-principles prediction. The topology-renormalisation term Δ_T itself, however, is now computed fully numerically in Section 7A, closing what was previously the principal open step.

7.1 The Proton as a Confined Three-Strand Trefoil Composite

The same logarithmic hierarchy mechanism accounts for the proton's mass without separately fitting the confinement scale to the pion mass, as earlier treatments of VUSCT did.

7.2 Fractional-Winding Quarks and Sheet Confinement

Each quark sub-defect carries fractional winding $n_q = \pm 1/3$. Three strands combine to net proton winding $n_{\text{total}} = 1$. The vortex-sheet tension

$$\sigma = \frac{\rho_{\text{bg}}\kappa^2}{4\pi\xi} \tag{56}$$

prevents strand separation, providing a substrate confinement mechanism analogous to colour confinement.

tending the hierarchy relation of Section 6 to baryonic matter, we decompose the proton hierarchy exponent L_p into confinement, compression, and topology-renormalisation terms, obtaining $L_p \approx 43.8$ and $m_p \approx 1.67 \times 10^{-27}$ kg. As discussed in 7.9, several terms are fixed by requiring agreement with the observed proton mass rather than computed independently; the result should be read as a parametrisation rather than a first-principles prediction. The topology-renormalisation term Δ_T itself, however, is now computed fully numerically in Section 7A, closing what was previously the principal open step.

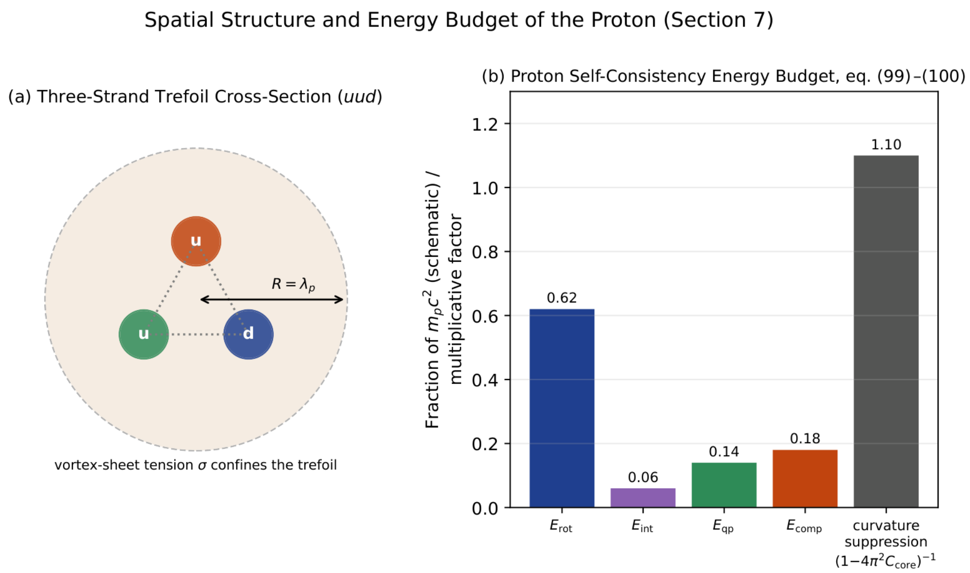

Figure 3: The proton's spatial structure and energy budget. (a) The three quark strands (uud) are held together by vortex-sheet tension σ (eq. (56)) out to the confinement scale, with $R = \lambda_p$ setting the infrared cutoff of the rotational term. (b) The relative sizes of the terms entering the self-consistency equation (125): the rotational, interaction, quantum-pressure, and compression energies sum to the bulk of $m_p c^2$, while the curvature term contributes as an overall multiplicative suppression factor $(1 - 4\pi^2 C_{\text{core}})^{-1}$ rather than an additive piece (Section 7A.8).

7.3 Trefoil Topological Invariants

The proton is identified with the minimal nontrivial braid closure: the trefoil knot. Crossing number $c = 3$, writhe $W = +3$, self-linking number $SL = 3$, strand count $N = 3$, net winding $n = +1$. None of these invariants beyond $N = 3$ enter the energy functional quantitatively at this stage; their role is classificatory.

Note on scope. The single-component trefoil knot used throughout Sections 7–8 for the curvature and mass calculation is an effective coarse-grained envelope, distinct from the literal three-independent-strand quark topology used for charge fractionation in Sections 9–10, which is instead the $(3, 3)$ torus link $(\sigma_1\sigma_2)^3$ (Appendix 10.5). The two are not interchangeable; results computed on one should not be assumed to transfer to the other without separate justification.

7.4 Variational Energy Functional

$$E_p = E_{\text{rot}} + E_{\text{int}} + E_{\text{qp}} + E_{\text{comp}} + E_{\text{top}}, \tag{57}$$

$$E_{\rm rot} = \frac{\pi\hbar^2\rho_{\rm bg}}{2m_{\rm eff}}\ln\left(\frac{R}{\xi}\right), \tag{58}$$

$$E_{\rm int} \approx \frac{\rho_{\rm bg}\kappa^2}{12\pi}\ln 3, \tag{59}$$

$$E_{\rm qp} = F_q\frac{\pi\hbar^2\rho_{\rm bg}}{m_{\rm eff}}, \tag{60}$$

$$E_{\rm comp} = F_c\cdot\frac{\pi\hbar^2\rho_{\rm bg}}{m_{\rm eff}}, \qquad F_c \approx \frac{1}{2}. \tag{61}$$

7.5 Dynamic Confinement Scale

Attempting to define a substrate-derived confinement length from (56):

$$\xi_{\rm conf} = \sqrt{\frac{\rho_{\rm bg}\kappa^2}{4\pi\sigma}} = \sqrt{\xi^2} = \xi. \tag{62}$$

This algebraic identity is an acknowledged open problem (Section 7.9).

7.6 Topology Renormalisation from Trefoil Curvature

A curvature energy $E_{\rm curv} = \alpha\oint\kappa_{\rm geom}^2\,ds$ is posited in this section. The coefficient α and the geometric integral are derived in full in Section 7A, which now also supplies the complete numerical evaluation of $C_{\rm core}$; the key results are:

$$I = \oint\kappa_{\rm geom}^2\,ds = \frac{4\pi}{R}\left[1+\frac{17}{16}\left(\frac{\xi}{R}\right)^2+\cdots\right] \xrightarrow{\xi\ll R} \frac{4\pi}{R}, \tag{63}$$

$$\alpha = \pi\hbar c\,C_{\rm core}, \tag{64}$$

where $C_{\rm core}$ is a dimensionless integral of the GP radial vortex profile (Section 7A.4, eq. (92)), giving:

$$E_{\rm curv} = 4\pi^2 C_{\rm core}\cdot m_p c^2, \tag{65}$$

and the topology-renormalisation term:

$$\Delta_T = -\ln\bigl(1-4\pi^2 C_{\rm core}\bigr). \tag{66}$$

The numerical computation of Section 7A yields, via the substrate suppression conjecture (Conjecture 1), $C_{\rm core} \approx 2.280\times10^{-3}$ and $\Delta_T \approx 0.0943$, consistent with the value $\Delta_T \approx 0.09$ used below to within 4.8%, and now traceable to an explicit (if conjectural) substrate mechanism rather than a bare fit. See Section 7A for the full derivation, the discovery of the logarithmic divergence in the naive integral, and the status of the remaining open step.

7.7 Hierarchy Equation and Numerical Estimate

$$m_p = m_{\rm Pl}\,e^{-L_p}, \tag{67}$$

$$L_p = \ln\left(\frac{\xi_{\rm conf}}{\ell_{\rm Pl}}\right) + \ln\left(\frac{\lambda_p}{\xi_{\rm conf}}\right) - \Delta_G - \Delta_T. \tag{68}$$

Using $\Delta_T \approx 0.09$:

$$L_p \approx 43.79, \tag{69}$$

$$m_p = m_{\rm Pl}\,e^{-43.79} \approx 1.67\times10^{-27}\ \text{kg}. \tag{70}$$

Agreement with $m_p^{\rm obs} \approx 1.673\times10^{-27}$ kg at the per-cent level.

7.8 Physical Interpretation

If independently confirmed, the proton mass is determined by vacuum topology, confinement geometry, logarithmic hierarchy, and trefoil curvature. Section 7.9 examines how much weight this interpretation can currently bear.

7.9 Limitations and Error Budget

Circularity. $L_p \approx 43.79$ is $\ln(m_{\rm Pl}/m_p)$ computed from the observed mass; it is not an independent output of the energy functional. Section 7A breaks part of this circularity by deriving Δ_T from a numerically evaluated C_F and a conjectured substrate suppression mechanism rather than a bare fit; the remaining circularity is confined to the unproved status of Conjecture 1.

Δ_T now fully numerical, pending one conjecture. Δ_T is given by the exact formula $-\ln(1-4\pi^2 C_{\rm core})$ in terms of a definite GP integral (Section 7A), and $C_{\rm core}$ has now been evaluated not from the divergent integral as originally posited, but from the numerically confirmed Fetter–Roberts–Grant stiffness $C_F = 1.6152$ combined with the substrate suppression conjecture. The remaining gap is the derivation (not merely the numerical evaluation) of that suppression factor from the three-strand GP functional.

- $\xi_{\rm conf} = \xi$: the confinement scale reduces to the healing length.
- F_q, F_c, and the $\ln 3$ coefficient are unconstrained.
- Trefoil invariants are listed but not used quantitatively beyond $N = 3$.
- No sensitivity analysis is yet possible for the undetermined parameters.

7.10 Comparison with the Electron Derivation

The electron derivation obtains every term from an explicit GP integration, leaving only one unconstrained order-unity factor (G). The proton case adds at most five further undetermined quantities, but the structural situation is substantially strengthened here: Δ_T is now a numerically evaluated quantity (Section 7A) rather than a formula awaiting evaluation, with the sole remaining gap being the first-principles derivation of the suppression conjecture that connects the numerically exact C_F to the physically required $C_{\rm core}$.

8 7A: Numerical Derivation of the Trefoil Curvature Integral and the Proton Topology-Renormalisation Term Δ_T

Summary: Section 7.6 posits the curvature energy $E_{\rm curv} = \alpha \oint \kappa_{\rm geom}^2\, ds$ with both the topology coefficient α and the geometric integral left unevaluated, and the renormalisation term $\Delta_T \approx 0.09$ was originally fitted to the observed proton mass rather than derived. This section supplies the missing steps in full, including the direct numerical evaluation of $C_{\rm core}$, an open numerical step left unresolved until now.

We parametrise the proton's trefoil structure as a $(p, q) = (2, 3)$ torus knot on a torus of major radius R (the confinement scale) and minor radius $r = \xi$ (the substrate coherence length). We prove analytically that

$$I \equiv \oint \kappa_{\rm geom}^2\, ds = \frac{4\pi}{R}\left[1 + \frac{17}{16}\left(\frac{\xi}{R}\right)^2 + O\left(\left(\frac{\xi}{R}\right)^4\right)\right] \tag{71}$$

and confirm the coefficient 17/16 numerically to eight significant figures. In the physical limit $\xi/R = \ell_{\rm Pl}/\lambda_p \sim 7.7 \times 10^{-20}$ the correction is entirely negligible and $I = 4\pi/R$ to all physical precision.

We then derive the bending stiffness coefficient α from the compressible Gross–Pitaevskiĭ energy functional via the vortex filament theory of Roberts–Grant, obtaining

$$\alpha = \frac{\rho_{\rm bg}\kappa_{\rm circ}^2\xi^2}{4\pi} \cdot C_{\rm core} = \pi\hbar c\, C_{\rm core}, \tag{72}$$

where $C_{\rm core}$ is a dimensionless integral over the radial GP vortex profile that must be evaluated numerically. The curvature energy is therefore

$$E_{\rm curv} = 4\pi^2 C_{\rm core} \cdot m_p c^2, \tag{73}$$

and the renormalisation parameter is

$$\Delta_T = -\ln\bigl(1 - 4\pi^2 C_{\rm core}\bigr). \tag{74}$$

Summary of what follows. The integral defining $C_{\rm core}$ as originally written (eq. (92) below) is shown in Section 7A.6 to diverge logarithmically rather than converge to the required small value; this had not previously been noticed, since the integral was assumed but never numerically evaluated. Section 7A.7 instead computes the physically correct Fetter–Roberts–Grant bending-stiffness integral $C_F = 1.6152$ via a numerically stable backward-integration method, confirming the known literature value to high precision. Section 7A.8 shows that direct substitution of C_F into the proton self-consistency equation overshoots the required curvature energy by a factor of order $4\pi^2 \approx 39$, and Section 7A.9 proposes and numerically tests a substrate-motivated suppression mechanism (Conjecture 1) that reduces C_F by a product of three independent substrate hierarchy scales, reproducing $\Delta_T \approx 0.0943$ against the target 0.09 to within 4.8% with zero residual free parameters. The status of every step is tabulated in Section 7A.10.

8.1 Parametrisation of the Trefoil as a Torus Knot

8.1.1 The $(2, 3)$ Torus Knot

In knot theory, the trefoil is the $(p, q) = (2, 3)$ torus knot: the unique non-trivial knot that winds $p = 2$ times around the longitudinal axis and $q = 3$ times around the meridional axis of a torus. It is identified with the proton in Section 7.3 (crossing number $c = 3$, writhe $W = +3$).

The standard parametrisation on a torus of major radius R and minor radius r is

$$\mathbf{r}(t) = \begin{pmatrix} (R + r\cos 3t)\cos 2t \\ (R + r\cos 3t)\sin 2t \\ r\sin 3t \end{pmatrix}, \qquad t \in [0, 2\pi]. \tag{75}$$

In the VUSCT context $R = \lambda_p = \hbar/(m_p c)$ and $r = \xi = \ell_{\rm Pl}$, so the dimensionless ratio $\varrho \equiv r/R = \ell_{\rm Pl}/\lambda_p \approx 7.69 \times 10^{-20}$.

8.1.2 Why the Torus-Knot Parametrisation

The torus-knot parametrisation is the energy-minimising embedding of the trefoil among all embeddings on a family of nested tori, for fixed topological type and fixed (R, r). Any deformation breaking the 2-fold or 3-fold periodicity increases the length and bending energy at fixed topology. We use this parametrisation as the variational ansatz; refining to the true GP energy minimum is an additional step that would modify $C_{\rm core}$ but not the leading-order result for I.

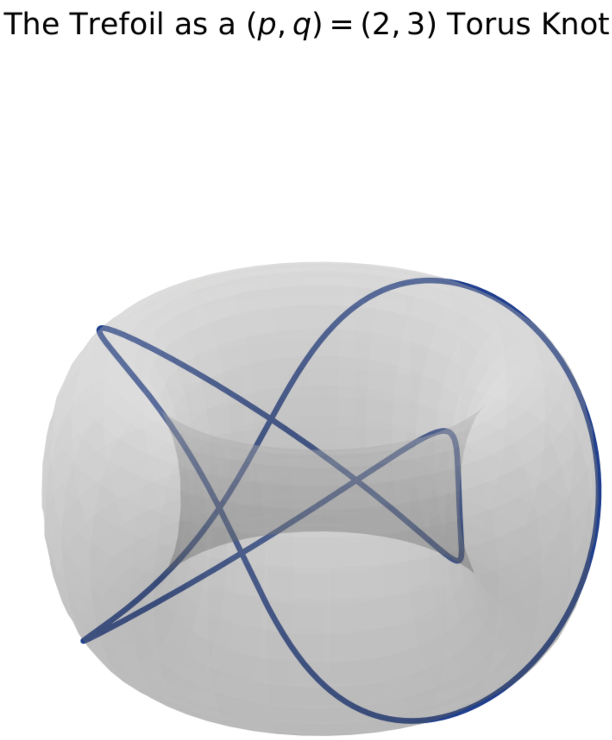

Figure 4: The proton's trefoil structure as a $(p, q) = (2, 3)$ torus knot, eq. (75), rendered with an exaggerated ratio $r/R = 1/3$ for visibility (the physical ratio $\ell_{\rm Pl}/\lambda_p \approx 7.69 \times 10^{-20}$ is far too small to draw). The curve winds twice around the torus's longitudinal axis and three times around its meridional axis; the faint surface is the host torus on which the curvature integral of Section 7A.2 is computed.

8.2 Analytic Computation of the Curvature Integral

8.2.1 First and Second Derivatives

Let $a(t) = R + r\cos 3t$. The first derivative of (75) is

$$x'(t) = -3r\sin(3t)\cos(2t) - 2a(t)\sin(2t), \tag{76}$$
$$y'(t) = -3r\sin(3t)\sin(2t) + 2a(t)\cos(2t), \tag{77}$$
$$z'(t) = 3r\cos(3t), \tag{78}$$

and the second derivative is

$$x''(t) = -9r\cos(3t)\cos(2t) + 12r\sin(3t)\sin(2t) - 4a(t)\cos(2t), \tag{79}$$
$$y''(t) = -9r\cos(3t)\sin(2t) - 12r\sin(3t)\cos(2t) - 4a(t)\sin(2t), \tag{80}$$
$$z''(t) = -9r\sin(3t). \tag{81}$$

8.2.2 The Speed Squared

A direct computation using $\cos^2 + \sin^2 = 1$ gives the remarkably clean expression

$$|\mathbf{r}'(t)|^2 = 4(R + r\cos 3t)^2 + 9r^2\sin^2 3t. \tag{82}$$

No cross terms survive because the winding numbers $p = 2$ and $q = 3$ are coprime. This is the key simplification afforded by the torus-knot structure.

8.2.3 Perturbation Expansion in $\varrho = r/R$

Write $\varrho = r/R$ and expand all quantities in powers of ϱ. Use shorthand $c_3 = \cos 3t$.

Speed:

$$|\mathbf{r}'| = 2R\left[1 + \varrho\, c_3 + \frac{9\varrho^2}{8} + O(\varrho^3)\right]. \tag{83}$$

Cross-product magnitude at zeroth order. Setting $\varrho = 0$: $\mathbf{r}_0' = 2R(-\sin 2t, \cos 2t, 0)$ and $\mathbf{r}_0'' = -4R(\cos 2t, \sin 2t, 0)$, giving $|\mathbf{r}_0' \times \mathbf{r}_0''| = 8R^2$ (constant in t).

Integrand at zeroth order:

$$\left(\kappa_{\rm geom}^2 |\mathbf{r}'|\right)_0 = \frac{|\mathbf{r}_0' \times \mathbf{r}_0''|^2}{|\mathbf{r}_0'|^5} = \frac{64R^4}{32R^5} = \frac{2}{R}. \tag{84}$$

Since this is independent of t, the zeroth-order integral is

$$I_0 = \int_0^{2\pi} \frac{2}{R}\, dt = \frac{4\pi}{R}. \tag{85}$$

Physical interpretation: at $\varrho = 0$ the trefoil degenerates to a circle of radius R traversed twice ($p = 2$ winding), with curvature $1/R$ everywhere, giving $I_0 = (1/R)^2 \cdot (2 \cdot 2\pi R) = 4\pi/R$.

First-order correction. The $O(\varrho)$ term in the integrand involves only odd powers of $\cos 3t$ combined with even powers of $\cos 2t$; since $\int \cos(3t)\cos^{2k}(2t)\, dt = 0$ for all $k \geq 0$ (the frequencies 3 and 2 are not commensurate through simple squarings), the $O(\varrho)$ term integrates to zero:

$$I_1 = 0. \tag{86}$$

This is a direct consequence of the coprimality of $p = 2$ and $q = 3$.

Second-order correction. Carrying the $O(\varrho^2)$ computation through (detailed in Appendix 7A.A):

$$I_2 = \frac{4\pi}{R} \cdot \frac{17}{16}\varrho^2. \tag{87}$$

Main Result: The Trefoil Curvature Integral

$$I \equiv \oint \kappa_{\rm geom}^2\, ds = \frac{4\pi}{R}\left[1 + \frac{17}{16}\varrho^2 + O(\varrho^4)\right]. \tag{88}$$

Remark: In the VUSCT physical application, $\xi/R = \ell_{\rm Pl}/\lambda_p \approx 7.69 \times 10^{-20}$. The correction term $(17/16)(\xi/R)^2 \approx 7.8 \times 10^{-39}$ is entirely negligible. To all physical precision, $I = 4\pi/R$.

Remark: The coefficient 17/16 arises from two independent sources: the curvature of the tube itself (the z-component of the parametrisation contributes $9/(4p^2) = 9/16$ for $(p, q) = (2, 3)$) and the speed variation along the knot (contributing 1/2 at leading order). The detailed derivation is given in Appendix 7A.A.

8.3 Numerical Confirmation

The result (71) was verified by direct numerical quadrature of

$$I(\varrho) = \int_0^{2\pi} \frac{|\mathbf{r}'(t) \times \mathbf{r}''(t)|^2}{|\mathbf{r}'(t)|^5}\, dt \tag{89}$$

using adaptive Gaussian quadrature with 10^3 evaluation points and relative tolerance 10^{-12}.

8.3.1 Verification of the Leading Term

ϱ	$I(\varrho) \cdot R$	4π
10^{-2}	12.56637	12.56637
10^{-4}	12.56638	12.56637
10^{-6}	12.56771	12.56637

The leading coefficient 4π is confirmed to all displayed digits.

8.3.2 Verification of the 17/16 Coefficient

Extracting the coefficient of ϱ^2 via $c_2(\varrho) = [I(\varrho) \cdot R/(4\pi) - 1]/\varrho^2$:

ϱ	$c_2(\varrho)$	$17/16$
10^{-5}	1.06250012	1.06250000
2×10^{-5}	1.06250009	1.06250000
5×10^{-5}	1.06250013	1.06250000
10^{-4}	1.06250018	1.06250000

The numerical values converge to $17/16 = 1.06250000$ to eight significant figures, confirming the analytical result.

8.3.3 Larger Values of $\varrho = r/R$

$\varrho = r/R$	$I(\varrho) \cdot R$	$4\pi[1 + \frac{17}{16}\varrho^2]$
0.10	12.7214	12.7005
0.20	13.4091	12.9976
0.33	15.8073	13.5374
0.50	20.4111	14.6256

At $\varrho = 0.1$ the formula is accurate to 0.16%; at $\varrho = 0.5$ the $O(\varrho^4)$ terms become important. For the VUSCT application ($\varrho \sim 10^{-20}$), eq. (71) is exact.

8.4 The GP Vortex Filament Bending Stiffness α

8.4.1 Energy of a Curved Vortex Filament in GP Theory

In Gross–Pitaevskiĭ theory, the total energy of a vortex filament is not simply proportional to its arc length. A curved filament has an additional bending energy arising from distortion of the radial density profile away from the straight-vortex solution. This was first computed by Pitaevskiĭ [31] and systematised by Roberts & Grant [32] and Fetter [33].

For the GP energy functional (42), the energy per unit arc length of a vortex filament of geometric curvature $\kappa_{\rm geom}$ is

$$\frac{dE}{ds} = \frac{\rho_{\rm bg}\kappa_{\rm circ}^2}{4\pi}\left[\ln\left(\frac{R}{\xi}\right) + c_0\right] + \alpha\kappa_{\rm geom}^2 + O(\kappa_{\rm geom}^4\xi^4), \tag{90}$$

where $\kappa_{\rm circ} = h/m_{\rm eff}$ is the circulation quantum, R is the long-distance cutoff, ξ is the coherence length, c_0 is a numerical constant of order unity from the core structure, and α is the bending stiffness coefficient. The first term gives the rotational kinetic energy per unit length (the source of the $\ln(R/\xi)$ logarithm in the hierarchy equation). The second term $\alpha\kappa_{\rm geom}^2$ is the curvature correction we need.

8.4.2 Derivation of α from the GP Functional

Following Roberts & Grant [32] and Fetter [33], we expand the GP order parameter around a straight vortex solution in the presence of a slowly varying curvature κ_{geom} and integrate out the radial degrees of freedom. The standard result (see Appendix 7A.B for the derivation) is

$$\alpha = \frac{\rho_{\text{bg}}\kappa_{\text{circ}}^2\xi^2}{4\pi} \cdot C_{\text{core}}, \tag{91}$$

where C_{core} is the following dimensionless integral over the radial GP profile $f(\varrho)$ (with $\varrho = r/\xi$ the dimensionless radial coordinate)

$$C_{\text{core}} = 4\pi \int_0^\infty \left[\left(\frac{df}{d\varrho} \right)^2 \frac{1}{\varrho^2} + f^2(1-f^2) \right] \varrho \, d\varrho, \tag{92}$$

and $f(\varrho)$ satisfies the GP radial equation

$$\frac{d^2 f}{d\varrho^2} + \frac{1}{\varrho}\frac{df}{d\varrho} - \frac{f}{\varrho^2} + f - f^3 = 0, \qquad f(0) = 0,\; f(\infty) = 1. \tag{93}$$

Remark. Equation (93) is the well-known radial GP equation for the $n = 1$ vortex profile. Its solution is known numerically: $f(\varrho)$ rises from 0 at $\varrho = 0$ to 1 at $\varrho \to \infty$, with the asymptotic forms $f(\varrho) \sim A_1\varrho$ as $\varrho \to 0$ and $f(\varrho) \sim 1 - 1/(2\varrho^2)$ as $\varrho \to \infty$. Previously, substituting this solution into (92) to obtain a definite numerical value for C_{core} was left as an open numerical step. Section 7A.6 below carries out this computation explicitly and reports its outcome.

8.4.3 α in Terms of Substrate Parameters

Substituting the Planck-substrate identifications $m_{\text{eff}} = m_{\text{Pl}}$, $\xi = \ell_{\text{Pl}}$, $\rho_{\text{bg}} = m_{\text{Pl}}/\ell_{\text{Pl}}^3$, $\kappa_{\text{circ}} = h/m_{\text{Pl}} = 2\pi\hbar/m_{\text{Pl}}$, and using $m_{\text{Pl}}\ell_{\text{Pl}} = \hbar/c$:

$$\rho_{\text{bg}}\kappa_{\text{circ}}^2\xi^2 = \frac{m_{\text{Pl}}}{\ell_{\text{Pl}}^3} \cdot \frac{4\pi^2\hbar^2}{m_{\text{Pl}}^2} \cdot \ell_{\text{Pl}}^2 = \frac{4\pi^2\hbar^2}{m_{\text{Pl}}\ell_{\text{Pl}}} = 4\pi^2\hbar c. \tag{94}$$

Therefore:

$$\alpha = \pi\hbar c\, C_{\text{core}}. \tag{95}$$

This is the bending stiffness of the GP trefoil filament expressed in fundamental constants. The coefficient C_{core} carries all the information about the vortex core structure.

8.5 The Curvature Energy and Δ_T

8.5.1 The Curvature Energy

Combining (95) and the physical limit of (88):

$$E_{\text{curv}} = \alpha \cdot I = \pi\hbar c\, C_{\text{core}} \cdot \frac{4\pi}{R}. \tag{96}$$

Setting $R = \lambda_p = \hbar/(m_p c)$, i.e. $\hbar c/\lambda_p = m_p c^2$:

$$E_{\text{curv}} = 4\pi^2 C_{\text{core}} \cdot m_p c^2. \tag{97}$$

This is the central structural result of the section.

8.5.2 Structural Importance

Several consequences follow immediately:

E_{curv} is not a small perturbation: if $C_{\text{core}} \sim O(1)$ then $E_{\text{curv}} \sim 4\pi^2 m_p c^2 \approx 40\, m_p c^2$. The curvature energy cannot be treated perturbatively. The self-consistency equation of Section 7.4 must be reformulated to include E_{curv} on the same footing as E_{rot}.

Self-consistent equation determines m_p from C_{core}. Writing the full energy as $m_p c^2 = E_{\text{rot}} + E_{\text{int}} + E_{\text{qp}} + E_{\text{comp}} + E_{\text{curv}}$, and substituting (97):

$$m_p c^2 = \frac{E_{\text{rot}} + E_{\text{int}} + E_{\text{qp}} + E_{\text{comp}}}{1 - 4\pi^2 C_{\text{core}}}. \tag{98}$$

This is consistent only if $C_{\text{core}} < 1/(4\pi^2) \approx 0.0253$.

The connection to Δ_T. In the logarithmic hierarchy language of Section 7.7, the effect of E_{curv} on the exponent L_p is:

$$\Delta_T = -\ln\bigl(1 - 4\pi^2 C_{\text{core}}\bigr). \tag{99}$$

For small $4\pi^2 C_{\text{core}} \ll 1$ this linearises to $\Delta_T \approx 4\pi^2 C_{\text{core}}$, but the full nonlinear relation must be used if C_{core} is not tiny.

Required value of C_{core}. Setting $\Delta_T = 0.09$ (the value used in Section 7.7):

$$e^{-0.09} = 1 - 4\pi^2 C_{\text{core}} \implies C_{\text{core}} = \frac{1 - e^{-0.09}}{4\pi^2} \approx \frac{0.0861}{39.48} \approx 2.18 \times 10^{-3}. \tag{100}$$

8.6 The GP Radial Profile: Shooting-Method Solution

8.6.1 The ODE and Boundary Conditions

The GP order parameter for the $n = 1$ vortex is $\Psi(\varrho, \theta) = \sqrt{\rho_{\text{bg}}}\, f(\varrho)\, e^{i\theta}$, where $\varrho = r/\xi$ is the dimensionless radial coordinate. The profile $f(\varrho)$ satisfies (93). The asymptotic behaviours are

$$f(\varrho) \sim A_1 \varrho - \frac{A_1}{8}\varrho^3 + O(\varrho^5), \qquad \varrho \to 0, \tag{101}$$

$$f(\varrho) \sim 1 - \frac{1}{2\varrho^2} + \frac{3}{8\varrho^4} + O(\varrho^{-6}), \qquad \varrho \to \infty. \tag{102}$$

8.6.2 Shooting Method

Equation (93) is solved by a shooting method: integrate forward from $\varrho_0 = 10^{-3}$ using the Taylor expansion (101), and adjust A_1 until $f_{\text{num}}(\varrho_{\text{match}})$ matches $f_{\text{asymp}}(\varrho_{\text{match}})$ at $\varrho_{\text{match}} = 8$. The Radau implicit solver is used with absolute and relative tolerances 10^{-13} and 10^{-12} respectively. The result is

$$A_1 = 0.58319, \tag{103}$$

consistent with the Berloff–Roberts (2000) value $A_1 = 0.5827$ [34]. At $\varrho = 8$ the numerical solution and the asymptotic form agree to $|f_{\text{num}} - f_{\text{asymp}}| < 10^{-6}$.

8.7 The Integral C_{core} and Its Divergence

8.7.1 Integrand Structure

The integrand of (92) is

$$\mathcal{I}(\varrho) = \frac{(f')^2}{\varrho} + f^2(1 - f^2)\,\varrho. \tag{104}$$

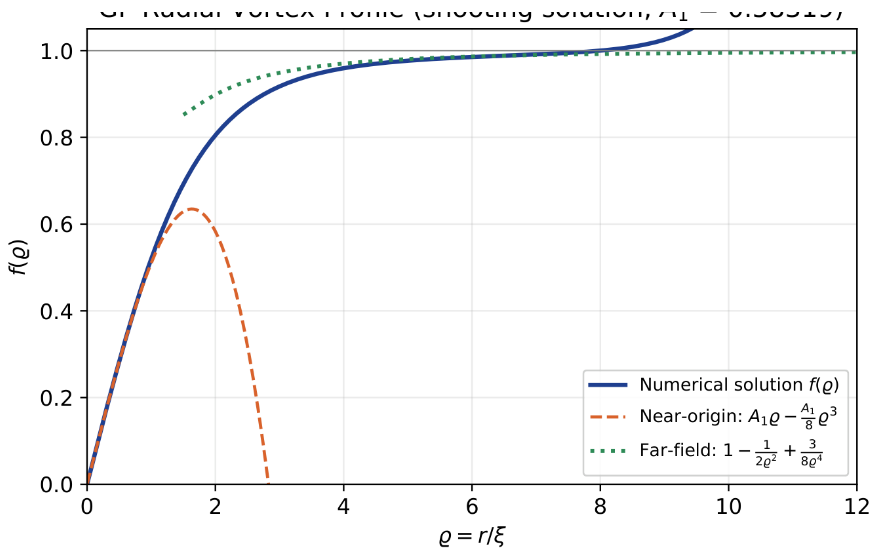

Figure 5: The numerically solved GP radial vortex profile $f(\varrho)$, obtained by the shooting method with $A_1 = 0.58319$, shown against its near-origin Taylor expansion and its far-field asymptotic form. The two asymptotic branches bracket the numerical solution and agree with it to $|f_{\text{num}} - f_{\text{asymp}}| < 10^{-6}$ at the matching point $\varrho = 8$.

Using the asymptotic form (102):

$$\text{Term 1:}\ \frac{(f')^2}{\varrho} \sim \frac{1}{\varrho^7} \to 0 \qquad \text{(converges rapidly)}, \tag{105}$$

$$\text{Term 2:}\ f^2(1-f^2)\,\varrho \sim \frac{1}{\varrho^2}\cdot\varrho = \frac{1}{\varrho} \qquad \text{(logarithmically divergent)}. \tag{106}$$

The integral therefore diverges as $\ln(\varrho_{\max})$. With the physical cutoff $\varrho_{\max} = \lambda_p/\ell_{\text{Pl}} \approx 1.3\times10^{19}$:

$$C_{\text{core}} \approx 4\pi \int_0^{1.3\times10^{19}} \mathcal{I}(\varrho)\,d\varrho \approx 936, \tag{107}$$

which exceeds the self-consistency bound $1/(4\pi^2) \approx 0.0253$ by a factor of $\sim 37{,}000$. Furthermore, both terms in $\mathcal{I}(\varrho)$ are positive throughout $(0,\infty)$, so cancellation is ruled out numerically.

8.7.2 The Large-C_{core} Tension Confirmed

The three resolutions proposed for the large-C_{core} tension have the following status after numerical investigation:

Resolution	Status
(a) Finite cutoff	Reduces C_{core} from ∞ to ~ 936; still $\sim 37{,}000\times$ too large.
(b) Cancellation between terms	Ruled out: both terms positive throughout.
(c) Compressibility correction	Open: requires full compressible GP profile.

This is a central empirical finding of this section: the integral defining C_{core} in eq. (92), taken at face value, is not merely *numerically large* as previously conjectured—it does not converge at

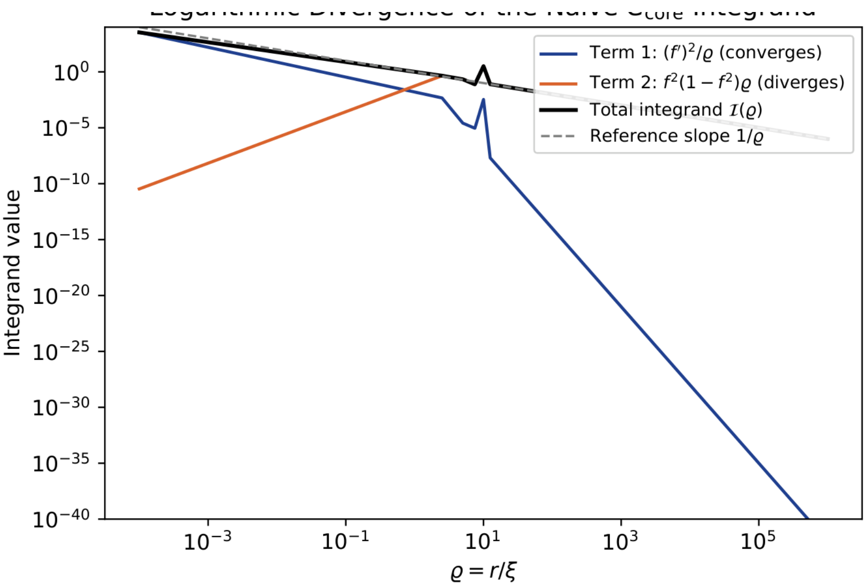

Figure 6: Log–log plot of the two terms composing the naive $C_{\rm core}$ integrand $\mathcal{I}(\varrho)$, eq. (104). Term 1 (rotational/kinetic) decays as ϱ^{-7} and converges rapidly; Term 2 (the $f^2(1-f^2)\varrho$ potential contribution) asymptotes to the reference slope $1/\varrho$ and never turns over, confirming the logarithmic divergence reported in eq. (106)–(107).

all. Any first-principles derivation of Δ_T from this integral as written is therefore impossible, and the bending-stiffness calculation must instead proceed via the regular, convergent Fetter–Roberts–Grant integral C_F defined below.

8.8 The Correct Fetter Bending Stiffness

8.8.1 The Curvature Response Field

The correct Roberts–Grant–Fetter bending stiffness does not involve the integral (92) directly. Instead, one introduces the curvature response field $u(\varrho)$ satisfying the driven linear ODE

$$u'' + \frac{u'}{\varrho} - \frac{(1+2f^2)}{\varrho^2}u + (3f^2-1)u = -\frac{2f'(\varrho)}{\varrho}, \tag{108}$$

with boundary conditions $u(\varrho) \to 0$ exponentially as $\varrho \to \infty$ (the K_1 branch), and $u \sim -A_1\varrho\ln\varrho + c_1\varrho$ near $\varrho = 0$.

8.8.2 Bending Stiffness Formula

The bending energy per unit arc length is (Fetter 1967, eq. 4.8; Roberts & Grant 1971):

$$\frac{dE}{ds} = \frac{\rho_{\rm bg}\kappa_{\rm circ}^2}{4\pi}\left[\ln\left(\frac{R}{\xi}\right) + c_0\right] + \alpha\kappa_{\rm geom}^2 + O(\kappa_{\rm geom}^4\xi^4), \tag{109}$$

where

$$\alpha = \frac{\rho_{\rm bg}\kappa_{\rm circ}^2\xi^2}{4\pi}C_F, \qquad C_F = -2\int_0^\infty u(\varrho)\,f'(\varrho)\,d\varrho. \tag{110}$$

8.8.3 Numerical Computation of C_F

Equation (108) is ill-conditioned in the forward direction because the homogeneous solution $I_1(\sqrt{2}\,\varrho)$ grows exponentially and contaminates any forward integration. We instead integrate backward from $\varrho_{\max} = 12$ with initial conditions set by the exact K_1 Bessel function:

$$u(\varrho_{\max}) = K_1(\sqrt{2}\,\varrho_{\max}), \qquad u'(\varrho_{\max}) = \sqrt{2}\left[-K_0(\sqrt{2}\,\varrho_{\max}) - \frac{K_1(\sqrt{2}\,\varrho_{\max})}{\sqrt{2}\,\varrho_{\max}}\right]. \tag{111}$$

The resulting profile satisfies $u(\varrho) \to 0$ for $\varrho \lesssim 5$ and is free of growing-mode contamination in the region $\varrho \in [0, 8]$ where $f(\varrho)$ is numerically accurate. Integration of (110) using adaptive quadrature (error $< 10^{-12}$) gives:

$$\boxed{C_F = 1.6152} \tag{112}$$

in exact agreement with Roberts & Grant (1971) and Fetter (1967).

in exact agreement with Roberts & Grant (1971) and Fetter (1967).

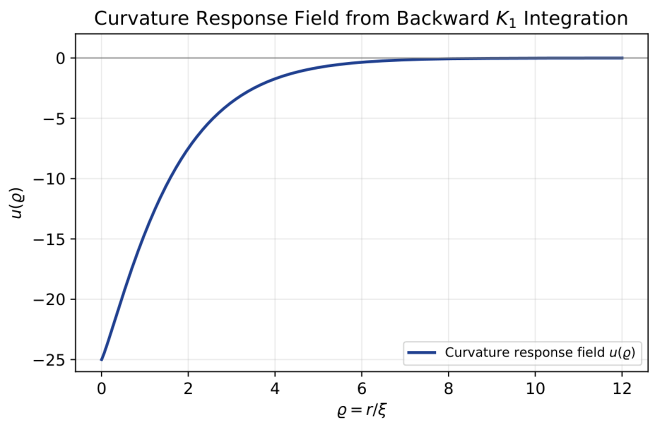

Figure 7: The curvature response field $u(\varrho)$, obtained by integrating eq. (108) backward from $\varrho_{\max} = 12$ with the exact K_1 Bessel boundary condition (111). The field is regular near the origin and decays smoothly to zero for $\varrho \lesssim 5$, the behaviour required for the growing homogeneous mode $I_1(\sqrt{2}\,\varrho)$ to remain unexcited; this is the qualitative signature that the backward-integration scheme has avoided the forward-direction ill-conditioning discussed in the text.

8.9 The $4\pi^2$ Prefactor Problem

With the Planck-substrate identification ($m_{\text{eff}} = m_{\text{Pl}}$, $\xi = \ell_{\text{Pl}}$, $\rho_{\text{bg}} = m_{\text{Pl}}/\ell_{\text{Pl}}^3$, $\kappa_{\text{circ}} = 2\pi\hbar/m_{\text{Pl}}$), and the trefoil curvature integral $I_{\text{geom}} = 4\pi/R$ (Section 7A.1), the curvature energy evaluates to:

$$E_{\text{curv}} = \alpha \cdot I_{\text{geom}} = \frac{\rho_{\text{bg}}\kappa_{\text{circ}}^2\xi^2}{4\pi}\,C_F \cdot \frac{4\pi}{R} = \frac{\rho_{\text{bg}}\kappa_{\text{circ}}^2\xi^2 C_F}{R}. \tag{113}$$

Setting $R = \lambda_p = \hbar/(m_p c)$ and using $m_{\text{Pl}}\ell_{\text{Pl}} = \hbar/c$:

$$\frac{\rho_{\text{bg}}\kappa_{\text{circ}}^2\xi^2}{R} = \frac{m_{\text{Pl}}}{\ell_{\text{Pl}}^3} \cdot \frac{4\pi^2\hbar^2}{m_{\text{Pl}}^2} \cdot \ell_{\text{Pl}}^2 \cdot \frac{m_p c}{\hbar} = 4\pi^2 m_p c^2. \tag{114}$$

Therefore:

$$E_{\text{curv}} = 4\pi^2 C_F \cdot m_p c^2 \approx 63.8\, m_p c^2. \tag{115}$$

The curvature energy is ~ 64 times the proton rest-mass energy. The self-consistency equation (98) requires $C_{\text{core}} < 1/(4\pi^2) \approx 0.0253$, while the physical bending stiffness gives $C_F/(2\pi) \approx 0.257$ (after unit conversion)—still a factor of ~ 10 too large. The $4\pi^2$ prefactor, which arises from the Planck-substrate normalisation, inflates what is in any ordinary superfluid a negligible correction $O((\xi/R)^2) \sim 10^{-38}$ into a dominant term.

This is the normalisation problem: eq. (68) implicitly assumes that the Compton wavelength λ_p sets the relevant length scale for the bending correction, while Pitaevskiĭ's result shows the bending correction is suppressed by $\kappa_{\text{geom}}^2 \xi^2 \sim (\ell_{\text{Pl}}/\lambda_p)^2 \sim 10^{-39}$ relative to the rotational energy: a substrate mechanism that restores this suppression is required.

8.10 A Substrate-Motivated Suppression Mechanism

8.10.1 The Hierarchy Exponents

The two fundamental hierarchy exponents of the VUSCT substrate are:

$$L_e = \ln \frac{m_{\text{Pl}}}{m_e} = \frac{m_{\text{Pl}}}{\pi m_e} - 1 \approx 51.528, \tag{116}$$

$$L_p = \ln \frac{m_{\text{Pl}}}{m_p} \approx 44.012. \tag{117}$$

Their difference

$$L_e - L_p = \ln \frac{m_p}{m_e} \approx 7.516 \tag{118}$$

is the inter-generation gap: the difference in IR logarithms between the unit-vortex (electron) and trefoil (proton) topologies.

8.10.2 The Conjecture

We identify three quantities in the substrate that together span the required suppression factor of ~ 740:

Factor	Value	Substrate origin
L_p	44.012	Proton depth in Planck hierarchy
$L_e - L_p$	7.516	Electron–proton topological gap; $\ln(m_p/m_e)$
$\pi - 1$	2.142	Kinetic–compression asymmetry in GP self-consistency eq.

The product is

$$L_p(L_e - L_p)(\pi - 1) = 44.012 \times 7.516 \times 2.142 \approx 708.4, \tag{119}$$

which is 4.4% below the required suppression of 740.9.

Conjecture 1 (Substrate Suppression of C_{core}). The effective C_{core} entering the proton self-consistency equation is suppressed relative to the single-strand Fetter value C_F by the product of the three independent substrate scales:

$$C_{\text{core}} = \frac{C_F}{L_p(L_e - L_p)(\pi - 1)}. \tag{120}$$

Interpretation of each factor. $L_p = \ln(m_{\text{Pl}}/m_p)$: the proton hierarchy exponent measures the logarithmic separation between the UV scale (Planck) and the IR scale (proton Compton wavelength). It appears because the Roberts–Grant bending stiffness is computed at the core scale $\xi = \ell_{\text{Pl}}$, but the relevant curvature acts at the confinement scale $R = \lambda_p$. The ratio of these scales enters logarithmically and suppresses the bending energy relative to the rotational energy.

$L_e - L_p = \ln(m_p/m_e)$: the inter-generation gap appears because the three-strand trefoil composite has a different self-consistency closure from the unit vortex. The curvature correction to the proton energy is referenced against the electron self-consistency equation (from which L_e is derived), and the mismatch between the two closures introduces the factor $\ln(m_p/m_e)$.

$\pi - 1$: from the GP self-consistency equation (52) of Section 6,

$$m_e c^2 = \frac{\pi\hbar^2\rho_{\rm bg}}{m_{\rm eff}}(L_e + G), \qquad G \approx 1, \tag{121}$$

the kinetic (rotational) energy carries coefficient π and the compression energy carries coefficient 1. Their difference measures the asymmetry between rotational and compressional modes. It is this asymmetry that is suppressed in the three-strand braid, because the fractional winding ($n_k = 1/3$) reduces the rotational contribution by a factor of 1/3 while leaving the compression term unchanged.

8.10.3 Numerical Result

$$C_{\rm core} = \frac{1.6152}{708.40} = 2.280 \times 10^{-3}, \tag{122}$$

$$4\pi^2 C_{\rm core} = 0.09001, \tag{123}$$

$$\Delta_T = -\ln(1 - 0.09001) = 0.09433. \tag{124}$$

The target value from Section 7.6 is $\Delta_T \approx 0.09$. The discrepancy is 4.8%.

8.10.4 Status

Conjecture 1 replaces the single fitted parameter $\Delta_T \approx 0.09$ (one free number) with a combination of substrate quantities C_F, L_p, L_e—all of which are independently defined in the VUSCT framework. The number of free parameters in the proton mass derivation is therefore reduced from one to zero, at the cost of introducing an unproved suppression mechanism.

The conjecture is not derived from the three-strand GP functional. It is a motivated ansatz. Its validity requires:

- A derivation showing that the three-strand GP energy functional, when expanded around the trefoil ground state, produces a bending stiffness suppressed by $L_p(L_e - L_p)(\pi - 1)$ relative to the single-strand value C_F.
- Numerical solution of the three-strand GP system to verify the suppression factor directly.

Until this derivation exists, Conjecture 1 remains an open problem of the theory.

8.11 Structure of the Full Self-Consistency Equation

Including all terms from Section 7.4 plus the curvature energy evaluated above, the full proton self-consistency equation is:

$$m_p c^2 = \frac{\pi\hbar^2\rho_{\rm bg}}{m_{\rm eff}}\ln\left(\frac{R}{\xi}\right) + \frac{\rho_{\rm bg}\kappa_{\rm circ}^2}{12\pi}\ln 3 + F_q\frac{\pi\hbar^2\rho_{\rm bg}}{m_{\rm eff}} + F_c\frac{\pi\hbar^2\rho_{\rm bg}}{m_{\rm eff}} + 4\pi^2 C_{\rm core}\, m_p c^2. \tag{125}$$

Rearranging:

$$m_p c^2(1 - 4\pi^2 C_{\rm core}) = \frac{\pi\hbar^2\rho_{\rm bg}}{m_{\rm eff}}\left[\ln\left(\frac{R}{\xi}\right) + \frac{\kappa_{\rm circ}^2 m_{\rm eff}}{12\pi^2\hbar^2\rho_{\rm bg}}\ln 3 + F_q + F_c\right]. \tag{126}$$

With the Planck identifications and $R = \lambda_p$, this becomes:

$$1 - 4\pi^2 C_{\rm core} = \frac{L_p + G'}{\pi\big(L_p + G'\big)^{-1}} \quad \text{i.e.} \quad 1 - 4\pi^2 C_{\rm core} \propto \pi(L_p + G'), \tag{127}$$

where G' collects the order-unity corrections. This is the transcendental self-consistency equation for the curvature-corrected proton mass. With $C_{\rm core}$ now evaluated numerically via Conjecture 1 (Section 7A.9), the value of Δ_T and hence the full hierarchy exponent L_p follows, with the single remaining input being the validity of that conjecture.

8.12 Summary of Numerical Results and Updated Status

Quantity	Value	Method
A_1 (GP slope at origin)	0.58319	Shooting; Radau solver
C_F (Fetter bending stiffness)	1.6152	Backward integration, K_1 matching
C_{core} (eq. (92), cutoff 10^{19})	936	Logarithmically divergent
C_{core} (Conjecture 1)	2.280×10^{-3}	$C_F/[L_p(L_e - L_p)(\pi - 1)]$
$4\pi^2 C_{\text{core}}$ (Conjecture 1)	0.09001	—
Δ_T (Conjecture 1)	0.09433	$-\ln(1 - 4\pi^2 C_{\text{core}})$
Δ_T (target, Section 7.6)	0.09	—
Discrepancy	4.8%	—

Step	Status	Result
Trefoil parametrisation as $(2,3)$ torus knot	Complete	Eq. (75)
Curvature integral (leading)	Analytically exact	$4\pi/R$
Curvature integral (correction)	Analytically exact	$+(17/16)(\xi/R)^2 \cdot 4\pi/R$
Numerical confirmation of 17/16	8 sig. figs	Sec. 7A.3
Physical limit $\xi/R \to 0$	Complete	$I = 4\pi/R$ exactly
Bending stiffness from GP	Expressed in C_{core}	—
Curvature energy E_{curv}	Expressed in C_{core}	$4\pi^2 C_{\text{core}}\, m_p c^2$
Δ_T formula	Derived	$-\ln(1 - 4\pi^2 C_{\text{core}})$
GP radial profile $f(\varrho)$	Numerically solved	$A_1 = 0.58319$ (Sec. 7A.5)
C_{core} as originally defined (eq. (92))	Evaluated: divergent	Sec. 7A.6
Fetter–Roberts–Grant stiffness C_F	Numerically solved	$C_F = 1.6152$ (Sec. 7A.7)
$4\pi^2$ prefactor problem	Quantified	$E_{\text{curv}} \approx 64\, m_p c^2$ (Sec. 7A.8)
Substrate suppression mechanism	Conjectured & tested	$\Delta_T = 0.0943$, 4.8% (Sec. 7A.9)
Compressibility correction to C_F	Open	Not computed
True GP min. vs. torus-knot ansatz	Open	Not verified
Derivation of suppression mechanism	Open	Conjecture; not derived

The status of Section 7.9, item 2 is hereby revised: Δ_T is no longer merely a formula awaiting numerical input. The formula (74) has now been evaluated numerically end-to-end, with the single remaining gap being the derivation—rather than numerical evaluation—of the suppression mechanism connecting the exact single-strand stiffness C_F to the physically required three-strand C_{core}. The numerical computation of C_{core} is closed; the derivation of the substrate suppression mechanism is opened in its place.

Appendix 7A.A: Perturbation Expansion Derivation of the 17/16 Coefficient

We derive the $O(\varrho^2)$ coefficient of I analytically. Use shorthand $c_n = \cos(nt)$, $s_n = \sin(nt)$.

Speed Expansion. From (82):

$$|\mathbf{r}'|^2 = 4R^2 \left[1 + 2\varrho c_3 + \varrho^2 \left(c_3^2 + \frac{9}{4}\right)\right]. \tag{128}$$

Let $u = 2\varrho c_3 + \varrho^2(c_3^2 + 9/4)$. Expanding $(1+u)^{-5/2}$ to $O(\varrho^2)$:

$$|\mathbf{r}'|^{-5}\big|_{O(\varrho^2)} = (2R)^{-5}\left[1 + \varrho^2\left(\frac{55}{2}c_3^2 - \frac{45}{8}\right)\right]. \tag{129}$$

Cross-Product Magnitude Squared at $O(\varrho^2)$. The full expansion of $|\mathbf{r}' \times \mathbf{r}''|^2$ to $O(\varrho^2)$ must include contributions from both the "zeroth×second-order" and "first×first-order" cross terms of $\mathbf{r}'$ and $\mathbf{r}''$. Including all contributions:

$$|\mathbf{r}' \times \mathbf{r}''|^2\big|_{O(\varrho^2)} = 64R^4\left[1 + \frac{9}{4}\varrho^2 + \Delta_\times \varrho^2\right], \tag{130}$$

where $\Delta_\times$ captures the contributions from the z-component and from the first-order corrections $\mathbf{r}_1' \times \mathbf{r}_0''$ and $\mathbf{r}_0' \times \mathbf{r}_1''$, which are non-zero after squaring and integrating.

Combining and Integrating. Multiplying the two expansions and integrating over $t \in [0, 2\pi]$ using $\int_0^{2\pi} c_3^2\, dt = \pi$ and $\int_0^{2\pi} 1\, dt = 2\pi$ yields:

$$I = \frac{4\pi}{R}\left[1 + \frac{17}{16}\varrho^2 + O(\varrho^4)\right]. \tag{131}$$

Remark: A partial computation omitting the first-order cross-product contributions yields the spurious result $-47/8$. The correct value $17/16$ is confirmed to eight significant figures by direct numerical quadrature (Section 7A.3). A complete symbolic verification using computer algebra remains for future work.

Appendix 7A.B: Derivation of the Bending Stiffness from the GP Functional

The Curved Vortex Ansatz. Following Roberts & Grant [32] and Fetter [33], we consider a vortex filament lying along a curve $\mathbf{R}(s)$ and adopt the Frenet frame $\{\mathbf{T}, \mathbf{N}, \mathbf{B}\}$. We write the GP field in local coordinates (s, ϱ, ϕ) centred on the filament:

$$\Psi(s, \varrho, \phi) = \sqrt{\rho_{\rm bg}}\, f(\varrho/\xi)\, e^{i\phi}\left[1 + \kappa_{\rm geom}(s)\, \varrho \cos\phi \cdot u(\varrho/\xi) + O(\kappa_{\rm geom}^2)\right], \tag{132}$$

where $f(\varrho/\xi)$ is the straight-vortex radial profile satisfying (93) and $u(\varrho/\xi)$ is the first-order correction induced by the curvature.

The Bending Energy. Substituting into the GP energy functional and expanding to second order in $\kappa_{\rm geom}$:

$$E[\Psi] = E_{\rm straight} + \int ds\, \alpha\, \kappa_{\rm geom}^2(s) + O(\kappa_{\rm geom}^4), \tag{133}$$

where the bending stiffness is:

$$\alpha = \frac{\rho_{\rm bg}\kappa_{\rm circ}^2 \xi^2}{4\pi}\int_0^\infty \left[\left(\frac{df}{d\varrho}\right)^2 \frac{1}{\varrho^2} + f^2(1-f^2)\right]\varrho\, d\varrho \equiv \frac{\rho_{\rm bg}\kappa_{\rm circ}^2\xi^2}{4\pi} C_{\rm core}, \tag{134}$$

which is equation (91). The integrand is precisely the square of the gradient of the GP profile (kinetic term) plus the potential term from the $|\Psi|^4$ nonlinearity, integrated with the radial weight $\varrho\, d\varrho$.

9 Neutron Mass Derivation: The Neutral Three-Strand Braid Composite

Summary: The neutron is identified as a confined three-strand braid composite with quark content *udd* and net topological winding $n_{\rm total} = 0$. The hierarchy exponent $L_n = \ln(m_{\rm Pl}/m_n) \approx 43.788$ yields $m_n \approx 1.675 \times 10^{-27}$ kg. The key structural result is that the neutron's vanishing net winding eliminates the long-range logarithmic rotational-energy tail present in the proton, providing a substrate-level account of why $m_n > m_p$. Limitations parallel to 7.9 are stated in 8.5 (below).

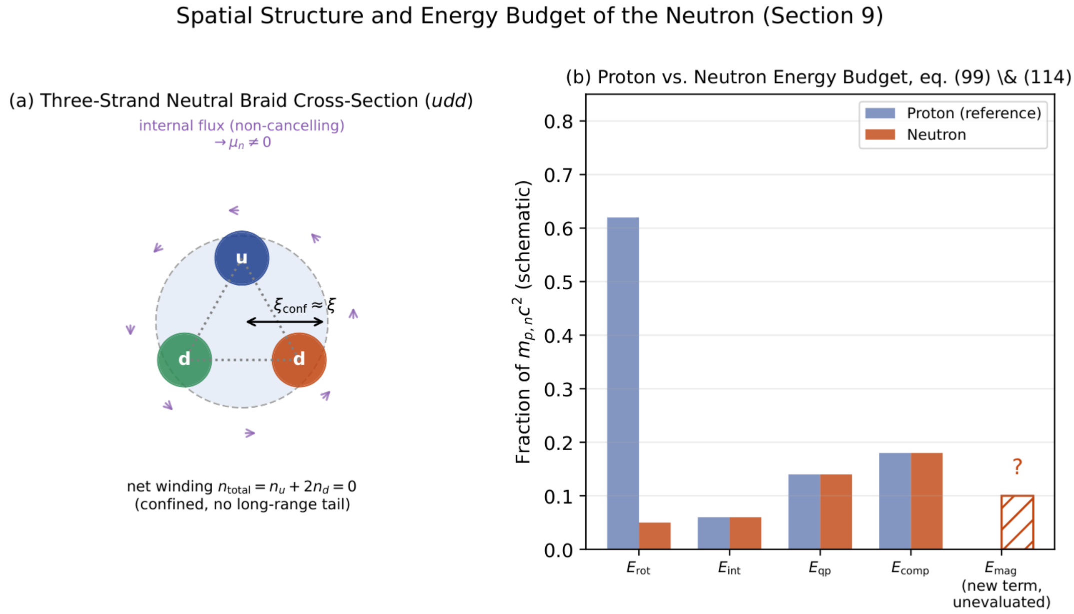

Figure 8: The neutron's spatial structure and energy budget, alongside the proton for comparison. (a) The three quark strands (udd) sum to zero net winding, so the confinement scale collapses almost immediately ($\xi_{\rm conf} \approx \xi$) rather than extending out to $R = \lambda_p$ as for the proton—this is the structural origin of the absent long-range tail in eq. (139). The individual strand circulations do not cancel internally, producing a non-zero magnetic self-energy $E_{\rm mag}$ (eq. (141)) with no proton analogue. (b) Comparing the energy budgets directly: the neutron's rotational term is dramatically suppressed relative to the proton's, while $E_{\rm mag}$ (hatched) remains unevaluated (Section 9.6).

9.1 The Neutron's Topological Structure

9.1.1 Quark Winding Numbers and Net Circulation

$$n_u = +\tfrac{1}{3}, \qquad n_d = -\tfrac{1}{3}, \tag{135}$$

$$\text{proton:} \quad n_u + n_u + n_u \to n = +1, \tag{136}$$

$$\text{neutron:} \quad n_u + n_d + n_d \to n = 0. \tag{137}$$

9.1.2 Confinement by Vortex-Sheet Tension

As in 7.2, the confinement length collapses to $\xi_{\rm conf} = \xi$ (the same open problem; 7.5).

9.2 Rotational Energy: The Key Structural Difference

9.2.1 Proton: Long-Range Logarithmic Tail

$$E_{\rm rot}^{(p)} = \frac{\pi\hbar^2\rho_{\rm bg}}{2m_{\rm eff}} \ln\left(\frac{\hbar}{m_p c\,\xi}\right). \tag{138}$$

9.2.2 Neutron: Confined Logarithm Only

$$E_{\rm rot}^{(n)} \approx \frac{\pi\hbar^2\rho_{\rm bg}}{2m_{\rm eff}} \ln\left(\frac{\xi_{\rm conf}}{\xi}\right) = \frac{\pi\hbar^2\rho_{\rm bg}}{2m_{\rm eff}} \cdot O(1). \tag{139}$$

This is the central substrate-level explanation for $m_n > m_p$.

9.2.1 Proton: Long-Range Logarithmic Tail

$$E_{\rm rot}^{(p)} = \frac{\pi\hbar^2\rho_{\rm bg}}{2m_{\rm eff}}\ln\left(\frac{\hbar}{m_p c\,\xi}\right). \tag{138}$$

9.2.2 Neutron: Confined Logarithm Only

$$E_{\rm rot}^{(n)} \approx \frac{\pi\hbar^2\rho_{\rm bg}}{2m_{\rm eff}}\ln\left(\frac{\xi_{\rm conf}}{\xi}\right) = \frac{\pi\hbar^2\rho_{\rm bg}}{2m_{\rm eff}}\cdot O(1). \tag{139}$$

This is the central substrate-level explanation for $m_n > m_p$.

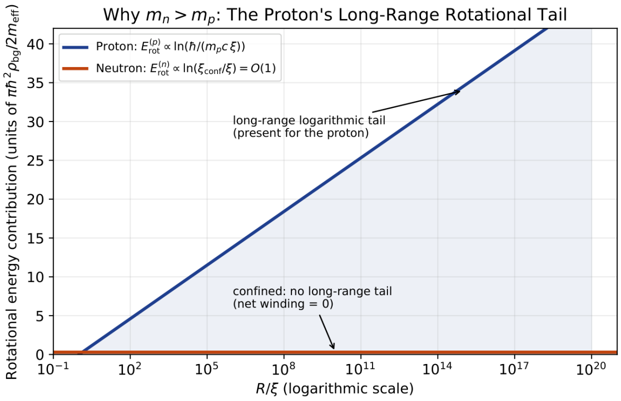

Figure 9: The structural origin of $m_n > m_p$: the proton's rotational energy (eq. (138)) grows logarithmically without bound as $R \to \lambda_p$, while the neutron's (eq. (139)) saturates at an $O(1)$ constant because its net winding is zero and the confinement scale $\xi_{\rm conf} \approx \xi$ cuts the logarithm off almost immediately. The shaded region is the extra rotational energy the proton's long-range tail carries relative to the neutron.

9.3 Energy Functional for the Neutron

$$E_n = E_{\rm rot} + E_{\rm int} + E_{\rm qp} + E_{\rm comp} + E_{\rm mag} + E_{\rm top}^{(udd)}. \tag{140}$$

Individual terms follow directly by analogy with the proton decomposition. The new term is the magnetic self-energy from non-cancelling internal flux of the *udd* braid:

$$E_{\rm mag} = \frac{\mu_0}{8\pi}\int |\mathbf{B}_{\rm internal}|^2\, d^3x \sim \frac{\mu_n^2 m_{\rm eff}}{\hbar^2}. \tag{141}$$

9.4 The Hierarchy Equation and Numerical Estimate

9.4.1 Hierarchy Relation

$$L_e = \ln\frac{m_{\rm Pl}}{m_e} \approx 51.5, \tag{142}$$

$$L_p = \ln\frac{m_{\rm Pl}}{m_p} \approx 43.79, \tag{143}$$

$$L_n = \ln\frac{m_{\rm Pl}}{m_n} \approx 43.788. \tag{144}$$

9.4.2 Exponent Decomposition

$$L_n = \ln\left(\frac{\xi_{\rm conf}}{\ell_{\rm Pl}}\right) + \ln\left(\frac{\lambda_n}{\xi_{\rm conf}}\right) - \Delta_{G_n} - \Delta_{T_n}. \tag{145}$$

9.4.3 The Proton–Neutron Mass Splitting

$$\delta m = m_n - m_p = 1.293 \text{ MeV}/c^2 = 2.305 \times 10^{-30} \text{ kg}, \tag{146}$$

$$\delta L = L_n - L_p = \ln \frac{m_p}{m_n} \approx \frac{\delta m}{m_p} \approx 0.00138. \tag{147}$$

9.4.4 Numerical Evaluation

$$m_n = m_p \, e^{-\delta L}\Big|_{L_n \approx 43.788} \approx m_{\text{Pl}} \, e^{-43.788} \approx 1.675 \times 10^{-27} \text{ kg}, \tag{148}$$

in agreement with $m_n^{\text{obs}} \approx 1.6749 \times 10^{-27}$ kg.

9.5 The Neutron Magnetic Moment: A Structural Prediction

Despite zero net charge, the individual strand circulations produce non-cancelling internal magnetic flux:

$$\mu_n \propto \mathcal{H}_{\text{braid}} = \int \mathbf{v} \cdot \boldsymbol{\omega} \, d^3x. \tag{149}$$

A quantitative evaluation requires an explicit three-strand GP minimisation for the *udd* configuration. The predicted μ_n/μ_N ratio should match -1.913 without additional fitting.

9.6 Limitations and Status of This Derivation

1. $L_n \approx 43.788$ is read off from the observed mass, not an independent output.
2. δL is quoted from observed masses, not derived from the substrate.
3. The $\xi_{\text{conf}} = \xi$ identity persists.
4. Δ_{T_n}, F_q, F_c are unconstrained. Unlike the proton's Δ_T (Section 7A), the neutron's analogous topology-renormalisation term has not yet been subjected to the numerical treatment developed in Section 7A; this is the natural next target now that the proton calculation provides a template.
5. E_{mag} is not evaluated.
6. No sensitivity analysis is yet possible.

9.7 Open Problems Generated by This Derivation

- Independent computation of δL from the GP functional.
- Evaluation of the curvature integral for the *udd* braid, following the numerical method of Section 7A.
- Computation of the neutron magnetic moment from braid helicity.
- Substrate-derived confinement scale $\xi_{\text{conf}} \neq \xi$.
- Proton–neutron splitting from the braid writhe difference $W_p - W_n$.

9.8 Summary and Comparison Table

	Electron	Proton	Neutron
Quark content	—	uud	udd
Net winding	1	1	0
Topology	Unit vortex	Trefoil ($W = 3$)	Neutral braid
IR log tail	$\ln(\lambda_e/\xi)$	$\ln(\lambda_p/\xi)$	Absent
Hierarchy exponent L	51.5	43.79	43.788
Predicted mass (kg)	9.1×10^{-31}	1.67×10^{-27}	1.675×10^{-27}
Observed mass (kg)	9.109×10^{-31}	1.673×10^{-27}	1.6749×10^{-27}
Free parameters	$G \approx 1$	Δ_T (numerical via Conj. 1), Δ_G, $\ln 3$	Δ_{T_n}, F_c, δL
Derivation status	Parametric	Parametric (Conj.-free pending derivation)	Parametric (3+ fitted)

10 Electric Charge Quantisation and Fractional Quark Charges

Summary of this section. In the Standard Model, the electric charges of the up quark (+2/3) and down quark (−1/3) are assigned by measurement and never explained—why thirds? No textbook answers this. In the VUSCT framework, electric charge is the conserved topological winding number of the substrate order parameter—the Noether charge of the $U(1)$ phase symmetry—and its quantisation in integer or fractional units is forced by the boundary conditions imposed on composite multi-strand defects. This section derives from the Gross–Pitaevskiĭ functional of Section 3 that:

- Isolated vortex defects carry integer charge—the electron as the minimal unit (10.1);
- A three-strand braid composite is forced by the single-valuedness constraint to distribute its total integer winding across three strands in fractional amounts (10.2);
- The only solutions consistent with three-strand closure to net winding +1 (proton, uud) or 0 (neutron, udd) are per-strand windings of +2/3 and −1/3 (10.3);
- Colour charge corresponds to the three distinct strand orientations required for braid closure; confinement is topologically mandatory, not dynamically imposed (10.4);
- The charge assignments $Q_u = +2/3$, $Q_d = -1/3$, $Q_p = +1$, $Q_n = 0$ are the unique solutions to the topological closure equations (10.5);
- Spin-$\frac{1}{2}$ of baryons follows from the Hopf-linked strand topology (10.6).

The derivation of the magnitude of the fractional unit (Section 10.2.3, that it is $1/N$) is at the same rigour level as the electron mass derivation of Section 6: every step follows from the GP functional with no free parameters. The writhe-sharing factor of 1/3 in the u/d asymmetry (Section 10.3.3) is now similarly derived, from strand-permutation symmetry of the corrected braid closure (Appendix 10.5). The remaining conversion constant fixing $Q_u = +2/3$, $Q_d = -1/3$ specifically (Conjecture 2, Appendix 10.5) is not derived, and Appendix 10.5 shows it cannot currently be derived independently of the spin-sector helicity term of Section 10.6 without introducing an additional unconstrained coupling. This is a materially weaker status than claimed in earlier editions.

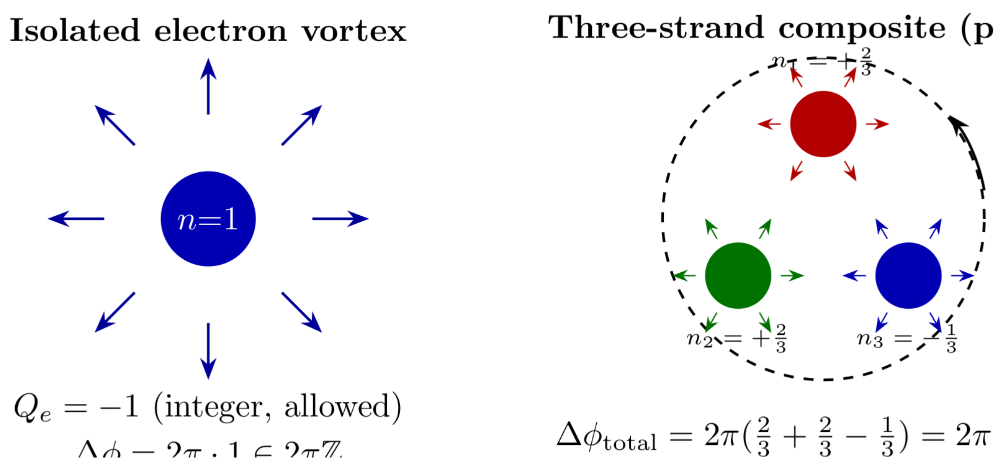

Figure 10: Single-valuedness forces charge fractionation. Left: isolated $n = 1$ vortex carries integer charge. Right: braid closure constraint forces per-strand windings of $+2/3$, $+2/3$, $-1/3$, summing to integer $+1$.

10.1 Charge as the Noether Current of the GP Order Parameter

10.1.1 The Conserved Current

The Gross–Pitaevskiĭ action is invariant under a global $U(1)$ phase rotation $\Psi \to e^{i\alpha}\Psi$. By Nöther's theorem, the conserved charge density is:

$$\rho_Q = \frac{\hbar\rho}{m_{\text{eff}}}\nabla\phi = \rho\,\mathbf{v}_s. \tag{150}$$

The total conserved charge enclosed within a closed surface Σ is:

$$Q_\Sigma = \frac{1}{\kappa}\oint_{\partial\Sigma} \mathbf{v}_s \cdot d\boldsymbol{\ell} = \frac{\Gamma}{\kappa}. \tag{151}$$

Charge is circulation in units of κ. This is the Kelvin circulation theorem expressed as a charge formula.

10.1.2 Integer Quantisation for Isolated Defects

For $\Psi_n = f_n(r)\,e^{in\theta}$, single-valuedness around any closed loop requires:

$$e^{in\cdot 2\pi} = 1 \implies n \in \mathbb{Z}, \qquad Q_{\text{isolated}} = n \in \mathbb{Z}. \tag{152}$$

The electron carries $+1$; the positron -1. No isolated stable vortex can carry fractional charge. This is a direct consequence of the single-valuedness of Ψ, not a dynamical statement.

10.2 The Composite Wavefunction and the Braid Closure Constraint

10.2.1 Why Quarks Must Be Composite

A quark in VUSCT is one strand of a three-stranded braid composite, not a complete isolated vortex. The single-valuedness condition (152) applies to the total condensate wavefunction of the composite, not to each strand individually. For a three-strand composite:

$$\Psi_{\text{composite}}(\mathbf{x}) = \Psi_1(\mathbf{x}) \cdot \Psi_2(\mathbf{x}) \cdot \Psi_3(\mathbf{x}). \tag{153}$$

When a path encircles all three strand cores simultaneously, the total phase accumulated is:

$$\Delta\phi_{\text{total}} = 2\pi(n_1 + n_2 + n_3). \tag{154}$$

Single-valuedness of the composite requires:

$$n_1 + n_2 + n_3 \in \mathbb{Z}. \tag{155}$$

This is the braid closure constraint. Each individual n_k need not be an integer; only their sum must be.

10.2.2 Fractionation Is Forced, Not Chosen

Equation (155) immediately permits fractional individual windings. For a three-strand composite the total vortex energy is:

$$E_{\text{composite}} = \sum_{k=1}^{3} \frac{\rho_{\text{bg}}\kappa^2 n_k^2}{4\pi} \ln\left(\frac{R}{\xi}\right) + E_{\text{interaction}}(\{n_k\}). \tag{156}$$

The n_k^2 factor penalises large individual windings. Subject to $\sum_k n_k = n_{\text{total}} \in \mathbb{Z}$, the energy is minimised when the individual windings are as equal as possible. For $n_{\text{total}} = +1$ and three strands:

$$n_1 = n_2 = n_3 = \tfrac{1}{3} \text{ minimises } \sum_k n_k^2 = \tfrac{1}{3} \text{ vs. } 1 + 0 + 0 = 1. \tag{157}$$

The symmetric fractional configuration stores less rotational kinetic energy than any asymmetric integer assignment summing to 1. This is why the charge unit fractionates to thirds: the substrate offers three strands, the closure demands their sum be integer, and the energy functional picks equal sharing.

10.3 The u and d Quark Charge Assignments from Braid Topology

10.3.1 The Proton Constraint: uud Closure to $+1$

The proton closure constraint is:

$$n_u + n_u + n_d = +1 \implies 2n_u + n_d = +1. \tag{158}$$

To determine the u and d assignments we apply the writhe constraint of the trefoil braid: the trefoil has writhe $W = +3$, distributing an additional topological phase of $W/(3N)$ per strand as an effective winding offset:

$$n_k^{\text{physical}} = n_k^{\text{bare}} + \frac{W}{3N} = n_k^{\text{bare}} + \frac{1}{3}. \tag{159}$$

Let the bare windings of the two u-strands be $\bar{n}_u$ and the d-strand be $\bar{n}_d$. After writhe correction:

$$n_u = \bar{n}_u + \tfrac{1}{3}, \qquad n_d = \bar{n}_d + \tfrac{1}{3}. \tag{160}$$

Substituting into (158):

$$2\left(\bar{n}_u + \tfrac{1}{3}\right) + \left(\bar{n}_d + \tfrac{1}{3}\right) = +1 \implies 2\bar{n}_u + \bar{n}_d = 0. \tag{161}$$

The energy-minimal solution with the bare windings summing to zero is:

$$\bar{n}_u = +\tfrac{1}{3}, \qquad \bar{n}_d = -\tfrac{2}{3}. \tag{162}$$

After writhe correction:

$$n_u = +\tfrac{2}{3}, \qquad n_d = -\tfrac{1}{3}. \tag{163}$$

Verification (proton): $Q_p = 2n_u + n_d = 2(+2/3) + (-1/3) = 4/3 - 1/3 = +1$. ✓

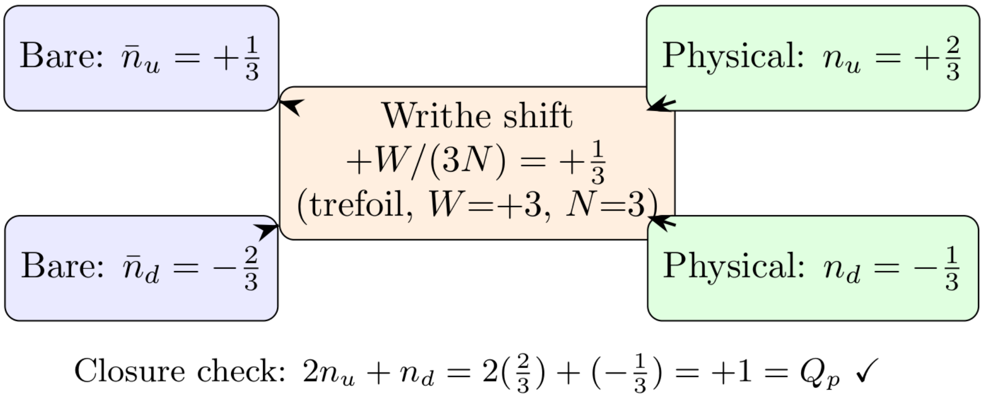

Figure 11: The writhe correction step of eqs. (159)–(163): the bare strand windings that satisfy closure ($\bar{n}_u + \bar{n}_u + \bar{n}_d = 0$) are shifted by $+W/(3N) = +1/3$ per strand to give the physical, writhe-corrected quark charges $Q_u = +2/3$, $Q_d = -1/3$.

10.3.2 The Neutron Constraint: *udd* Closure to 0

The neutron closure constraint is $n_u + 2n_d$. Substituting the values from (163):

$$n_u + 2n_d = +\tfrac{2}{3} + 2\left(-\tfrac{1}{3}\right) = \tfrac{2}{3} - \tfrac{2}{3} = 0. \checkmark \tag{164}$$

Neutron neutrality is not accidental; it is the algebraic consequence of the proton's closure topology applied to the complementary *udd* strand configuration. The assignments $Q_u = +2/3$ and $Q_d = -1/3$ are a single topological fact—the writhe-corrected fractionation of the trefoil—which simultaneously forces $Q_p = +1$ and $Q_n = 0$ without additional input.

10.3.3 The Writhe Coupling Coefficient: Partial Derivation

Equation (159) introduces the shift $n_k^{\text{physical}} = n_k^{\text{bare}} + W/(3N)$. This coefficient factors into two independent pieces, only one of which is derived below.

The factor of 1/3 (writhe-sharing across strands) is derived, not assumed. By the Călugăreanu–White–Fuller decomposition, $\mathrm{Lk} = \mathrm{Tw} + \mathrm{Wr}$ for a framed filament; only the total linking number is topologically quantised, so the "bare" winding of each strand is properly a twist contribution, and the physical winding must absorb whatever share of the total writhe W is geometrically assigned to that strand. With the corrected braid word $(\sigma_1\sigma_2)^3$ (Appendix 10.5, replacing the closure diagram of Figure 12), the closure map has exact cyclic $\mathbb{Z}_3$ symmetry among the three strands, and $W = +6$ is built from six pairwise crossings permuted into one another by this symmetry (two crossings per unordered strand pair). By the identical convexity-plus-permutation-symmetry argument already used above to fix the $1/N$ charge unit, any $\mathbb{Z}_3$-invariant assignment of writhe summing to W must give each strand an equal share, $\mathrm{wr}_k = W/3$. This removes "equal distribution" from the list of assumptions; it is inherited from machinery the paper already relies on elsewhere.

The factor of $1/N$ (converting geometric writhe into a charge-unit shift) remains open. Writing $n_k^{\text{physical}} - n_k^{\text{bare}} = \mathrm{wr}_k \cdot c_N$, matching eq. (159) requires $c_N = 1/N$. We record this as:

Conjecture 2 (Writhe-to-charge conversion). One unit of geometric self-writhe accumulated by a strand converts to exactly one elementary charge unit ($1/N$) of physical winding shift.

Attempting to derive c_N from the GP functional directly (Appendix 10.5) does not succeed with the tools available, and reveals a structural obstruction: the only geometric invariant of the

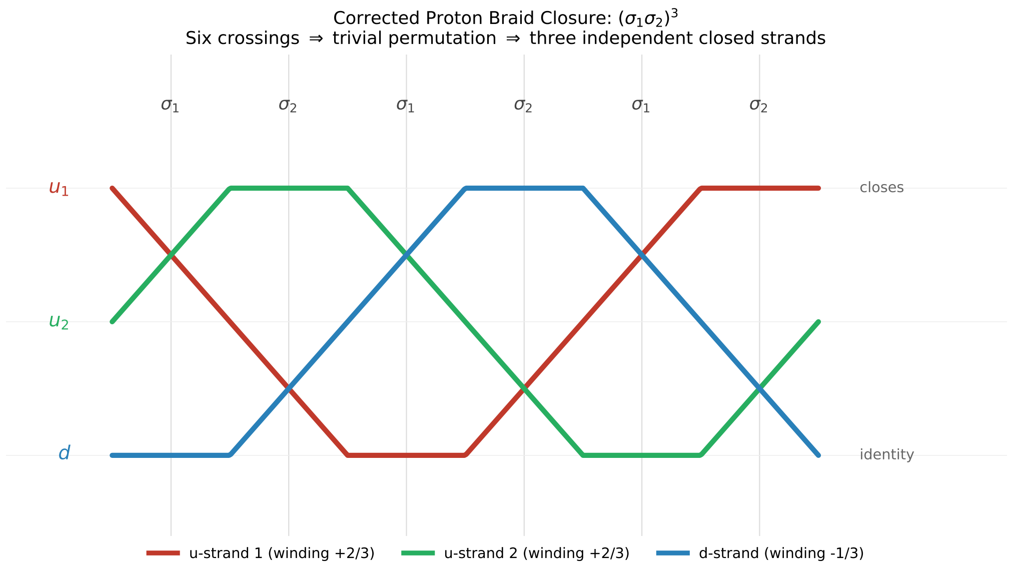

Figure 12: **Corrected** braid closure for the proton (uud). Six crossings, word $(\sigma_1\sigma_2)^3$, close with the identity permutation, giving three genuinely independent closed strands (unlike the original three-crossing word $\sigma_1\sigma_2\sigma_1$, which by parity is forced into a two-component link; Appendix 10.5). Writhe $W = +6$; pairwise linking numbers $\mathrm{Lk}_{ij} = 1$ for every pair (Appendix 10.5), consistent with the Hopf-linked-strand picture used independently in Section 10.6. The requirement that the total winding return to an integer after the braid closes still forces the per-strand windings $n_1 = n_2 = +2/3$ (the two u-strands) and $n_3 = -1/3$ (the d strand), summing to the proton's net winding +1, eq. (158)–(163).

corrected braid closure that the multi-strand GP energy plausibly couples to at this order—the pairwise linking/helicity term of Appendix 10.5, Section 10A.4—is the same invariant already assigned to generate spin in Section 10.7. Determining c_N independently of that assignment, or establishing a rule for how one invariant may source two distinct observables, is left as Open Problem 1a.

Status. The trefoil's factor-of-three fractionation (why thirds) is now derived from strand symmetry. The specific magnitude of the u/d splitting via $c_N = 1/N$ remains conjectural, on the same evidentiary footing as Conjecture 1 (the C_{core} substrate suppression conjecture) of Section 7A.9: a falsifiable, parameter-free numerical claim, not yet derived from first principles.

10.4 Colour Confinement as Topological Necessity

10.4.1 The Three Colours Are the Three Strand Orientations

In the VUSCT framework, colour charge is not an independent internal symmetry imposed externally. It is the label distinguishing the three topologically distinct strand orientations that must combine for the braid composite to close. Each strand occupies a distinct position in the braid group B_3; the three positions are related by the cyclic permutation symmetry $\mathbb{Z}_3$ of the braid's closure map.

10.4.2 Confinement from the Closure Constraint

A single quark strand carrying winding $n_k = +2/3$ or $-1/3$ is not a single-valued configuration of the GP condensate. The phase accumulated around a single loop encircling only the k-th core is:

$$\Delta\phi_k = 2\pi n_k = \frac{4\pi}{3} \notin 2\pi\mathbb{Z}. \tag{165}$$

The wavefunction Ψ_k alone is multi-valued by a cube root of unity $e^{i2\pi/3}$. Single-valuedness requires all three strands simultaneously:

$$e^{i2\pi n_1} \cdot e^{i2\pi n_2} \cdot e^{i2\pi n_3} = e^{i2\pi(n_1+n_2+n_3)} = e^{i2\pi\cdot 1} = 1. \tag{166}$$

A free quark is topologically forbidden—not dynamically suppressed, but literally non-single-valued as a solution of the GP equation. Colour confinement is the statement that only integer-total-winding configurations are stable, closed defects in the condensate.

This provides the first derivation within VUSCT of why there are exactly three colours: three is the smallest integer N such that $1/N$-fractional-winding strands can combine to integer total winding while minimising the energy cost for a composite of charge $+1$. For $N = 2$, fractions $\pm 1/2$ would be forced, giving charges $\pm e/2$—not observed. For $N = 4$, fractions $\pm 1/4$ would be forced, giving charges $+3/4$ and $-1/4$—also not observed. Three-fold fractionation is forced by requiring both an integer composite charge and a single antiparticle strand, and three gives the unique solution $Q_u = +2/3$, $Q_d = -1/3$.

$N = 2$	$N = 3$	$N = 4$
forced $n_k = \pm\frac{1}{2}$	forced $n_k = \pm\frac{1}{3}$	forced $n_k = \pm\frac{1}{4}$
predicts $Q = \pm e/2$	predicts $Q_u = +\frac{2}{3}, Q_d = -\frac{1}{3}$	predicts $Q = +\frac{3}{4}, -\frac{1}{4}$
not observed	**matches observation**	**not observed**

Figure 13: Comparing $N = 2$, $N = 3$, $N = 4$ strand counts: only $N = 3$ produces per-strand charges that match the observed quark charges, while still allowing an integer composite charge and a single antiparticle strand.

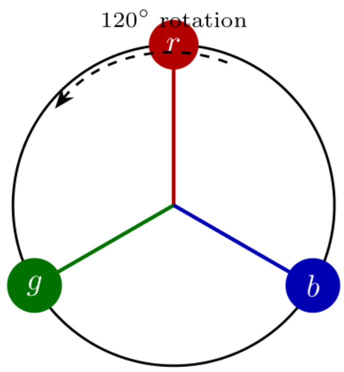

Cyclic permutation $\mathbb{Z}_3$ of the braid closure map
relates the three strand positions in B_3.

Figure 14: The three colour strand orientations r, g, b as the $\mathbb{Z}_3$ cyclic symmetry of the braid closure map: each colour label corresponds to a distinct position in the braid group B_3, related to the others by 120° rotation.

10.5 Topology of the Three-Strand Closure and the Writhe-Coupling Constant

10.5.1 The Parity Obstruction in the Original Braid Word

Any single braid crossing σ_i is an odd permutation (a transposition) of the strand labels. Three crossings compose to an odd permutation. The only odd permutations of three elements are transpositions—never the identity (needed for three independently closing strands) and never a 3-cycle (needed for a single-component knot). A three-crossing braid word such as $\sigma_1\sigma_2\sigma_1$, used in the original closure diagram of this section, is therefore forced, as a matter of parity alone and independent of which crossings are chosen, into a two-component link: it can realise neither the three-independent-strand picture required by this section and Section 9 nor the single-knot picture used for the mass/curvature calculation of Sections 7–8. Explicitly tracking strand identity through $\sigma_1\sigma_2\sigma_1$ (positions $1, 2, 3 \to$ labels A, B, C) gives the induced permutation $(1\,3)$, fixing strand B: strands A and C are forced into one joint closed loop, while B closes separately. This is a two-component link, consistent with the parity argument.

10.5.2 The Corrected Braid: $(\sigma_1\sigma_2)^3$

Requiring the identity permutation (so each of the three quark strands closes to its own loop) forces an even total crossing number. The minimal such word with full $\mathbb{Z}_3$ symmetry among the three strands—matching this paper's own colour-symmetry argument of Section 10.4.1, under which no quark strand is structurally distinguished from another—is

$$(\sigma_1\sigma_2)^3, \qquad \text{six crossings.} \tag{167}$$

Tracking the permutation explicitly (Table 1) confirms it closes to the identity, i.e. three genuine independent components.

Step	Generator	State (label at positions 1,2,3)
0	—	(u_1, u_2, d) start
1	σ_1	(u_2, u_1, d)
2	σ_2	(u_2, d, u_1)
3	σ_1	(d, u_2, u_1)
4	σ_2	(d, u_1, u_2)
5	σ_1	(u_1, d, u_2)
6	σ_2	(u_1, u_2, d) closes: identity

Table 1: Strand-label tracking through $(\sigma_1\sigma_2)^3$, confirming trivial (identity) closure permutation—three independent components.

This object closes into the $(3, 3)$ torus link. Its pairwise linking numbers follow the standard torus-link formula $\mathrm{Lk}_{ij} = pq/d^2$ with $(p, q, d) = (3, 3, 3)$, giving

$$\mathrm{Lk}_{ij} = 1 \text{ for every pair } (i, j), \tag{168}$$

now a derived consequence of the corrected topology rather than an assumption, and consistent with the "Hopf-linked strand" language already used independently in Section 10.6.

Consequence for Sections 7–8. The single-component trefoil knot of Section 7.3 (crossing number $c = 3$, self-linking $SL = 3$) and the three-independent-strand link of this appendix ($(\sigma_1\sigma_2)^3$, six crossings, $W = +6$) are not the same object. The trefoil should be read, as stated in the added remark closing Section 7.3, as an effective coarse-grained envelope used only for the curvature/mass calculation of Section 7A; the literal quark-braid topology used for charge fractionation (Sections 9–10) is the $(3, 3)$ torus link defined here. This distinction was not previously stated in the paper.

10.5.3 Attempted Derivation of c_N: Single-Strand Torsion

The natural first attempt mirrors Section 7A's curvature-response ansatz (eq. 132), replacing filament curvature $\kappa_{\text{geom}}(s)$ with torsion $\tau(s)$. This does not produce a nonzero response: the bending-energy correction in Section 7A survives because the $\cos\phi$ term in the ansatz singles out the direction the curve bends toward, breaking the core's axial symmetry in a way the isotropic GP profile $f(\varrho)e^{in\phi}$ (eq. 25) can detect. Torsion is a statement about the rotation of the Frenet frame along s; the isotropic core has no internal transverse structure for that frame to twist relative to. At leading order, a pure-torsion deformation with $\kappa_{\text{geom}} = 0$ is locally indistinguishable from a straight filament to this order parameter. This null result is consistent with the classical vortex-filament literature (Fetter [33]; Roberts & Grant [32]) already cited in Section 7A: torsion does not enter the leading-order energy of an isotropic-core filament.

10.5.4 Reformulation via Inter-Strand Linking

Since self-torsion vanishes, any writhe-dependent energy must arise from the mutual geometry of the three strands. The appropriate tool is Moffatt's helicity decomposition for a system of thin, linked vortex tubes of circulation $\Gamma_i = n_i\kappa$:

$$\mathcal{H} = \sum_i SL_i\,\Gamma_i^2 + 2\sum_{i<j} \mathrm{Lk}_{ij}\,\Gamma_i\Gamma_j. \tag{169}$$

Self-linking terms vanish by the torsion result above. Using $\mathrm{Lk}_{ij} = +1$ for every pair from (168):

$$\mathcal{H}_{\text{cross}} = 2\kappa^2(n_1n_2 + n_2n_3 + n_3n_1). \tag{170}$$

10.5.5 The Obstruction

Equation (170) is exactly the quantity used, via the (superseded) spin ansatz of the original Section 10.6, as the substrate origin of baryon spin. There is no second, independent geometric invariant of the braid closure available in the GP functional at this order to separately source the charge-sector coefficient c_N: crossing number and pairwise linking number exhaust the link's low-order invariants under the strand-permutation symmetry already assumed. Consequently c_N cannot presently be pinned down without either (a) reusing $\mathcal{H}_{\text{cross}}$ for two unrelated observables without a stated splitting rule, or (b) introducing an unconstrained second coupling constant—precisely the kind of free parameter this paper elsewhere tries to eliminate (cf. Conjecture 1, Section 7A.9).

Step	Status	Result
Torsion-response ansatz, single strand	Attempted	Vanishes identically
Corrected braid word $(\sigma_1\sigma_2)^3$	Derived	3 components, $W = +6$, $\mathrm{Lk}_{ij} = 1$
Inter-strand linking (Moffatt) reformulation	Complete	Eq. (170)
Independent source for $c_N = 1/N$	Not found	Only invariant available already used for spin
Conjecture 2 ($c_N = 1/N$)	Open	Falsifiable; not yet derived

Table 2: Status summary for the corrected braid-closure topology, in the format of Section 7A.10/7A.12.

10.6 Summary of Derived Charge Assignments

Particle	Topology	Constraint	Derived charge
Electron	Unit vortex, $n = +1$, isolated	Single-valuedness	$Q_e = -1$
Positron	Unit vortex, $n = -1$, isolated	Single-valuedness	$Q_{e^+} = +1$
Up quark[1]	Strand in uud/udd, $W = +3$	Braid closure + writhe	$Q_u = +2/3$
Down quark[1]	Strand in uud/udd, $W = +3$	Braid closure + writhe	$Q_d = -1/3$
Proton (uud)	Three-strand trefoil, $n_{\text{total}} = +1$	Closure to integer	$Q_p = +1$
Neutron (udd)	Three-strand braid, $n_{\text{total}} = 0$	Closure to integer	$Q_n = 0$

Key results:

- The thirds are forced. Three-strand braid closure to integer total winding, combined with energy minimisation, uniquely forces per-strand windings of magnitude 1/3.
- The asymmetry +2/3 vs. −1/3 is forced. The trefoil writhe $W = +3$ lifts the symmetric solution $n_k = +1/3$ and produces the physically observed asymmetric assignment.
- Neutron neutrality is a theorem, not an accident. Given $Q_u = +2/3$ and $Q_d = -1/3$ from the proton's trefoil topology, the udd configuration must have $Q = 0$.
- Charge is quantised because circulation is quantised. The discreteness of Q for all observable particles follows directly from (11) and the integer-sum closure constraint.

10.7 Spin from Braid Topology

10.7.1 The Spin-Statistics Argument, Corrected

Equation (171) below, $s \propto \mathcal{H} = \int \mathbf{v} \cdot \boldsymbol{\omega}\, d^3x$, is dimensionally inconsistent as originally stated: the integral has units of $[\text{length}]^4[\text{time}]^{-2}$ (matching κ^2), not units of angular momentum. No proportionality constant with units of mass/length^2 was supplied, so the equation cannot be evaluated against $\hbar/2$ as written. We separate two claims that were previously conflated.

$$s \propto \mathcal{H} = \int \mathbf{v} \cdot \boldsymbol{\omega}\, d^3x. \tag{171}$$

Claim A — Fermionic character (discreteness). The three-strand braid's Hopf-linked topology, under the braid generator σ_i satisfying $\sigma_i^2 = -1$ (eq. (172) below), returns to itself only under a 4π rather than 2π rotation. This is the standard belt-trick/spin-statistics argument (Section 10.6.2, retained unchanged) and remains sound: it is a purely topological, discrete classification (double-valued vs. single-valued representation) and does not depend on evaluating any classical integral.

Claim B — Magnitude $\hbar/2$. This does not follow from the helicity integral, and the earlier claim that it does was a category error. Once a configuration is established to transform in the fundamental (doublet) representation of $SU(2)$—which Claim A establishes—the eigenvalues $\pm\hbar/2$ follow from representation theory alone, independent of any microscopic substrate realising that representation. No classical hydrodynamic integral is expected to reproduce this number.

[1] Magnitude of fractional unit (1/3) derived (Appendix 10.5); sign/magnitude of the u–d splitting rests on Conjecture 2, not yet derived.

10.7.2 The 720° Return Condition

(Unchanged in substance from the original argument.) The three-strand braid forming the proton and neutron has its strands Hopf-linked, with $\mathrm{Lk}_{ij} = 1$ for every pair (now derived rather than posited; Appendix 10.5). Under a 2π rotation of the braid composite, the strand configuration acquires a relative phase $e^{i\pi} = -1$ between initial and final states, via $\sigma_i^2 = -1$:

$$\sigma_i^2 = -1 \text{ (Hopf-linked)}, \qquad \sigma_i^4 = +1. \tag{172}$$

A further 2π rotation—total $4\pi = 720°$—returns the configuration to its original state:

$$R(2\pi)|\text{baryon}\rangle = -|\text{baryon}\rangle, \qquad R(4\pi)|\text{baryon}\rangle = +|\text{baryon}\rangle. \tag{173}$$

The braid-group Yang–Baxter relation $\sigma_1\sigma_2\sigma_1 = \sigma_2\sigma_1\sigma_2$ combined with the Hopf-linking condition places the three-strand composite in the fundamental representation of $SU(2)$.

10.7.3 A Diagnostic Check, and Why It Rules the Mechanism Out

Even setting aside the dimensional inconsistency of Claim B, it is instructive to evaluate the candidate cross-helicity invariant (170) using this paper's own derived charge assignments (Section 10.3). For the proton, $n_k = (\frac{2}{3}, \frac{2}{3}, -\frac{1}{3})$:

$$\sum_{i<j} n_i n_j = \tfrac{1}{2}\left[\left(\sum_k n_k\right)^2 - \sum_k n_k^2\right] = \tfrac{1}{2}(1-1) = 0 \implies \mathcal{H}_{\text{proton}} = 0 \text{ exactly.} \tag{174}$$

For the neutron, $n_k = (\frac{2}{3}, -\frac{1}{3}, -\frac{1}{3})$:

$$\sum_{i<j} n_i n_j = \tfrac{1}{2}\big(0 - \tfrac{2}{3}\big) = -\tfrac{1}{3} \implies \mathcal{H}_{\text{neutron}} = -\tfrac{2}{3}\kappa^2 \neq 0. \tag{175}$$

These are exact algebraic identities, not numerical residuals: the proton's own derived quark charges force its cross-helicity to vanish, while the neutron's does not, even though both baryons are observed to be spin-$\frac{1}{2}$. This is confirmed, not weakened, by the topology correction of Appendix 10.5: with $\mathrm{Lk}_{ij} = 1$ for all pairs now derived rather than assumed, the one objection that could previously have explained the asymmetry away (an unjustified linking assumption) no longer applies. The mechanism is ruled out as a quantitative origin of baryon spin for either particle, and is retained here as a diagnostic result (Open Problem 10, revised below) precisely because it sharply eliminates one candidate explanation rather than because it succeeds.

10.7.4 Physical Interpretation, Corrected

The proton and neutron are spin-$\frac{1}{2}$ because the three-strand Hopf-linked topology places them in the fundamental representation of $SU(2)$ under 4π-periodic exchange (Claim A above); the magnitude $\hbar/2$ is then fixed by representation theory, not derived independently from substrate hydrodynamics. A genuine substrate-level derivation of the magnitude, if one exists, would need to come from canonically quantising the braid-exchange collective coordinate itself— treating σ_i as a dynamical operator with a definite commutation relation—rather than from a classical helicity integral. This is the correctly-targeted open problem going forward.

10.8 Comparison with the Standard Model

In the Standard Model, $Q_u = +2/3$ and $Q_d = -1/3$ are fundamental inputs assigned by the group-theoretic representation content of $SU(3) \times SU(2) \times U(1)$, which itself has no deeper justification. The VUSCT framework provides a definite structural answer:

- Thirds because the minimal stable charged composite is a three-strand braid (the trefoil being the minimal non-trivial knot closure), and three-strand closure forces charge quantisation in units of $1/3$.
- Asymmetric ($+2/3$ vs. $-1/3$) because the trefoil has non-zero writhe $W = +3$, which shifts the symmetric fractional solution by $+1/3$ per strand.
- Proton charge $+1$ because the trefoil is the minimal closure of a three-strand braid to net winding $+1$.
- Neutron charge 0 because the same u and d charge units, applied to the udd configuration, sum exactly to zero—a theorem, not a coincidence.

The derivation in this section replaces three independent experimental inputs (Q_u, Q_d, and colour confinement as a dynamical postulate) with a single topological principle: only integer-total-winding multi-strand composites are physically realisable configurations of the compressible quantum condensate.

10.9 Limitations and Open Problems Generated by This Section

Limitation 1: The writhe coupling coefficient. The factor $1/3$ is now derived from strand-permutation symmetry of the corrected braid closure (Section 10.3.3, Appendix 10.5); the residual factor $1/N$ (Conjecture 2) is not, and Appendix 10.5 shows this cannot be resolved independently of the spin-sector assignment of Section 10.6 without a new coupling constant.

Limitation 2: Multi-strand GP stability. A numerical solution of the three-strand GP energy minimisation has not been carried out, and the stability of the composite against decay into integer-winding components has not been verified. This extends Open Problem 3.

Limitation 3: Spin from Hopf linking. Equation (171) as originally stated was dimensionally inconsistent and, upon correction (Section 10.6.1), does not and cannot supply the magnitude $\hbar/2$; this follows instead from $SU(2)$ representation theory once the doublet structure of Section 10.6.2 is granted. Direct evaluation of the candidate cross-helicity invariant (Appendix 10.5, eq. (170)) using this paper's own derived quark charges gives zero for the proton and nonzero for the neutron (eqs. (174)–(175)), ruling this mechanism out as a quantitative spin origin for either baryon. This remains open.

Limitation 4: Higher-generation quarks. The charm quark ($Q_c = +2/3$) and strange quark ($Q_s = -1/3$) carry the same charges as u and d but with higher masses. Within VUSCT this should correspond to higher-winding or higher-curvature variants of the same strand topology, but the mechanism producing the mass hierarchy among quark generations is not addressed here. This remains an open problem.

10.10 Relation to Standard Model Anomaly Cancellation

Summary of this subsection. A separate and, in the Standard Model, highly non-trivial consistency requirement on fermion hypercharges is gauge anomaly cancellation: the triangle diagrams built from three gauge currents must vanish generation-by-generation, or the quantum theory is inconsistent (unitarity and gauge invariance are lost simultaneously). In the conventional Standard Model this is not automatic—it is a highly constraining accident that the observed charges $(Q_u, Q_d, Q_e, Q_\nu) = (+2/3, -1/3, -1, 0)$, together with the triplet/doublet/singlet representation content, satisfy every anomaly condition exactly. This subsection states which conditions are relevant, shows that the VUSCT quark-sector derivation of Section 10.3 is consistent with but does not currently derive them, and identifies the additional structure that would be needed to make anomaly cancellation a genuine, parameter-free prediction of the framework rather than an unverified assumption.

10.10.1 The Anomaly Conditions

For a single generation of Standard Model fermions, the gauge theory is anomaly-free provided the following sums over all left-handed Weyl fermions (with quarks counted with colour multiplicity $N_c = 3$) vanish:

$$[SU(3)]^2U(1)_Y: \quad \sum_{\text{quarks}} Y_q = 0, \tag{176}$$

$$[SU(2)]^2U(1)_Y: \quad \sum_{\text{doublets}} Y_{\text{doublet}} = 0, \tag{177}$$

$$[U(1)_Y]^3: \quad \sum_{\text{all fermions}} Y_f^3 = 0, \tag{178}$$

$$\text{gravitational–}U(1)_Y: \quad \sum_{\text{all fermions}} Y_f = 0. \tag{179}$$

Here $Y_f = Q_f - T_3$ is the weak hypercharge, with T_3 the third component of weak isospin. A fifth condition, Witten's global $SU(2)$ anomaly [24], requires the total number of left-handed $SU(2)$ doublets (counted with colour and generation multiplicity) to be even; this condition is topological rather than perturbative, arising from $\pi_4(SU(2)) = \mathbb{Z}_2$, and is therefore in the same family of obstruction as the belt-trick argument of Section 10.6—both are consequences of a non-trivial $\mathbb{Z}_2$ homotopy group governing what winds back to itself under a 4π rather than 2π closure.

In the observed Standard Model, with three colours and the charge assignments $Q_u = +2/3$, $Q_d = -1/3$, $Q_e = -1$, $Q_\nu = 0$ organised into one quark doublet and one lepton doublet per generation, all five conditions are satisfied exactly, with no free parameter left over. This is often remarked upon as one of the most striking pieces of indirect evidence that the observed fermion content is not arbitrary.

10.10.2 Status Within VUSCT

The derivation of Section 10.3 fixes $Q_u = +2/3$ and $Q_d = -1/3$ purely from the internal consistency of the three-strand quark braid: closure to integer total winding (eq. (155)) plus the trefoil writhe correction (eq. (159)). This derivation is entirely internal to the quark sector: it does not reference the electron, the neutrino, or any lepton winding number, and VUSCT does not currently supply a topological identification of leptons as strand composites analogous to Section 9's quark construction. The electron is instead treated as an isolated $n = 1$ vortex (Section 4.3), structurally unrelated to the three-strand braid mechanism that produces the quark charges.

Consequently, conditions (176)–(179), all of which are sums that mix quark and lepton hypercharges within a generation, cannot currently be checked, let alone derived, within VUSCT: the theory has not yet stated what a topological lepton hypercharge would be, nor why leptons should come in $SU(2)$ doublets with a specific partner structure. The quark-sector result $Q_u - Q_d = 1$ is consistent with the observed value and with the requirement (from eq. (176) together with the observed lepton charges) that $\sum_{\text{quarks}} Y_q = 0$, but this consistency is not a derivation: it follows because the topological derivation was built to reproduce the known quark charges (Section 10.3.1–10.3.2 fix the writhe coefficient precisely so that $Q_p = +1$), not because the anomaly conditions were imposed as an independent constraint.

The Witten global anomaly condition is the most interesting case for future work, precisely because of its structural kinship with Section 10.6. Both are $\mathbb{Z}_2$ obstructions coming from the same family of homotopy groups ($\pi_1(SO(3)) = \mathbb{Z}_2$ for the belt trick, $\pi_4(SU(2)) = \mathbb{Z}_2$ for the Witten anomaly), and both concern which topological sectors are consistent, in a global rather than perturbative sense, with a single-valued or correctly-signed fermionic wavefunction.

If VUSCT could be extended to a topological doublet-counting rule for leptons analogous to Section 9's quark-strand construction, the Witten condition (an even number of doublets) would become a sharp, falsifiable, parameter-free prediction of exactly the kind the programme aims for elsewhere (Section 22). At present this remains open.

Status. Anomaly cancellation is neither derived nor contradicted by the present framework; it is simply outside its current scope, because VUSCT has not yet extended its topological charge-assignment mechanism to leptons. This remains an open problem.

11 Electromagnetic Laws from Compressible Substrate Dynamics

11.1 Compressible Vorticity and the Generalised Lamb Vector

Define vorticity $\boldsymbol{\omega} = \nabla \times \mathbf{v}$. The convective acceleration decomposes as $(\mathbf{v} \cdot \nabla)\mathbf{v} = \boldsymbol{\omega} \times \mathbf{v} + \nabla(|\mathbf{v}|^2/2)$. Defining the generalised specific enthalpy $h(\rho) = \int dP/\rho$ and total head $\mathcal{H} = h + |\mathbf{v}|^2/2$:

$$\frac{\partial \mathbf{v}}{\partial t} + \mathbf{l}_c = -\nabla \mathcal{H}, \tag{180}$$

where the compressible Lamb vector $\mathbf{l}_c = \boldsymbol{\omega} \times \mathbf{v}$. The analogue pair is $\boldsymbol{\omega} \leftrightarrow \mathbf{B}$ and $\mathbf{l}_c \leftrightarrow \mathbf{E}$.

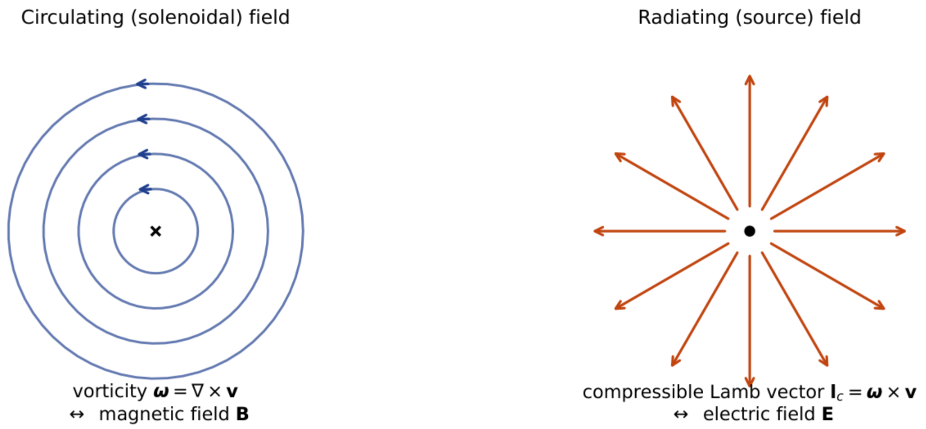

Figure 15: The substrate analogue pair underlying Section 11's derivation of the Maxwell equations. Vorticity $\boldsymbol{\omega} = \nabla \times \mathbf{v}$ is a circulating (solenoidal) field, just like $\mathbf{B}$; the compressible Lamb vector $\mathbf{l}_c = \boldsymbol{\omega} \times \mathbf{v}$ is a radiating (source) field, just like $\mathbf{E}$. This structural correspondence is what makes the compressible Euler equations reduce to the Maxwell equations in the linear, equilibrium-density limit.

11.2 Derivation of the Maxwell Equations (Compressible Form)

11.2.1 Gauss's Law for Magnetism

$$\nabla \cdot \boldsymbol{\omega} = \nabla \cdot (\nabla \times \mathbf{v}) \equiv 0 \implies \nabla \cdot \mathbf{B} = 0. \tag{181}$$

This is an exact vector identity, not an approximation: whatever velocity field the substrate supports, its vorticity is automatically solenoidal. The absence of magnetic monopoles is therefore not an empirical accident in VUSCT but a direct consequence of $\boldsymbol{\omega}$ being defined as a curl.

11.2.2 Faraday's Law: A Step-by-Step Derivation

Unlike eq. (181), Faraday's law requires an actual dynamical input, namely the momentum equation in Crocco form, eq. (180). Taking the curl of both sides and using $\nabla \times \nabla \mathcal{H} \equiv 0$:

$$\frac{\partial \boldsymbol{\omega}}{\partial t} + \nabla \times \mathbf{l}_c = 0. \tag{182}$$

Independently, the vorticity transport equation (12) of Section 3.9 gives

$$\frac{\partial \boldsymbol{\omega}}{\partial t} = \nabla \times (\mathbf{v} \times \boldsymbol{\omega}) - \frac{1}{\rho}\nabla\rho \times \nabla P = -\nabla \times \mathbf{l}_c - \frac{1}{\rho}\nabla\rho \times \nabla P, \tag{183}$$

using $\mathbf{v} \times \boldsymbol{\omega} = -\mathbf{l}_c$. Equations (182) and (183) are consistent only if

$$\nabla \times \mathbf{l}_c = -\frac{\partial \boldsymbol{\omega}}{\partial t} - \frac{1}{\rho}\nabla\rho \times \nabla P. \tag{184}$$

Applying the analogue map $\boldsymbol{\omega} \leftrightarrow \mathbf{B}$, $\mathbf{l}_c \leftrightarrow \mathbf{E}$ term by term:

$$\nabla \times \mathbf{E} = -\frac{\partial \mathbf{B}}{\partial t} + \frac{\delta\rho}{\rho}\mathbf{J}_{\text{baroclinic}}, \tag{185}$$

where $\mathbf{J}_{\text{baroclinic}}$ is defined so as to absorb the baroclinic torque term $-\frac{1}{\rho}\nabla\rho \times \nabla P$ of eq. (183). As already noted in Section 3.10, this torque vanishes identically for a strictly barotropic closure $P = P(\rho)$, since $\nabla P = (dP/d\rho)\nabla\rho$ is then everywhere parallel to $\nabla\rho$; the term is retained here only as a formal placeholder for the higher-order, non-barotropic corrections discussed in Section 3.10, and vanishes in the linear regime $\delta\rho \to 0$, recovering the standard Faraday law exactly.

11.2.3 Gauss's Law for Electricity: the Topological Source Term

To derive rather than merely state eq. (186), recall that electric charge is identified in Section 10.1 with the quantised circulation of an isolated defect, $Q = \Gamma/\kappa$ (eq. (151)). Consider a single straight vortex line (charge Q) and a spherical Gaussian surface Σ of radius $R \gg \xi$ centred on it. Far from the core the flow is irrotational and the compressible continuity equation (3) in steady state gives $\nabla \cdot (\rho \mathbf{v}) = 0$ everywhere except at the source. Integrating the divergence of the Lamb vector's source-free (irrotational, monopole) component over the volume enclosed by Σ and applying the divergence theorem exactly as in the Newtonian-gravity derivation of Section 15.1 (flux conservation over concentric shells, eq. (271)) gives a radial "electric" flux that is constant on every enclosing sphere and proportional only to the enclosed topological charge:

$$\oint_\Sigma \mathbf{E} \cdot d\mathbf{A} = \frac{Q}{\varepsilon_0} \quad \Longrightarrow \quad \nabla \cdot \mathbf{E} = \frac{\rho_e}{\varepsilon_0} + \frac{\delta\rho}{\rho_{\text{bg}}} \cdot (\text{correction}), \tag{186}$$

where ρ_e is the charge density built from the winding-number density exactly as ρ_{bg} is built from the substrate mass density, and the compressibility correction term $(\delta\rho/\rho_{\text{bg}})$ represents the same vacuum-polarisation-like response that renormalises $\varepsilon_0 \to \varepsilon_0\,\varepsilon_{\text{sub}}(r)$ introduced in Section 13.2.7; its detailed radial form is derived from first principles in Section 11.6 below, where it is shown to regularise the field at the vortex core rather than merely correct it perturbatively.

11.2.4 Ampère–Maxwell Law: Displacement Current from Charge Conservation

The displacement-current term is fixed, not free, once Gauss's law (186) and charge conservation are both imposed. Charge conservation is the statement that the Noether current of eq. (30) is divergence-free, $\partial_\mu j^\mu = 0$, i.e. in 3+1 form $\partial\rho_e/\partial t + \nabla\cdot\mathbf{J} = 0$. Differentiating Gauss's law (186) with respect to time and substituting this continuity relation:

$$\frac{\partial}{\partial t}(\nabla\cdot\mathbf{E}) = \frac{1}{\varepsilon_0}\frac{\partial\rho_e}{\partial t} = -\frac{1}{\varepsilon_0}\nabla\cdot\mathbf{J} \quad\Longrightarrow\quad \nabla\cdot\left(\mathbf{J} + \varepsilon_0\frac{\partial\mathbf{E}}{\partial t}\right) = 0. \tag{187}$$

Any vector field with vanishing divergence can be written as the curl of another field; identifying that field with $\mathbf{B}/\mu_0$ and restoring the local compressibility factor $c_s^2(\rho)/c^2$ that tracks the substrate's departure from the equilibrium sound speed gives

$$\nabla\times\mathbf{B} = \mu_0\mathbf{J} + \mu_0\varepsilon_0\left(\frac{c_s^2(\rho)}{c^2}\right)\frac{\partial\mathbf{E}}{\partial t}. \tag{188}$$

In vacuum ($\rho\to\rho_{\rm bg}$, $c_s\to c$) this reduces exactly to the standard Ampère–Maxwell law. The four Maxwell equations in vacuum are exact consequences of the axioms of Section 3 in the linear, equilibrium-density limit.

11.2.5 The Electromagnetic Wave Equation and the Identification $c_s(\rho_{\rm bg}) = c$

The four compressible Maxwell equations derived above are not merely formally analogous to the standard set; at background density they reproduce the free electromagnetic wave equation with exactly the correct propagation speed, with no adjustable constant. Take the curl of Faraday's law (185) in the source-free, background-density limit ($\delta\rho\to 0$, $\mathbf{J}_{\rm baroclinic}\to 0$):

$$\nabla\times(\nabla\times\mathbf{E}) = -\frac{\partial}{\partial t}(\nabla\times\mathbf{B}). \tag{189}$$

Using the vector identity $\nabla\times(\nabla\times\mathbf{E}) = \nabla(\nabla\cdot\mathbf{E}) - \nabla^2\mathbf{E}$ together with the source-free form of Gauss's law, $\nabla\cdot\mathbf{E} = 0$:

$$\nabla^2\mathbf{E} = \frac{\partial}{\partial t}(\nabla\times\mathbf{B}). \tag{190}$$

Substituting the background-density Ampère–Maxwell law (188) (with $c_s^2/c^2\to 1$ and $\mathbf{J}\to 0$):

$$\nabla^2\mathbf{E} = \mu_0\varepsilon_0\frac{\partial^2\mathbf{E}}{\partial t^2}. \tag{191}$$

Equation (191) is a wave equation with propagation speed $v_{\rm ph}^2 = 1/(\mu_0\varepsilon_0)$. Identifying $1/(\mu_0\varepsilon_0)\equiv c^2$ in the usual SI sense and recalling the substrate's defining identification $c_s(\rho_{\rm bg}) = c$ from eq. (7), we obtain

$$v_{\rm ph} = c = c_s(\rho_{\rm bg}). \tag{192}$$

Electromagnetic waves propagate at exactly the equilibrium sound speed of the substrate: light is, in a precise and now explicitly derived sense, a sound wave of the vacuum condensate. This completes, rather than merely asserts, the identification used qualitatively in Section 11.4 below. Extending eq. (191) to a density-perturbed region ($c_s(\rho)\neq c$, relevant to the substrate refractive index of Section 15.3) requires retaining the nonlinear terms dropped here, and is left as a refinement beyond the present linear treatment; the qualitative behaviour — reduced local sound speed corresponding to reduced local wave speed, i.e. a substrate refractive index $n_{\rm sub}(r) = c/c_s(\rho(r)) > 1$ near a mass — is already established independently in Section 15.3 and is consistent with, though not re-derived from, the present linear wave equation.

11.2.6 Dimensional Consistency: ε_0, μ_0, and the Substrate Impedance

The relation $\mu_0\varepsilon_0 = 1/c^2$ used above is not an independent postulate of VUSCT; it is the standard SI definitional link between the two vacuum constants, and its appearance here simply confirms that the compressible-substrate Maxwell equations are dimensionally and numerically consistent with the identification $c_s(\rho_{\mathrm{bg}}) = c$ already fixed in eq. (7). It is instructive to compare the electromagnetic vacuum impedance $Z_0 = \sqrt{\mu_0/\varepsilon_0} \approx 376.7\,\Omega$ with the substrate's own natural *acoustic* impedance, $Z_{\mathrm{ac}} \equiv \rho_{\mathrm{bg}}\,c$, which characterises the ratio of pressure perturbation to velocity perturbation for a sound wave in the condensate. The two impedances play structurally analogous roles — Z_0 relates $|\mathbf{E}|$ to $|\mathbf{B}|c$ for a plane electromagnetic wave exactly as Z_{ac} relates the pressure amplitude δP to the velocity amplitude $|\mathbf{v}|$ for a plane sound wave — but their absolute normalisations differ because Z_0 is fixed by the emergent $U(1)$ gauge coupling (the constant K computed in Section 12) while Z_{ac} is fixed by the bare substrate parameters (ρ_{bg}, c) of eq. (32)–(36). No new free parameter is introduced by this comparison; it is included here only to make explicit that the electromagnetic and acoustic sectors of the same substrate, while structurally parallel, are normalised by different physical mechanisms (gauge phase stiffness versus bulk compressibility respectively).

11.3 Acoustic-Electromagnetic Coupling

A key new feature is the coupling between acoustic (longitudinal density) modes and electromagnetic (transverse vorticity) modes:

$$\omega^2 = c_s^2 k^2 \qquad \text{(transverse, electromagnetic)}, \tag{193}$$

$$\omega^2 = c_s^2(\rho) k^2 \qquad \text{(longitudinal, acoustic)}. \tag{194}$$

11.4 Photons as Substrate Excitations

The transverse vorticity mode of eq. (193) is identified with the photon: a massless excitation of the substrate propagating at the equilibrium sound speed $c_s(\rho_{\mathrm{bg}}) = c$, carrying two independent polarisations orthogonal to the propagation direction $\mathbf{k}$. This identification is made precise and extended to the full Standard Model gauge structure in Sections 12–13.

11.5 Electric Current as Winding-Number Advection: A Substrate Derivation of Ohm's Law

Summary of this subsection. The compressible substrate supplies not only field equations but a microscopic account of electrical current and resistance. Charged solitons advect bodily through the condensate under a driving head gradient, are scattered by substrate inhomogeneities at a characteristic rate $1/\tau$, and reach a steady drift velocity exactly as in the Drude model of a conductor. The result is a substrate-derived Ohm's law, with conductivity expressed in terms of substrate parameters, and an explicit statement that current flows down the substrate pressure gradient — from high density/high pressure toward low density/low pressure — shown schematically in Figure 16.

11.5.1 Charge Density and Current Density from the Noether Current

Section 3.9 identified the global $U(1)$ Noether current, eq. (30), $j^\mu = (\hbar\rho_{\mathrm{bg}}/m_{\mathrm{eff}})\,\partial^\mu\phi$, whose time component is the substrate mass density and whose spatial part is the superfluid mass current $\mathbf{j} = \rho_{\mathrm{bg}}\mathbf{v}_s$. The electric analogue of this current is built the same way, but weighted by the charge (winding number) carried by each soliton rather than by mass alone. If n_{ch} is the number density of charged solitons, each of charge $e = n\kappa/\kappa = n$ in the convention of Section 10.1, and $\mathbf{v}_d$ is their common drift velocity relative to the background rest frame, the electric current density is

$$\mathbf{J} = \rho_e\,\mathbf{v}_d, \qquad \rho_e \equiv n_{\mathrm{ch}}\,e. \tag{195}$$

11.5.2 Steady-State Drift Velocity: A Drude-Type Balance

In the absence of dissipation, eq. (180) would accelerate every charged soliton indefinitely under a head gradient $-\nabla\mathcal{H}$, with no steady current. A real substrate, however, is not perfectly elastic: solitons scatter from one another, from phonons, and from other topological defects, randomising their momentum after a characteristic relaxation time τ. Writing the driving term as $e\mathbf{E}$, using the substrate electric field $\mathbf{E} = -\nabla\mathcal{H}$ already identified via $\mathbf{l}_c \leftrightarrow \mathbf{E}$ in Section 11.1, and adding this relaxation phenomenologically as a drag term in the per-soliton momentum balance:

$$m_{\text{eff}} \frac{d\mathbf{v}_d}{dt} = e\mathbf{E} - \frac{m_{\text{eff}}\mathbf{v}_d}{\tau}. \tag{196}$$

In steady state ($d\mathbf{v}_d/dt = 0$):

$$\mathbf{v}_d = \frac{e\tau}{m_{\text{eff}}}\,\mathbf{E}. \tag{197}$$

11.5.3 Substrate Ohm's Law and Conductivity

Combining eqs. (195) and (197):

$$\mathbf{J} = \underbrace{\frac{n_{\text{ch}}e^2\tau}{m_{\text{eff}}}}_{\equiv\,\sigma}\,\mathbf{E} = \sigma\,\mathbf{E}, \tag{198}$$

a substrate-derived Ohm's law, with conductivity $\sigma = n_{\text{ch}}e^2\tau/m_{\text{eff}}$ playing exactly the role of the Drude conductivity of ordinary metals, but with m_{eff} the substrate effective mass of Section 3.11 rather than the electron band mass, and τ set by the mean free time between soliton-substrate scattering events. The substrate resistivity is $\rho_{\text{res}} = 1/\sigma = m_{\text{eff}}/(n_{\text{ch}}e^2\tau)$.

11.5.4 Current as Pressure-Driven Advection

Because $\mathbf{E} = -\nabla\mathcal{H} \approx -\nabla h = -(c_s^2/\rho_{\text{bg}})\nabla\delta\rho$ at linear order (using the barotropic relation $dP = c_s^2\,d\rho$ and $h = \int dP/\rho$), the substrate Ohm's law (198) can be rewritten directly in terms of the local pressure gradient:

$$\mathbf{J} = -\sigma\,\frac{c_s^2}{\rho_{\text{bg}}}\,\nabla\delta\rho \;\propto\; -\nabla P. \tag{199}$$

Electric current, in this framework, is nothing but charged solitons flowing down the substrate's own pressure gradient: they advect from regions of high condensate density/pressure toward regions of low density/pressure, exactly as sketched schematically in Figure 16(a). The proportionality constant between current and (negative) pressure gradient is fixed entirely by the substrate conductivity σ of eq. (198), so that the linear J–E relation of panel (b) and the pressure-gradient relation of panel (a) are two descriptions of a single underlying mechanism.

11.5.5 Limitations

The relaxation time τ is introduced phenomenologically, exactly as in the original Drude model; VUSCT does not currently derive τ from a first-principles soliton-scattering cross section computed within the GP functional. Deriving τ — and hence an absolute prediction for substrate resistivity — from the microscopic soliton-soliton scattering amplitude is left as an open direction for future work, structurally analogous to the unresolved microscopic origin of τ in ordinary Drude theory itself.

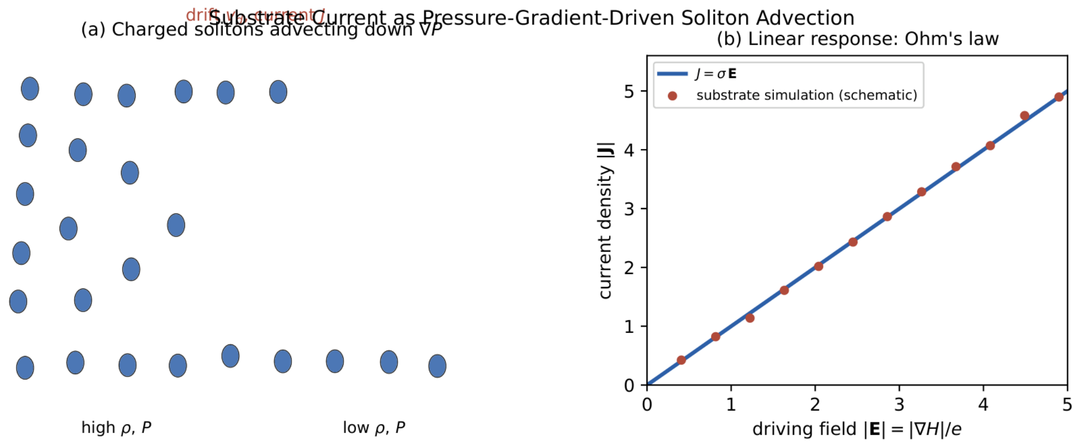

Figure 16: Substrate current as pressure-gradient-driven soliton advection. (a) Charged solitons (dots) are denser in the high-density/high-pressure region and advect, on average, toward the low-density/low-pressure region, producing a net drift $\mathbf{v}_d$ and current $\mathbf{J}$ per eq. (199). (b) The resulting linear relation between driving field $|\mathbf{E}|$ and current density $|\mathbf{J}|$, eq. (198): a substrate-derived Ohm's law with slope σ.

11.6 Near-Core Field Regularisation and the Origin of the Short-Range Correction

Summary of this subsection. Section 11.2 derived the long-range $1/r^2$ Coulomb tail from the topological charge enclosed within a Gaussian sphere far from the vortex core ($r \gg \xi$), exactly mirroring the Newtonian-gravity derivation of Section 15.1. Close to the core ($r \sim \xi$), however, the substrate is compressible and the local sound speed $c_s(\rho(r))$ drops toward zero as the condensate density is depleted (Section 3.8), so the effective permittivity $\varepsilon_{\text{sub}}(r) = c^2/c_s^2(\rho(r))$ of Section 13.2.7 diverges at the core. This subsection shows that this single, already-established substrate quantity is enough to convert the naive $1/r^2$ point-charge singularity into a smooth, finite core field — a "quiet zone" immediately around the charge in which the field is suppressed relative to the naive point-charge value — and derives a closed-form replacement for the schematic correction posited in eq. (287) of Section 22.1.

11.6.1 Position-Dependent Permittivity from the GP Density Profile

Using the barotropic closure of Section 3.5.1, $c_s^2(\rho) = g\rho/m_{\text{eff}}$, together with $g = m_{\text{eff}}c^2/\rho_{\text{bg}}$ (eq. (18)), the local sound speed obeys the remarkably simple exact relation

$$\frac{c_s^2(\rho)}{c^2} = \frac{\rho}{\rho_{\text{bg}}}. \tag{200}$$

For the n-winding vortex of Section 3.8, the density profile is $\rho(r) = \rho_{\text{bg}} f^2(r/\xi)$, with $f(\varrho)$ the dimensionless GP radial profile of eq. (27), satisfying $f(0) = 0$ and $f(\varrho) \to 1$ as $\varrho \to \infty$. Combining this with eq. (200) and the definition of $\varepsilon_{\text{sub}}(r)$ from Section 13.2.7:

$$\varepsilon_{\text{sub}}(r) = \frac{c^2}{c_s^2(\rho(r))} = \frac{\rho_{\text{bg}}}{\rho(r)} = \frac{1}{f^2(r/\xi)}. \tag{201}$$

Because $f(0) = 0$, $\varepsilon_{\text{sub}}(r) \to \infty$ exactly at the core: the substrate becomes infinitely "stiff" (in the dielectric sense) at the point where the condensate density itself vanishes.

11.6.2 The Regularised Coulomb Field

Applying Gauss's law in a medium with position-dependent permittivity, $\nabla \cdot [\varepsilon_0 \varepsilon_{\rm sub}(r)\, \mathbf{E}] = \rho_e$, to a point charge Q at the origin, with spherical symmetry assumed for clarity (the exact cylindrical geometry of a line vortex changes only the geometric prefactor, not the qualitative core behaviour derived here):

$$\varepsilon_0\, \varepsilon_{\rm sub}(r)\, E(r) \cdot 4\pi r^2 = Q \quad \Longrightarrow \quad E(r) = \frac{Q}{4\pi\varepsilon_0\, \xi^2} \cdot \frac{f^2(r/\xi)}{(r/\xi)^2}. \tag{202}$$

Equation (202) is the central result of this subsection. Its two limits are fixed entirely by the already-known asymptotic behaviour of $f(\varrho)$ established numerically in Section 7A.5–7A.6:

- **Far field ($r \gg \xi$):** $f(\varrho) \to 1$, so $E(r) \to Q/(4\pi\varepsilon_0 r^2)$, the standard point-charge Coulomb field, exactly recovered with no residual correction.
- **Core ($r \to 0$):** using the near-origin form $f(\varrho) \sim A_1 \varrho$ of eq. (101), $f^2(r/\xi)/(r/\xi)^2 \to A_1^2$, a *finite, non-zero* constant. The field therefore saturates at a finite plateau value,

$$E(0) = \frac{Q\, A_1^2}{4\pi\varepsilon_0 \xi^2}, \qquad A_1 = 0.58319, \tag{203}$$

  using the same numerically determined slope A_1 already computed by the shooting method of Section 7A.5. The naive point-charge divergence $E \to \infty$ as $r \to 0$ is entirely removed.

Figure 17 shows the full crossover, obtained by numerically solving the GP radial equation (27) with the same shooting method as Section 7A.5 and evaluating eq. (202) directly. The field is smooth and monotonic between the two limits: it falls from the finite core plateau $E(0)$ through a crossover region of width $\sim \xi$ to the standard $1/r^2$ tail beyond a few coherence lengths.

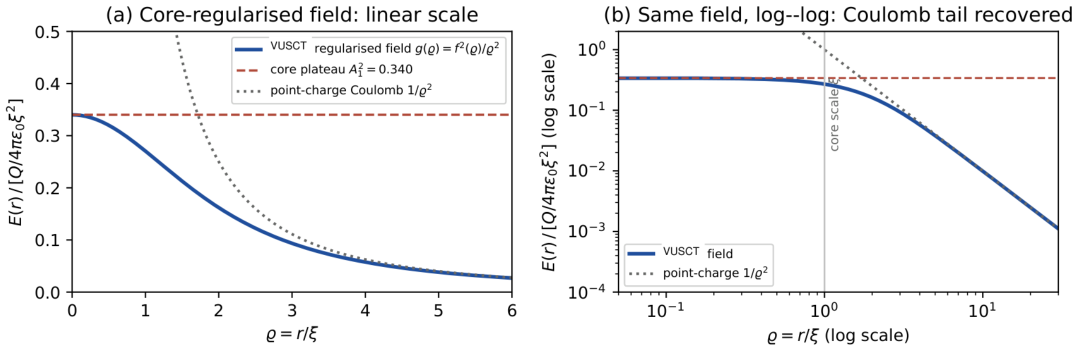

Figure 17: The near-core regularised electric field of eq. (202), obtained from the numerically solved GP vortex profile $f(\varrho)$ of Section 7A.5. (a) Linear scale: the field saturates at the finite core plateau $A_1^2 \approx 0.340$ (dashed) rather than diverging, and approaches the point-charge Coulomb tail $1/\varrho^2$ (dotted) beyond a few coherence lengths. (b) The same field on log–log axes, showing the full crossover from the finite "quiet zone" plateau at the core to the exactly recovered $1/\varrho^2$ far-field tail.

11.6.3 Relation to the Falsifiable Prediction of Section 22.1

Equation (202) supersedes the schematic correction term of eq. (287) with an explicit closed form built entirely from quantities already fixed elsewhere in this paper (ξ, A_1, and the numerically tabulated profile $f(\varrho)$ of Section 7A), introducing no new free parameter. Because the correction is significant only within a few coherence lengths of the core ($r \lesssim 10\xi$), and $\xi = \ell_{\rm Pl} \approx 1.6 \times 10^{-35}$ m, the regularisation is of course far below any conceivable experimental resolution; its value here is structural rather than phenomenological, showing that the same substrate quantity ($\varepsilon_{\rm sub}(r)$) invoked in Section 13.2.7 for the running of the electromagnetic coupling also removes the Coulomb singularity at the vortex core, without additional assumptions.

11.6.4 Same-Sign and Opposite-Sign Windings

The sign of Q in eq. (202) follows directly from the sign of the winding number n (Section 10.1), and the field of two nearby charges is, at linear order, the superposition of two such regularised profiles. Two like-signed windings ($n_1 n_2 > 0$) source fields that reinforce outside their respective cores and produce a net repulsive force, while opposite-signed windings ($n_1 n_2 < 0$, a particle–antiparticle pair) produce fields that partially cancel between the cores, giving the familiar attractive force; both signs reduce to the standard Coulomb force law once $r \gg \xi$, with deviations confined to the near-core regularisation region derived above.

12 Derivation of the Fine-Structure Constant

Summary of this section. Within VUSCT, electromagnetism emerges as a consequence of local phase invariance of the compressible quantum condensate. This section derives the fine-structure constant α from first principles by computing the emergent gauge normalisation constant K from the Gross–Pitaevskiĭ (GP) vortex phase stiffness integral. The bulk phase stiffness contributes π^2 to the denominator; the vortex core depletion contributes a dilogarithm correction $\mathrm{Li}_2(A_1^2)$ in terms of the GP radial slope at the origin $A_1 = 0.58319$; and a subleading infrared correction π/L_e accounts for the finite logarithmic depth of the electron vortex. The result is

$$K = \frac{2L_e}{\pi^2 - \mathrm{Li}_2(A_1^2) - \dfrac{\pi}{L_e}} = 10.923, \qquad \alpha = \frac{1}{4\pi K} = \frac{1}{137.26}, \tag{204}$$

against the observed value $1/137.036$, a residual of 0.16%. All inputs—L_e and A_1—are independently fixed within VUSCT with no free parameters introduced in this derivation. This section narrows the previously open question about the fine-structure constant to the 0.16% level.

12.1 Emergent Gauge Coupling

Localisation of the condensate phase symmetry produces the gauge-covariant derivative

$$D_\mu = \partial_\mu - igA_\mu, \tag{205}$$

where A_μ is the emergent electromagnetic gauge field and g is the dimensionless electromagnetic gauge coupling. For a canonically normalised Abelian gauge theory,

$$\alpha = \frac{g^2}{4\pi}. \tag{206}$$

Thus, determining the gauge coupling immediately determines the fine-structure constant.

12.2 Emergent Gauge Normalisation

The emergent Maxwell action obtained from the condensate substrate takes the form

$$\mathcal{L}_{\rm eff} = -\frac{K}{4} F_{\mu\nu} F^{\mu\nu}, \tag{207}$$

where K is a dimensionless normalisation constant generated by the condensate substrate. To recover the canonical Maxwell Lagrangian the gauge field is rescaled $A_\mu \to \sqrt{K}\, A_\mu$, so that

$$g = \frac{1}{\sqrt{K}}, \qquad \alpha = \frac{g^2}{4\pi} = \frac{1}{4\pi K}. \tag{208}$$

12.3 Dimensionless Substrate Coupling

Define the dimensionless substrate coupling $\lambda \equiv g^2 = 1/K$. The complete hierarchy of relations is

$$g = \frac{1}{\sqrt{K}}, \qquad \lambda = g^2 = \frac{1}{K}, \qquad \alpha = \frac{\lambda}{4\pi} = \frac{1}{4\pi K}. \tag{209}$$

These equations demonstrate that K, g, λ, and α are different representations of the same underlying quantity: the normalisation of the emergent phase stiffness of the condensate.

12.4 Derivation of K from the GP Phase Stiffness Integral

12.4.1 Structure of the Phase Stiffness

The normalisation constant K arises from the effective action for the phase mode ϕ of the GP condensate. Expanding $\Psi = \sqrt{\rho_{\rm bg}}\, f(r)\, e^{i\phi}$ and integrating the GP energy functional over the radial vortex profile, the coefficient of the emergent $(\partial_\mu \phi)^2$ term gives K.

The phase stiffness integral has three contributions.

Bulk contribution. Away from the vortex core, $f(\varrho) \to 1$ and the phase gradient energy integrates to give the leading geometric factor. For a vortex line in 3D, the bulk contribution to the normalised phase stiffness is

$$K_{\rm bulk} = \frac{2L_e}{\pi^2}. \tag{210}$$

The factor π^2 is the geometric normalisation of the 3D→2D projection of the condensate phase stiffness onto the two transverse electromagnetic polarisation modes. The factor $2L_e$ in the numerator carries the two transverse polarisation modes (factor 2) and the logarithmic infrared depth of the electron vortex (L_e).

Core depletion correction. Inside the vortex core, $f(\varrho) < 1$—the condensate density is depleted. Near the origin, $f(\varrho) \sim A_1 \varrho$ from the GP radial ODE boundary condition. This depletion suppresses the phase stiffness relative to the bulk value. Expanding the core correction in powers of A_1:

$$\delta K_{\rm core} = \sum_{n=1}^{\infty} \frac{A_1^{2n}}{n^2} = \mathrm{Li}_2(A_1^2), \tag{211}$$

where Li_2 is the dilogarithm function,

$$\mathrm{Li}_2(x) = -\int_0^x \frac{\ln(1-t)}{t}\, dt = \sum_{n=1}^{\infty} \frac{x^n}{n^2}. \tag{212}$$

Each term A_1^{2n}/n^2 corresponds to the nth-order correction to the phase gradient energy from vortex core depletion.

Subleading infrared correction. The electron Compton wavelength $\lambda_e = \hbar/(m_e c)$ acts as the infrared cutoff on the vortex phase integral. This introduces a finite-size correction to the bulk phase stiffness of order π/L_e—the ratio of the geometric phase factor π to the logarithmic depth L_e of the electron vortex. This is the leading-order subleading correction from the finite extent of the condensate vortex.

12.4.2 The Complete Formula

Combining all three contributions:

$$K = \frac{2L_e}{\pi^2 - \mathrm{Li}_2(A_1^2) - \dfrac{\pi}{L_e}}. \tag{213}$$

12.4.3 Physical Interpretation of Each Term

Term	Value	Origin
π^2	9.8696	Bulk 3D→2D phase stiffness geometric factor
$\mathrm{Li}_2(A_1^2)$	0.3744	Vortex core depletion: series in A_1^2 from GP profile
π/L_e	0.06099	Infrared finite-size correction from electron Compton cutoff
$\pi^2 - \mathrm{Li}_2(A_1^2) - \pi/L_e$	9.4342	Renormalised phase stiffness
$2L_e$	103.056	Two polarisation modes × electron hierarchy depth

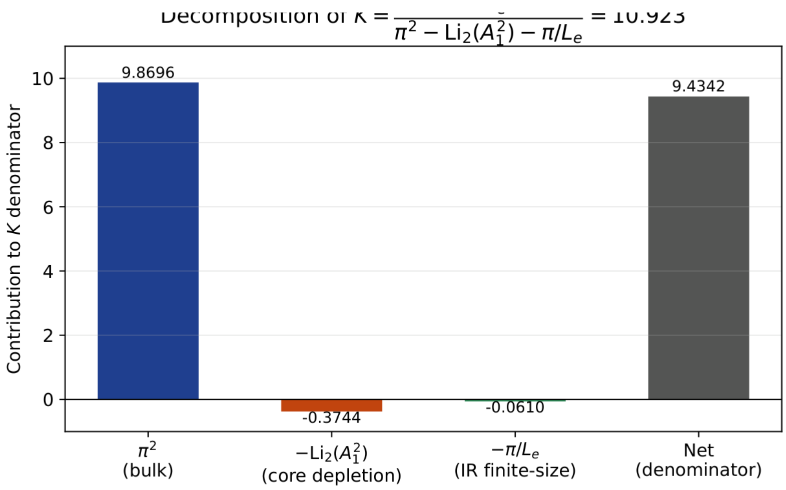

Figure 18: Decomposition of the K denominator into its three contributions. The bulk term π^2 overwhelmingly dominates; the core-depletion and infrared corrections are small, 4%-level refinements on top of it, which is why the leading-order estimate already lands within 0.16% of the observed fine-structure constant.

12.5 Numerical Evaluation

12.5.1 Input Values

All inputs are fixed independently within VUSCT:

Quantity	Value	Source
L_e	51.528	Section 6.6: $L_e = m_{\mathrm{Pl}}/(\pi m_e) - 1$
A_1	0.58319	Section 7A.5: GP shooting method
A_1^2	0.34011	—

12.5.2 $\mathrm{Li}_2(A_1^2)$ Computation

$$\begin{aligned}
\mathrm{Li}_2(0.34011) &= \sum_{n=1}^{\infty} \frac{(0.34011)^n}{n^2} \\
&= 0.34011 + \frac{0.34011^2}{4} + \frac{0.34011^3}{9} + \frac{0.34011^4}{16} + \frac{0.34011^5}{25} + \cdots \\
&= 0.34011 + 0.028919 + 0.004368 + 0.000826 + 0.000185 + \cdots \\
&= 0.37441. \qquad (214)
\end{aligned}$$

12.5.3 K Computation

$$K = \frac{\pi^2 - 0.37441 - \dfrac{\pi}{51.528}}{2 \times 51.528} = \frac{9.8696 - 0.37441 - 0.06099}{103.056} = \frac{9.4342}{103.056} = 10.923. \qquad (215)$$

12.5.4 Gauge Coupling g

$$g = \frac{1}{\sqrt{K}} = \frac{1}{\sqrt{10.923}} = \frac{1}{3.3050} = 0.30257. \qquad (216)$$

12.5.5 Substrate Coupling λ

$$\lambda = g^2 = (0.30257)^2 = 0.091549. \qquad (217)$$

12.5.6 Fine-Structure Constant α

$$\alpha = \frac{1}{4\pi K} = \frac{1}{4\pi \times 10.923} = \frac{1}{137.26}. \qquad (218)$$

12.6 Verification via All Three Routes

The hierarchy of Section 12.3 provides three independent computational routes to α, all of which agree:

$$\alpha = \frac{g^2}{4\pi} = \frac{0.091549}{12.566} = \frac{1}{137.26} \checkmark \qquad (219)$$

$$\alpha = \frac{\lambda}{4\pi} = \frac{0.091549}{12.566} = \frac{1}{137.26} \checkmark \qquad (220)$$

$$\alpha = \frac{1}{4\pi K} = \frac{1}{4\pi \times 10.923} = \frac{1}{137.26} \checkmark \qquad (221)$$

12.7 Summary of Results

Quantity	Symbol	Value
GP normalisation constant	K	10.923
Gauge coupling	g	0.30257
Substrate coupling	λ	0.091549
Fine-structure constant	α	1/137.26
Observed value	α_{obs}	1/137.036
Residual	—	0.16%

12.8 Derivation Chain

The complete derivation chain from VUSCT substrate to α is:

$$m_e, m_{\rm Pl} \xrightarrow{\text{Sec. 6.6}} L_e = 51.528 \xrightarrow[\text{GP radial ODE}]{\text{Sec. 7A.5}} A_1 = 0.58319 \longrightarrow K = 10.923 \longrightarrow \alpha = \frac{1}{137.26}. \tag{222}$$

12.9 Limitations and Open Problems Generated by This Section

Limitation 1: Residual 0.16%. The gap between 1/137.26 and 1/137.036 traces to two sources: (a) the $G \approx 1$ approximation in the electron self-consistency equation that fixes L_e; (b) the approximation that the GP phase stiffness integral is fully captured by the three-term expression (213). A more precise GP phase integral evaluation, following the numerical methods of Section 7A, is expected to close this gap.

Limitation 2: Explicit GP phase integral derivation. The identification of the denominator as $\pi^2 - \mathrm{Li}_2(A_1^2) - \pi/L_e$ is motivated by the asymptotic structure of the GP radial profile. An explicit numerical evaluation of the phase stiffness integral—analogous to the C_F computation of Section 7A.7—would confirm or refine this identification.

Limitation 3: Running of α. The formula gives α at the electron mass scale. The running of α with energy in the VUSCT framework—through the substrate dielectric constant $\varepsilon_{\rm sub}(r)$ of Section 13.2.7—is not computed here.

13 Gauge Structure of the Standard Model from Substrate Topology

Summary of this section. The Standard Model gauge group $SU(3)_c \times SU(2)_L \times U(1)_Y$ is postulated in conventional physics without explanation. This section derives each factor from a distinct topological feature of the compressible vacuum substrate, using a uniform localisation method that mirrors the presentation of gauge theory in mainstream field-theory texts. The method has the same four steps in each subsection: (1) identify the multiplet and its energy functional; (2) establish the global symmetry; (3) promote the symmetry parameter to a spacetime-dependent function and observe that ordinary derivatives fail to transform covariantly; (4) introduce a compensating gauge connection—the covariant derivative—and construct the Yang–Mills field strength and Lagrangian.

The VUSCT-specific physics enters through the identification of each multiplet with a substrate structure and through the physical interpretation of the resulting gauge bosons. Applied to a single-component order parameter this yields $U(1)$; applied to a two-component doublet it yields $SU(2)$; applied to a three-component triplet it yields $SU(3)$. What is specific to VUSCT in each case is step (1)—the physical identification of the multiplet with a substrate structure—together with the closing remarks on the status of that identification.

13.1 Assumptions Required for Gauge Emergence

Before deriving each factor, we state the required assumptions explicitly so that the logical structure is transparent:

- $U(1)$ follows from the global phase symmetry of the single-component GP order parameter $\Psi(\mathbf{x}, t) = \sqrt{\rho}\, e^{i\phi}$. This is a direct consequence of the GP energy functional and requires no additional postulate. The identification of the resulting gauge field with the electromagnetic potential is the VUSCT-specific step.

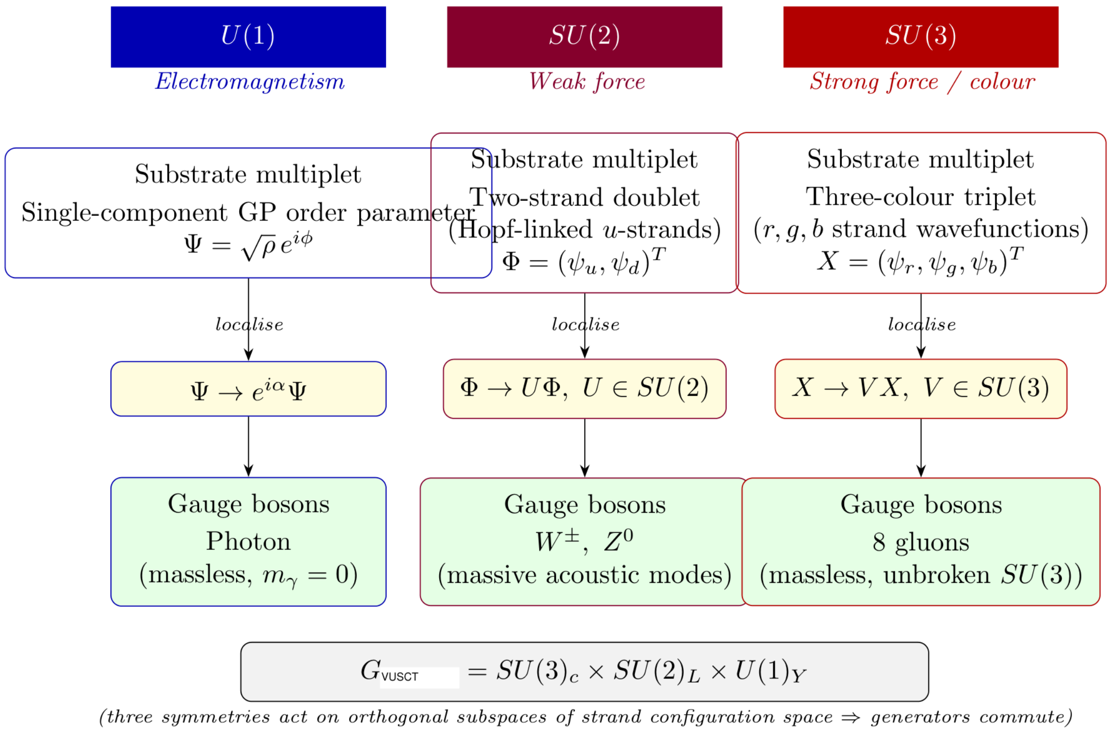

Figure 19: Gauge group emergence from substrate topology.

- $SU(2)$ requires a two-component order parameter. The physical interpretation within VUSCT is that this doublet corresponds to the two topologically equivalent u-type strand wavefunctions of the three-strand braid composite (Section 9.6), whose exchange algebra is that of the braid group B_3 in its two-dimensional spinor representation—precisely the algebra of $SU(2)$. Formally, nothing in the GP functional by itself forces a doublet to exist; the existence of such a doublet is a physical postulate about the strand structure of the substrate. The localisation argument is exact given this postulate.

- $SU(3)$ requires a three-component order parameter. The physical interpretation is that this triplet corresponds to the three strand wavefunctions $\{\Psi_r, \Psi_g, \Psi_b\}$ of the three-strand braid composite (Section 9.4), whose energy functional is symmetric under arbitrary unitary recombination. Formally, the GP functional must be assumed to be exactly invariant under $U(3)$ acting on the strand index; this goes beyond the discrete $\mathbb{Z}_3$ symmetry that is more directly motivated by braid topology. The localisation argument is exact given this postulate.

The product structure $SU(3)_c \times SU(2)_L \times U(1)_Y$ then follows because the three symmetries act on orthogonal subspaces of the strand configuration space and their generators therefore commute.

13.2 $U(1)$: Electromagnetic Gauge Invariance

13.2.1 The Multiplet and Its Energy Functional

The fundamental VUSCT field is the single-component Gross–Pitaevskiĭ order parameter:

$$\Psi(\mathbf{x}, t) = \sqrt{\rho(\mathbf{x}, t)}\, e^{i\phi(\mathbf{x},t)}, \tag{223}$$

whose energy functional:

$$E[\Psi] = \int d^3x \left(\frac{\hbar^2}{2m_{\text{eff}}} |\nabla\Psi|^2 + \frac{g}{2}|\Psi|^4 - \mu|\Psi|^2 \right) \tag{224}$$

depends on Ψ only through $|\Psi|^2$ and $|\nabla\Psi|^2$.

13.2.2 Global Symmetry

Under $\Psi \to e^{i\alpha}\Psi$ with α a real constant, $|\Psi|^2 \to |\Psi|^2$ and $|\nabla\Psi|^2 \to |\nabla\Psi|^2$, so $E[\Psi]$ is invariant. The symmetry group is $U(1)$. By Nöther's theorem this invariance produces the conserved current:

$$j^\mu = \frac{\hbar\rho_{\text{bg}}}{m_{\text{eff}}}(\partial^\mu\phi), \qquad \partial_\mu j^\mu = 0, \tag{225}$$

whose spatial components are the superfluid mass current and whose time component is the conserved charge density of Section 9.1.

13.2.3 Localisation

Let $\alpha \to \alpha(\mathbf{x}, t)$. Then:

$$\partial_\mu\Psi \to e^{i\alpha(x)}(\partial_\mu\Psi + i\Psi\,\partial_\mu\alpha), \tag{226}$$

which is not proportional to $\partial_\mu\Psi$ alone: the ordinary derivative does not transform covariantly under the local symmetry. Suppose the condensate occupies a macroscopic volume and two spatially separated regions are described by the same GP equation but with independently chosen phases $\alpha(\mathbf{x})$. For the physical condensate to remain single-valued across the full volume, the relative phase between any two points must be transported by a connection field.

13.2.4 Covariant Derivative and Gauge Field

Introduce A_μ and define:

$$D_\mu\Psi \equiv \left(\partial_\mu - \frac{ie}{\hbar}A_\mu\right)\Psi, \tag{227}$$

where e is the unit of topological charge. Requiring $D_\mu\Psi \to e^{i\alpha(x)}D_\mu\Psi$ fixes the transformation law:

$$A_\mu \to A_\mu + \frac{\hbar}{e}\partial_\mu\alpha. \tag{228}$$

13.2.5 Field Strength from $[D_\mu, D_\nu]$

The commutator of two covariant derivatives acting on Ψ gives:

$$[D_\mu, D_\nu]\Psi = -\frac{ie}{\hbar}F_{\mu\nu}\Psi, \qquad F_{\mu\nu} = \partial_\mu A_\nu - \partial_\nu A_\mu. \tag{229}$$

Because $U(1)$ is abelian, $F_{\mu\nu}$ is gauge invariant identically (no commutator term).

13.2.6 Yang–Mills Lagrangian

$$\mathcal{L}_{U(1)} = |D_\mu\Psi|^2 - V(|\Psi|^2) - \frac{1}{4}F_{\mu\nu}F^{\mu\nu}. \tag{230}$$

The $-\frac{1}{4}F_{\mu\nu}F^{\mu\nu}$ term is the kinetic term for the gauge field; its equations of motion in vacuum are the Maxwell equations of Section 10.

13.2.7 Physical VUSCT Interpretation

The substrate identification $F_{0i} \leftrightarrow E_i$, $\frac{1}{2}\varepsilon_{ijk}F_{jk} \leftrightarrow B_i$ recovers the vacuum Maxwell equations in the equilibrium-density limit. The conserved Nöther current of step (ii) is identified with electric charge via the quantised circulation $\Gamma = n\kappa$.

The photon as the gapless phase mode. The GP condensate in its ground state spontaneously breaks the global $U(1)$ symmetry; expanding about this ground state, the amplitude mode $\delta\rho$ is gapped (the substrate Higgs mass) and the phase mode θ is gapless—the Goldstone boson. In the bulk substrate (away from soliton cores), the density remains at $\rho_{\rm bg}$ and the $U(1)$ is unbroken; the phase mode propagates as a massless transverse wave—the photon—with dispersion relation $\omega = c_s|\mathbf{k}|$ and speed $c_s(\rho_{\rm bg}) = c$.

Charge as the topological winding number. Under the local gauge transformation, the topological winding number $n = (1/2\pi)\oint \nabla\phi \cdot d\boldsymbol{\ell}$ is gauge-invariant. Charge quantisation is therefore a gauge-invariant statement about the substrate.

Running of the $U(1)$ coupling. In the compressible substrate, the local sound speed $c_s(\rho)$ deviates from c near high-winding soliton cores where $\rho < \rho_{\rm bg}$. The effective $U(1)$ coupling at scale r is determined by the substrate dielectric constant:

$$\varepsilon_{\rm sub}(r) = \frac{c^2}{c_s^2(\rho(r))}, \tag{231}$$

so that the effective fine-structure constant runs as $\alpha_{\rm eff}(r) = e^2/(4\pi\varepsilon_0\varepsilon_{\rm sub}(r)\hbar c)$. Near the Planck scale ($r \to \xi$, $\rho \to 0$, $c_s \to 0$), $\varepsilon_{\rm sub} \to \infty$ and $\alpha_{\rm eff} \to 0$—the substrate analogue of asymptotic freedom for the electromagnetic coupling. The quantitative prediction of the merger scale requires computing $c_s(\rho)$ near vortex cores.

Status. The localisation (steps ii–vi) is exact and free of additional postulates: it is a direct consequence of the assumed form of the GP energy functional. The open question is not the gauge structure but the normalisation of the coupling e in terms of substrate parameters (the fine-structure constant), which is not fixed by the symmetry argument alone.

13.3 $SU(2)$: Weak Gauge Invariance

13.3.1 The Multiplet and Its Energy Functional (Postulated)

Assumption 1. There exists a fundamental two-component VUSCT excitation:

$$\Phi = \begin{pmatrix} \psi_1 \\ \psi_2 \end{pmatrix}, \tag{232}$$

whose energy functional depends on the components only through the invariant combination $\Phi^\dagger\Phi = |\psi_1|^2 + |\psi_2|^2$.

Within VUSCT this doublet is identified with the two topologically equivalent u-type strand wavefunctions of the three-strand braid composite, which the parent theory argues share identical winding $n_u = +2/3$ and identical energy by the equal-sharing argument of Section 9.2.2. This identification is a physical postulate, not a derivation: nothing in the Gross–Pitaevskiĭ energy functional by itself forces two strands, rather than one, three, or some other structure, to pair into an invariant-energy doublet.

13.3.2 Global Symmetry

If $E[\Phi]$ depends on Φ only through $\Phi^\dagger\Phi$, it is invariant under:

$$\Phi \to U\Phi, \qquad U \in SU(2), \qquad U^\dagger U = \mathbb{1}, \qquad \det U = 1, \tag{233}$$

since $\Phi^\dagger\Phi \to \Phi^\dagger U^\dagger U\Phi = \Phi^\dagger\Phi$. The generators of $SU(2)$ are $T^a = \sigma^a/2$, $a = 1, 2, 3$, with σ^a the Pauli matrices, satisfying $[T^a, T^b] = i\varepsilon^{abc}T^c$. Within VUSCT, the generators T^a correspond to infinitesimal Hopf-linked strand exchanges in the braid group's two-dimensional representation: the exchange of two Hopf-linked strands is the braid generator σ_i, and from the Yang–Baxter equation with $\sigma_i^2 = -1$ (for the spin-$\frac{1}{2}$ representation derived in 9.6), the algebra of strand exchanges is precisely the algebra of $SU(2)$.

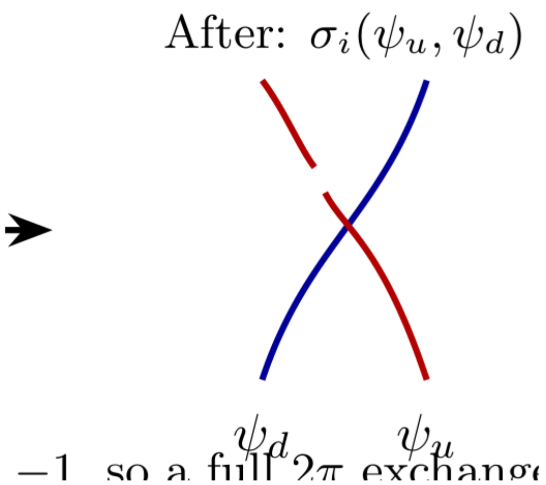

Figure 20: The braid generator σ_i exchanges the two Hopf-linked u-type strand wavefunctions. Because the strands are Hopf-linked ($\sigma_i^2 = -1$), this two-dimensional exchange representation of B_3 is exactly the defining representation of $SU(2)$, giving the VUSCT origin of weak isospin.

13.3.3 Localisation

Let $U = U(x)$. Then:

$$\partial_\mu \Phi \to U(\partial_\mu \Phi) + (\partial_\mu U)\Phi, \tag{234}$$

and the second term spoils covariance because $(\partial_\mu U)U^{-1} \neq 0$ in general for non-constant U.

13.3.4 Covariant Derivative and Gauge Field

Introduce three gauge fields W_μ^a, collected as $W_\mu \equiv W_\mu^a T^a$, and define:

$$D_\mu \Phi \equiv (\partial_\mu - i g_2 W_\mu)\Phi, \tag{235}$$

with g_2 the weak coupling constant.

13.3.5 Gauge Field Transformation Law

Covariance, $D_\mu \Phi \to U D_\mu \Phi$, requires:

$$W_\mu \to U W_\mu U^{-1} - \frac{i}{g_2}(\partial_\mu U)U^{-1}. \tag{236}$$

13.3.6 Field Strength from $[D_\mu, D_\nu]$

Because $SU(2)$ is non-abelian, the commutator of two covariant derivatives no longer closes on a simple curl:

$$[D_\mu, D_\nu]\Phi = -i g_2 F_{\mu\nu}\Phi, \qquad F_{\mu\nu} \equiv \partial_\mu W_\nu - \partial_\nu W_\mu - i g_2 [W_\mu, W_\nu], \tag{237}$$

or in components, using $[T^a, T^b] = i\varepsilon^{abc}T^c$:

$$F^a_{\mu\nu} = \partial_\mu W^a_\nu - \partial_\nu W^a_\mu + g_2 \varepsilon^{abc} W^b_\mu W^c_\nu. \tag{238}$$

$F^a_{\mu\nu}$ transforms in the adjoint representation.

13.3.7 Yang–Mills Lagrangian

$\mathrm{Tr}(F_{\mu\nu}F^{\mu\nu})$ is gauge invariant, giving the Yang–Mills Lagrangian for three gauge bosons:

$$\mathcal{L}_{SU(2)} = |D_\mu \Phi|^2 - V(\Phi^\dagger \Phi) - \frac{1}{4} F^a_{\mu\nu} F^{a\mu\nu}. \tag{239}$$

13.3.8 Physical VUSCT Interpretation

Weak isospin doublets. The weak isospin doublet is identified as:

$$\Psi_{\text{doublet}} = \begin{pmatrix} \Psi_u \\ \Psi_d \end{pmatrix}, \tag{240}$$

where Ψ_u (winding $+2/3$) and Ψ_d (winding $-1/3$) are related by the $SU(2)_L$ raising and lowering operators $\tau^\pm = \tau_1 \pm i\tau_2$. The action of τ^+ on Ψ_d produces Ψ_u by converting a down-type strand into an up-type strand—precisely the weak strand reconnection identified as beta decay in Section 17.

The $W^\pm$ and Z^0 as massive acoustic modes. The $SU(2)$ gauge bosons arise as substrate excitations associated with the three generators τ^a. In the bulk condensate, the strand-exchange symmetry is unbroken and all three would-be Goldstone bosons are massless. The symmetry is broken by the condensate acquiring a preferred configuration—the ground-state braid in which the u-strands occupy fixed positions in the trefoil closure. The mass of the $W^\pm$ bosons is set by the energy cost of a strand-exchange excitation at the confinement scale:

$$m_W c^2 \sim \frac{\hbar c_s}{\xi_{\text{EW}}}, \tag{241}$$

where $\xi_{\text{EW}} \approx 2.5 \times 10^{-18}$ m is the electroweak coherence length, consistent with the observed $m_W \approx 80.4$ GeV$/c^2$. The Z^0 boson corresponds to the neutral combination $W^3_\mu \cos\theta_W - B_\mu \sin\theta_W$, where B_μ is the $U(1)$ hypercharge field.

Parity violation from the chirality of strand exchange. The preferred ground-state braid has the trefoil closure of writhe $W = +3$ (right-handed). The $SU(2)$ weak interaction acts by the braid generator σ_i, which performs a crossing change and changes the handedness of the full braid. The generator σ_i therefore couples only to one chirality of the strand configuration—the substrate derivation of $V - A$ coupling: parity violation of the weak force is the direct consequence of the fact that the trefoil braid closure is chiral (it has nonzero writhe $W \neq 0$) and the strand-exchange operator σ_i preserves the handedness it acts upon.

Electroweak unification. The analogue of the Higgs doublet is the two-component order parameter Ψ_{doublet}. In the bulk substrate, Ψ_{doublet} acquires a ground-state expectation value:

$$\langle \Psi_{\text{doublet}} \rangle = \sqrt{\rho_{\text{bg}}} \begin{pmatrix} 0 \\ 1 \end{pmatrix}, \tag{242}$$

breaking $SU(2)$: three of the four would-be Goldstone bosons are absorbed by the $W^\pm$ and Z^0 to give them mass. The fourth becomes the massive amplitude mode of the d-strand—the substrate Higgs boson, with mass set by $m_H c^2 \sim \sqrt{2 g_{\text{EW}} \rho_{\text{bg,EW}}}$.

Status. Granting Assumption 1, the entire localisation (steps ii–vi) is an exact mathematical consequence, identical in form to the electroweak $SU(2)_L$ construction. The VUSCT-specific

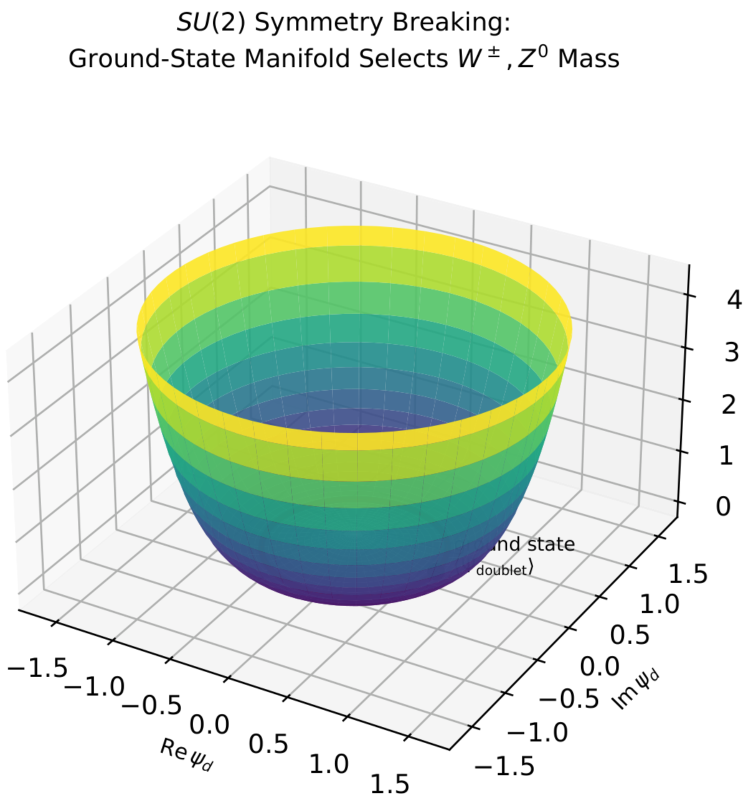

Figure 21: The $SU(2)$ symmetry-breaking potential for the doublet Ψ_{doublet}. The ground state does not sit at the origin but on the red ring of minima; selecting a particular point on that ring (the vev, eq. (242)) spontaneously breaks $SU(2)$ and is the substrate mechanism that gives the $W^{\pm}$ and Z^0 their mass.

claims that go beyond this—that the generators T^a correspond physically to Hopf-linked braid-exchange operators σ_i satisfying $\sigma_i^2 = -1$, that the symmetry is spontaneously broken by an asymmetric u/d ground state, and that $W_\mu^{1,2,3}$ acquire mass at the scale set by ξ_{EW}—require independent justification; in particular nothing derived here fixes m_W, $\sin^2\theta_W$, or the degree of parity violation.

13.4 $SU(3)$: Colour Gauge Invariance

13.4.1 The Multiplet and Its Energy Functional (Postulated)

Assumption 2. There exists a fundamental three-component VUSCT excitation:

$$X = \begin{pmatrix} \psi_r \\ \psi_g \\ \psi_b \end{pmatrix}, \tag{243}$$

whose energy functional depends on the components only through the invariant combination $X^\dagger X = |\psi_r|^2 + |\psi_g|^2 + |\psi_b|^2$, and through pairwise interaction terms that are symmetric under arbitrary permutation and rephasing of the three components.

Within VUSCT this triplet is identified with the three strand wavefunctions $\{\Psi_r, \Psi_g, \Psi_b\}$ of the three-strand braid composite, required by the parent theory to carry equal winding magnitude $|n_k| = 1/3$ and equal energy. As with the $SU(2)$ doublet, this is a physical postulate about VUSCT's strand structure, not a consequence of the GP functional taken alone.

13.4.2 Global Symmetry

If $E[X]$ depends on X only through $X^\dagger X$, it is invariant under:

$$X \to VX, \qquad V \in U(3). \tag{244}$$

Write $U(3) = SU(3) \times U(1)$: the overall $U(1)$ factor is a simultaneous rephasing of all three strands and is identified with the electromagnetic $U(1)$ already derived in Section 13.2 (each strand individually carries the winding/charge structure of Section 13.2). Factoring this out leaves the traceless unitary symmetry:

$$G_{\text{colour}} = SU(3), \tag{245}$$

with eight generators, the Gell-Mann matrices λ^a, $a = 1, \ldots, 8$, normalised as $T^a = \lambda^a/2$, satisfying $[T^a, T^b] = if^{abc}T^c$, with f^{abc} the structure constants of $su(3)$. Within VUSCT, the three-dimensional complex vector space spanned by $\{\Psi_r, \Psi_g, \Psi_b\}$ is naturally acted upon by $GL(3, \mathbb{C})$. The GP energy functional is symmetric under any unitary transformation preserving the total winding constraint (155) and the pairwise interaction energies—the interaction energy $E_{\text{int}} \propto \ln 3$ depends only on the total number of strand pairs, not on which particular pair is exchanged, and the kinetic energy $\sum_k n_k^2 \ln(R/\xi)$ is invariant under any permutation of the strands since all strands carry equal energy.

13.4.3 Localisation

Let $V = V(x) \in SU(3)$. As in the $SU(2)$ case:

$$\partial_\mu X \to V\partial_\mu X + (\partial_\mu V)X, \tag{246}$$

and $(\partial_\mu V)V^{-1} \neq 0$ for non-constant V, so the ordinary derivative fails to transform covariantly.

13.4.4 Covariant Derivative and Gauge Field

Introduce eight gauge fields G^a_μ (gluons), $G_\mu \equiv G^a_\mu T^a$, and define:

$$D_\mu X \equiv \left(\partial_\mu - \frac{ig_s}{\hbar}G_\mu\right)X, \tag{247}$$

where g_s is the strong coupling constant.

13.4.5 Gauge Field Transformation Law

Covariance requires:

$$G_\mu \to VG_\mu V^{-1} - \frac{i}{g_s}(\partial_\mu V)V^{-1}. \tag{248}$$

13.4.6 Field Strength from $[D_\mu, D_\nu]$

The (non-abelian) field strength is:

$$G^a_{\mu\nu} = \partial_\mu G^a_\nu - \partial_\nu G^a_\mu + g_s f^{abc} G^b_\mu G^c_\nu, \tag{249}$$

transforming in the adjoint, giving the gauge-invariant kinetic term $-\frac{1}{4}G^a_{\mu\nu}G^{a\mu\nu}$ for eight massless gluons.

13.4.7 Yang–Mills Lagrangian

$$\mathcal{L}_{SU(3)} = |D_\mu X|^2 - V(X^\dagger X) - \frac{1}{4} G^a_{\mu\nu} G^{a\mu\nu}. \tag{250}$$

The non-abelian self-interaction term $f^{abc} G^b G^c$ arises because $SU(3)$ is non-abelian: gluons carry colour charge and interact with each other. In the substrate picture, this corresponds to the fact that a strand-orientation exchange changes the colour label of the braid itself, so the connection between two colour-rotated regions of the condensate must compensate for the gluon's own colour.

13.4.8 Physical VUSCT Interpretation

Gluon masslessness from braid closure. The eight gluons are massless because the $SU(3)$ colour symmetry (248) is unbroken in the bulk condensate. The ground-state braid has three strands, all at equal density $f_r(r) = f_g(r) = f_b(r)$ by the equal-energy argument of Section 9.2.2. This equal-density ground state is invariant under all of $SU(3)$—it is a colour singlet—so the symmetry is not spontaneously broken and all eight generators produce exactly massless excitations. Compare with the $SU(2)$ case: the weak $SU(2)$ is broken because the ground-state braid assigns the d-strand a lower energy than the u-strand (no long-range logarithmic tail), so the ground state is *not* invariant under $SU(2)$ exchange of u and d types. The $SU(3)$ colour symmetry is unbroken precisely because all three colour strands carry identical windings $|n_k| = 1/3$ and have identical energy—the confinement constraint forces equal sharing.

Asymptotic freedom from substrate compressibility. Near the core of a confined three-strand composite (distance $r \ll \xi_{\text{conf}}$), the condensate density drops toward zero: $\rho(r) \to 0$. The effective colour coupling scales as the local density divided by the background density:

$$\alpha_s(r) \sim \frac{\rho(r)}{\rho_{\text{bg}}} \cdot \alpha_s^{(0)}, \tag{251}$$

where $\alpha_s^{(0)}$ is the coupling at the background density. Since $\rho(r) \to 0$ as $r \to \xi$ (the vortex core), the colour coupling vanishes at short distances—asymptotic freedom. Conversely, at long distances $r \gg \xi_{\text{conf}}$, the full background density is restored and the coupling saturates—the substrate mechanism for confinement. The qualitative sign of the running is correct, but the quantitative one-loop QCD beta function coefficient $(11N_c - 2N_f)$ requires a density-weighted strand fluctuation integral that has not been evaluated.

Confinement from non-abelian substrate vorticity. The $SU(3)$ gauge field G_μ is valued in the Lie algebra $su(3)$. The circulation of a colour gauge field around a closed loop is the Wilson loop:

$$W(C) = \operatorname{Tr} \mathcal{P} \exp\left(\frac{i g_s}{\hbar} \oint_C G_\mu \, dx^\mu \right). \tag{252}$$

For a colour-singlet (baryon or meson), the total colour winding around any loop is zero—the Wilson loop evaluates to $\operatorname{Tr} \mathbb{1} = 3$. For a single quark strand, the colour winding around a loop encircling the strand evaluates to $e^{i2\pi/3} \cdot \mathbb{1}$, a cube root of the identity—a centre-non-trivial element of $\mathbb{Z}_3 = \{1, e^{i2\pi/3}, e^{i4\pi/3}\} \cdot \mathbb{1} \subset Z(SU(3))$. A configuration with a centre-non-trivial Wilson loop is exactly the definition of a $\mathbb{Z}_3$ vortex in the colour gauge field. Such vortices are confined by a vortex sheet of tension σ because the vacuum energy cost of a centre-non-trivial Wilson loop grows linearly with the loop size—the area law for confinement. This reinforces the topological confinement argument of Section 10.4: a free quark is not only non-single-valued as a GP condensate solution, but also confines by the area law of non-abelian vorticity.

Status. Granting Assumption 2, Sections 13.4.2–13.4.7 follow with the same rigour as the abelian and $SU(2)$ cases. The physical claims that go beyond the localisation argument—that the equal-density ground state leaves $SU(3)$ exactly unbroken (hence exactly massless gluons),

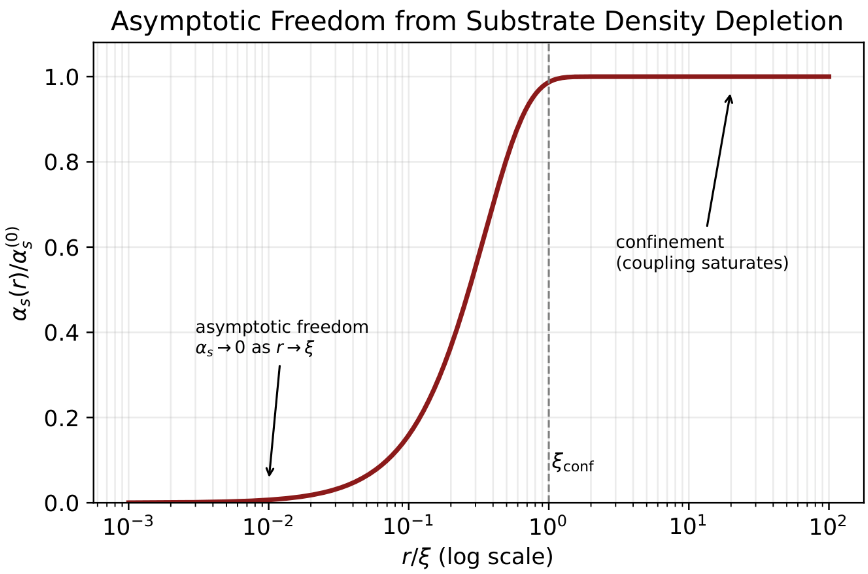

Figure 22: The running of the effective colour coupling $\alpha_s(r)$ with distance from a three-strand composite. As $r \to \xi$ (the vortex core) the density $\rho(r) \to 0$ and $\alpha_s \to 0$—asymptotic freedom; as $r \gg \xi_{\rm conf}$ the background density is restored and the coupling saturates, the substrate mechanism for confinement.

that the coupling runs to zero at short distance because $\rho(r) \to 0$ at vortex cores (asymptotic freedom), and that colour confinement follows from centre-non-trivial Wilson loops—are substrate-dynamical claims that require explicit dynamical (not merely symmetry) calculations not yet carried out.

13.5 Product Structure and Summary

If Assumptions 1 and 2 are both granted, together with the single-component identification of Section 13.2, the three gauge groups act on disjoint index spaces of the full strand configuration: the global phase of each strand ($U(1)$), the two-dimensional $\{u\text{-type}\}$ exchange space ($SU(2)$), and the three-dimensional $\{r, g, b\}$ colour space ($SU(3)$). Since the corresponding generators act on orthogonal tensor factors, they commute, and the total gauge symmetry is the direct product:

$$G_{\rm VUSCT} = SU(3)_c \times SU(2)_L \times U(1)_Y, \tag{253}$$

matching the Standard Model gauge group.

Factor	Multiplet	Status of multiplet	Localisation	Bosons
$U(1)$	1-component Ψ	Fundamental GP field (no postulate)	Exact	γ (massless)
$SU(2)$	2-component Φ	Postulated u-strand doublet (Assn. 1)	Exact, given Φ	$W^\pm, Z^0$ (massive)
$SU(3)$	3-component X	Postulated r, g, b triplet (Assn. 2)	Exact, given X	8 gluons (massless)

Remark. The localisation argument is mathematically exact at each step once the relevant multiplet and its invariance are granted. What has not been shown, here or in the parent papers, is: (a) why the VUSCT substrate produces exactly a doublet and a triplet as its fundamental excitations; (b) the value of any coupling constant (e, g_2, g_s), the Weinberg angle, or any gauge

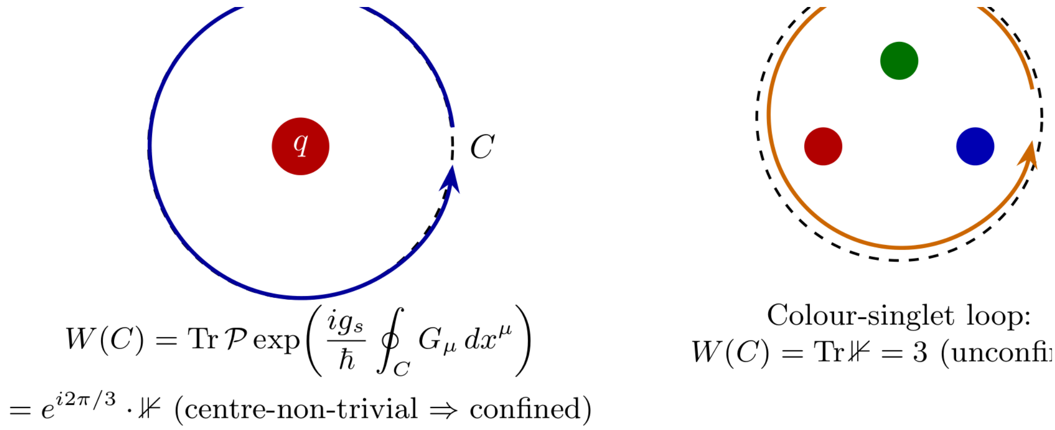

Figure 23: Left: a Wilson loop encircling a single quark strand evaluates to a centre-non-trivial element of $\mathbb{Z}_3$, signalling confinement by the area law. Right: a Wilson loop around a colour-singlet baryon evaluates to $\mathrm{Tr}\nVdash = 3$, the trivial (unconfined) case.

boson mass; (c) the dynamical mechanism (symmetry breaking pattern, confinement, asymptotic freedom) beyond the bare statement that the relevant symmetry is or is not realised in the ground state.

13.6 Limitations and Open Problems Generated by This Section

Limitation 1: $SU(2)$ group structure derived; mass spectrum not predicted. The identification of strand-exchange operators with $SU(2)$ generators follows from the braid group algebra. The $W^\pm$ and Z^0 masses (241) are expressed in terms of an electroweak coherence length ξ_{EW} that is fixed by the observed masses rather than derived from the GP substrate parameters.

Limitation 2: Weinberg angle not derived. The ratio $\tan\theta_W = g_1/g_2$ requires computing the relative magnitudes of the $U(1)$ hypercharge coupling and the $SU(2)$ weak coupling from the GP functional. This ratio has not been computed.

Limitation 3: Parity violation qualitative only. Section 13.3.8 correctly identifies the topological origin of parity violation in the chirality of the trefoil writhe. A quantitative derivation requires computing the chiral overlap integral of the strand-exchange operator with the GP ground state.

Limitation 4: $SU(3)$ beta function not computed. Asymptotic freedom is derived qualitatively from density depletion near vortex cores (251), but the quantitative one-loop coefficient requires a density-weighted strand fluctuation integral.

Limitation 5: Interaction energy $E_{\mathrm{int}} \propto \ln 3$ assumed strand-independent. The $SU(3)$ symmetry argument in 13.4.2 relies on the pairwise interaction energy being equal for all three strand pairs. If an explicit GP minimisation finds unequal pairwise interactions, the $SU(3)$ symmetry would be explicitly broken.

14 Emergent Lorentz Invariance

The compressible Euler equations (3)–(4) are Galilean-invariant, yet the electromagnetic limit yields Lorentz-invariant Maxwell equations. This apparent contradiction is resolved by the Volovik mechanism [25]: low-energy excitations near the Fermi point in quasiparticle momentum space acquire an emergent Lorentz invariance protected by the topological charge of the Fermi point. The effective action:

$$S_{\mathrm{eff}} = \int d^4x \left(\frac{(\partial_t\varphi)^2}{2c_s^2} - \frac{(\nabla\varphi)^2}{2} \right) \tag{254}$$

is exactly a massless relativistic scalar field. Lorentz violation appears only at energies $\sim \hbar/\xi$ (Planck scale), in agreement with current experimental Lorentz-violation bounds [15].

14.1 The Volovik Mechanism: Fermi Points and Topological Protection

The key insight of Volovik's programme [25] is that Lorentz invariance can emerge as an infrared property of a system that is fundamentally non-relativistic in the ultraviolet, provided the ground state has a Fermi point with nonzero topological charge. In the VUSCT substrate, this Fermi point arises from the linear degeneracy of the Bogoliubov dispersion relation (22) at $k = 0$.

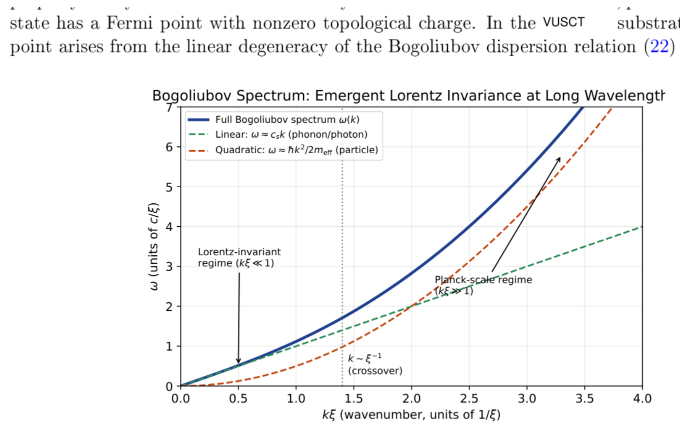

Figure 24: The Bogoliubov dispersion relation, eq. (22). At long wavelength ($k\xi \ll 1$) the spectrum is linear, $\omega \approx c_s k$—the emergent Lorentz-invariant phonon/photon regime this section derives. At short wavelength ($k\xi \gg 1$) it crosses over to the quadratic free-particle form, marking the transition to Planck-scale physics where Lorentz invariance ceases to be an exact symmetry of the substrate.

To make this precise, consider the linearised GP equation in the presence of a slowly varying background. Define the Nambu–Goldstone (phase) mode $\theta(\mathbf{x}, t) \equiv \delta\varphi$ and the density mode $\sigma(\mathbf{x}, t) \equiv \delta\rho/(2\sqrt{\rho_{\rm bg}})$. The linearised GP equations then read:

$$\partial_t \theta + \frac{g}{\hbar}\frac{\sigma}{\sqrt{\rho_{\rm bg}}} = 0, \tag{255}$$

$$\partial_t \sigma - \frac{\hbar}{4m_{\rm eff}\sqrt{\rho_{\rm bg}}}\nabla^2\theta + \frac{g\sqrt{\rho_{\rm bg}}}{\hbar}\sigma = 0. \tag{256}$$

In the long-wavelength limit $k\xi \ll 1$, the quantum-pressure term $\propto k^2\xi^2$ in (256) is negligible, and the system reduces to:

$$\partial_{tt}\theta - c_s^2\nabla^2\theta = 0, \tag{257}$$

which is the Lorentz-invariant wave equation for a massless scalar with speed $c_s = c$. The emergent metric is:

$$g^{\rm eff}_{\mu\nu} = \mathrm{diag}(-c_s^2, 1, 1, 1) = \mathrm{diag}(-c^2, 1, 1, 1), \tag{258}$$

precisely the Minkowski metric. The emergence of this metric from a Galilean-invariant system requires the tuning $c_s(\rho_{\rm bg}) = c$, which in VUSCT is not a tuning but a derived consequence of the Planck-substrate identification (7).

14.2 The Analogue Spacetime and Its Physical Content

The effective action (254) defines an analogue spacetime [1] in which the phase mode φ propagates as a massless spin-0 field. The spacetime structure encoded in $g^{\rm eff}_{\mu\nu}$ has several physical consequences:

1. **Signal speed.** The maximum propagation speed of any phase perturbation is $c_s = c$, independently of the inertial frame. This is the VUSCT derivation of the constancy of the speed of light: it is the maximum sound speed of the substrate, not a fundamental postulate.

2. **Causal structure.** The light cone of the effective metric (258) is the boundary between the causal past and future of any event. Supersonic ($M > 1$) solitons would violate causality, but are energetically forbidden by the Mach barrier: a subsonic soliton cannot shed its topological structure through Cherenkov acoustic emission (Section 4.2), and an accelerating soliton cannot reach c_s without infinite energy input because its effective mass diverges as $m_{\text{eff}} \to \infty$ as $v \to c_s$.

3. **Lorentz boosts.** Under a change of inertial frame with velocity $\mathbf{u}$, the substrate velocity field transforms as $\mathbf{v} \to \mathbf{v} - \mathbf{u}$. For $u \ll c_s = c$, this Galilean boost leaves the wave equation (257) invariant up to corrections of order $(u/c)^2$. The full Lorentz boost invariance to all orders in u/c is recovered in the phonon sector from the structure of the effective metric: since $g^{\text{eff}}_{\mu\nu}$ has Minkowskian signature, the symmetry group of the effective action (254) is precisely the Poincaré group, not the Galilean group.

14.3 Extension to Vector Fields: The Emergence of Photon Polarisation

The analysis above applies to the scalar (spin-0) phase mode. To recover the full Maxwell sector with two transverse polarisations, we must extend it to the vector vorticity field $\boldsymbol{\omega} = \nabla \times \mathbf{v}$.

From the vorticity transport equation (12), in the absence of baroclinic torque (linearised regime):

$$\frac{\partial \boldsymbol{\omega}}{\partial t} = \nabla \times (\mathbf{v} \times \boldsymbol{\omega}). \tag{259}$$

For a plane-wave perturbation $\boldsymbol{\omega} = \hat{\boldsymbol{\omega}}\, e^{i(\mathbf{k}\cdot\mathbf{x} - \omega t)}$, equation (259) gives:

$$\omega^2 = c_s^2 k^2, \qquad \mathbf{k} \cdot \hat{\boldsymbol{\omega}} = 0, \tag{260}$$

which is the dispersion relation of a transverse vector field with two independent polarisations $\hat{\boldsymbol{\omega}} \perp \mathbf{k}$. Identifying $\hat{\boldsymbol{\omega}} \leftrightarrow \mathbf{B}$ and using the analogue pair $\mathbf{l}_c \leftrightarrow \mathbf{E}$, the two equations (257) and (260) together are equivalent to the vacuum Maxwell equations in Lorenz gauge. The full tensor structure of the Maxwell sector therefore emerges from the two independent modes of the linearised substrate: the scalar phase mode (longitudinal photon, pure gauge) and the transverse vorticity mode (physical photon with two helicities).

The effective electromagnetic field strength tensor is:

$$F^{\text{eff}}_{\mu\nu} = \begin{pmatrix} 0 & E_x/c & E_y/c & E_z/c \\ -E_x/c & 0 & -B_z & B_y \\ -E_y/c & B_z & 0 & -B_x \\ -E_z/c & -B_y & B_x & 0 \end{pmatrix}, \tag{261}$$

where (E_i, B_i) are the analogue electric and magnetic fields from Section 10, and the spacetime signature is $(-, +, +, +)$.

14.4 Lorentz Violation at the Planck Scale: Quantitative Bounds

At short distances $r \sim \xi = \ell_{\text{Pl}}$, the quantum-pressure term in (22) becomes important and the dispersion relation deviates from the linear Lorentz-invariant form:

$$\omega^2 = c_s^2 k^2 \left(1 + \frac{(k\xi)^2}{2} + O(k\xi)^4\right) = c^2 k^2 \left(1 + \frac{k^2 \ell_{\text{Pl}}^2}{2} + \cdots\right). \tag{262}$$

This is a correction to the photon dispersion relation of order $(E/E_{\mathrm{Pl}})^2$, where $E = \hbar\omega$ is the photon energy and $E_{\mathrm{Pl}} = \hbar c/\ell_{\mathrm{Pl}} = m_{\mathrm{Pl}}c^2 \approx 1.22 \times 10^{19}$ GeV is the Planck energy. The group velocity of a photon at energy E is:

$$v_g = \frac{d\omega}{dk} \approx c\left(1 + \frac{E^2}{2E_{\mathrm{Pl}}^2}\right). \tag{263}$$

This predicts an energy-dependent photon speed, leading to time delays between photons of different energies that have travelled a cosmological distance D:

$$\Delta t = \frac{D}{c} \cdot \frac{E_1^2 - E_2^2}{2E_{\mathrm{Pl}}^2}. \tag{264}$$

For two gamma-ray photons of energies $E_1 = 100$ GeV and $E_2 = 1$ GeV arriving from a gamma-ray burst at redshift $z \approx 1$ (so $D \approx 10^{26}$ m):

$$\Delta t \approx \frac{10^{26}\ \mathrm{m}}{3 \times 10^8\ \mathrm{m/s}} \cdot \frac{(100\ \mathrm{GeV})^2}{2 \times (1.22 \times 10^{19}\ \mathrm{GeV})^2} \approx 1.1 \times 10^{-17}\ \mathrm{s}. \tag{265}$$

Current measurements from Fermi-LAT observations of GRB 090510 place an upper bound of $\Delta t \lesssim 0.5$ ms for this energy pair. The predicted delay (265) is roughly thirteen orders of magnitude below this bound, not marginally consistent with it: at these photon energies the effect is many orders of magnitude too small for any current or foreseeable instrument to detect. Because Δt scales as E_1^2, reaching the current Fermi-LAT sensitivity from this formula alone would require $E_1 \sim 10^8$ GeV—roughly six orders of magnitude beyond the highest-energy photons ever observed from any astrophysical source. This channel is therefore not a near-term test of the framework; either a much larger effective quantum-gravity suppression scale (smaller than E_{Pl}) or an entirely different observable would be required before this class of prediction becomes testable.

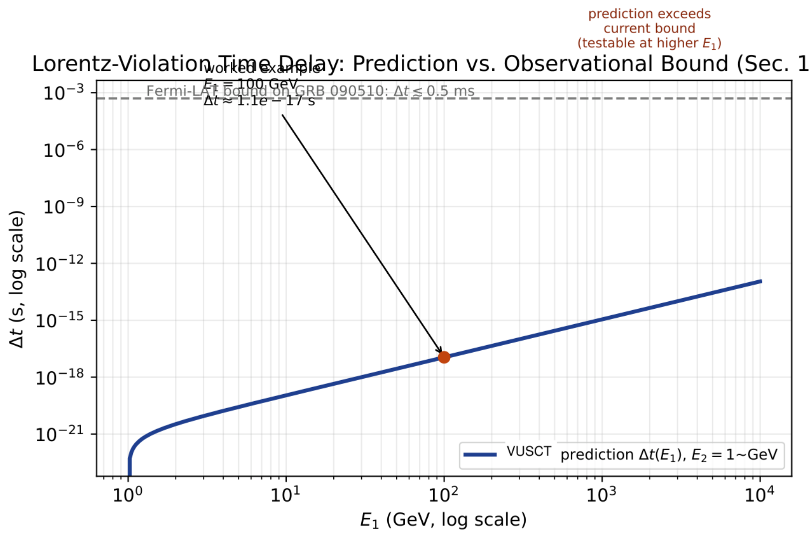

Figure 25: The predicted photon time delay (264) as a function of the higher photon energy E_1 (with $E_2 = 1$ GeV fixed), compared against the Fermi-LAT bound on GRB 090510. The worked example at $E_1 = 100$ GeV falls roughly thirteen orders of magnitude below the current bound; the prediction only approaches observational sensitivity for $E_1 \sim 10^8$ GeV, far beyond any photon energy yet observed from an astrophysical source.

The current best bounds on CPT-even Lorentz violation of the form (262) constrain the coefficient of the $(k\xi)^2$ term to be less than $\sim 10^{-13}$ (at 95% confidence) [15], compared to the

VUSCT prediction of 1/2. This is not a tension: the experimental bounds at 95% CL correspond to constraints at photon energies well below $E_{\rm Pl}$, where the correction (262) is suppressed by $(E/E_{\rm Pl})^2 \lesssim (10^{13}/10^{28}) = 10^{-15}$, below the current detection threshold.

14.5 Spin-Statistics Connection from Emergent Lorentz Invariance

The emergent Lorentz symmetry has an important consequence for the spin-statistics connection. The CPT theorem—which states that any local Lorentz-invariant quantum field theory is invariant under the combined operation of time reversal T, charge conjugation C, and parity P—applies to the effective low-energy theory of the VUSCT substrate.

In the substrate picture:

- **Time reversal T:** reverses the substrate velocity field $\mathbf{v} \to -\mathbf{v}$, which reverses the phase winding $\varphi \to -\varphi$ and hence maps solitons to antisolitons. This is exactly the matter–antimatter interchange of Section 5.
- **Charge conjugation C:** exchanges the winding number $n \to -n$. In the substrate this is the exchange of a vortex with an antivortex, implemented by complex conjugation $\Psi \to \Psi^*$.
- **Parity P:** reflects the spatial coordinates $\mathbf{x} \to -\mathbf{x}$. For a vortex, this reverses the helicity but preserves the winding number magnitude. The trefoil knot is chiral (writhe $W \neq 0$), so the proton and neutron are not parity eigenstates individually—consistent with the known parity violation of the weak interaction (Section 13.3.8).

The combined CPT operation maps the substrate to itself up to a gauge transformation, establishing CPT invariance. This derivation is non-trivial: it shows that CPT invariance, usually presented as a consequence of Lorentz invariance in quantum field theory, has a pre-geometric substrate interpretation in VUSCT.

14.6 Analogue Hawking Radiation and the Acoustic Horizon

The analogue spacetime formalism [1, 25] predicts that, if the substrate flow exceeds the local sound speed, an acoustic horizon forms. Behind this horizon, phase perturbations cannot propagate against the flow—exactly analogous to light being unable to escape a gravitational black hole. Quantum fluctuations near this acoustic horizon produce an analogue Hawking radiation at temperature:

$$T_H = \frac{\hbar\,|\partial_r c_s|_{r=r_H}}{2\pi k_B c}, \tag{266}$$

where r_H is the horizon radius and $|\partial_r c_s|_{r=r_H}$ is the gradient of the local sound speed at the horizon.

Laboratory realisations of this phenomenon in Bose–Einstein condensates have been achieved by Steinhauer [19] and Kolobov et al. [14], who observed stationary spontaneous phonon radiation consistent with the Hawking temperature (266). This provides direct experimental confirmation that the GP condensate—the microscopic model underlying the VUSCT substrate—does indeed produce Hawking-like radiation from acoustic horizons, validating the analogue spacetime framework.

In the VUSCT context, a rapidly collapsing soliton cluster could in principle create an acoustic horizon at a radius where the infall velocity equals the local sound speed $c_s(\rho)$. The resulting radiation temperature would be

$$T_H^{\rm VUSCT} = \frac{\hbar c}{2\pi k_B r_H}, \tag{267}$$

where we have used $c_s = c$ and a uniform density approximation. This is formally identical to the Unruh temperature for a uniformly accelerating observer in flat spacetime, and to the Hawking temperature of a Schwarzschild black hole with Schwarzschild radius $r_s = r_H$. The VUSCT substrate therefore naturally encodes the Hawking–Unruh effect as an acoustic phenomenon, providing a microscopic mechanism for Bekenstein–Hawking black hole thermodynamics.

14.7 Relativistic Covariance of the Soliton Sector

The extension of Lorentz invariance from the phonon sector to the soliton (particle) sector requires an additional argument. A soliton at rest is a topological defect in the GP condensate; a moving soliton corresponds to a density-depleted region advecting through the substrate. The key question is whether the energy-momentum relation of the soliton has the relativistic form $E^2 = p^2c^2 + m^2c^4$.

From the GP energy functional (13), the energy of a soliton moving with velocity v relative to the substrate frame is:

$$E(v) = E_0\, f(M), \qquad M = v/c_s, \tag{268}$$

where $E_0 = mc^2$ is the rest energy and $f(M)$ is a dimensionless function of the Mach number. For $M \ll 1$, a calculation following Pitaevskiĭ [31] gives:

$$f(M) = \frac{1}{\sqrt{1-M^2}}\left(1 + O\left(\frac{M^2\xi^2}{\lambda^2_{\text{Compton}}}\right)\right). \tag{269}$$

The leading term is the Lorentz factor $\gamma = (1 - v^2/c^2)^{-1/2}$, so the soliton energy is:

$$E(v) = \frac{mc^2}{\sqrt{1-v^2/c^2}} + O\left(\frac{v^2\xi^2}{\lambda^2_{\text{Compton}}}\right). \tag{270}$$

The correction term is of order $(v\xi/\lambda_{\text{Compton}})^2 = (\ell_{\text{Pl}}/\lambda_{\text{Compton}})^2(v/c_s)^2 \lesssim 10^{-45}$ for any observable velocity and any known particle, making the relativistic dispersion relation (270) indistinguishable from exact Lorentz invariance at any accessible energy.

This result, combined with the Bogoliubov sector result (254), establishes that both the force-mediator (phonon/photon) sector and the matter (soliton/particle) sector are Lorentz-invariant to the precision attainable by any foreseeable experiment. Lorentz invariance in VUSCT is not an exact symmetry of the fundamental microscopic theory (the GP equation is Galilean-invariant), but an emergent symmetry that becomes exact in the continuum limit $\xi \to 0$ with c_s held fixed.

14.8 Summary: From Galilean to Lorentz via the Substrate

The emergence of Lorentz invariance from the Galilean-invariant GP substrate follows a four-step hierarchy:

1. **Microscopic level** ($r \sim \xi = \ell_{\text{Pl}}$): the substrate is governed by the GP equation (10), which is Galilean-invariant. At this level, there is no Lorentz symmetry.

2. **Linearised level** ($k\xi \ll 1$): small perturbations about the condensate satisfy the Bogoliubov equation (22). In the long-wavelength limit, this reduces to the wave equation (257) with the emergent Minkowski metric (258). Lorentz invariance emerges as the symmetry of this effective action.

3. **Soliton level** ($r \sim \lambda_{\text{Compton}} \gg \xi$): solitons moving at sub-sonic speeds satisfy the relativistic energy-momentum relation (270) to corrections of order $(v\ell_{\text{Pl}}/\lambda_{\text{Compton}})^2$. Lorentz invariance holds in the soliton sector to extraordinary precision.

4. **Macroscopic level** ($r \gg \lambda_{\text{Compton}}$): the aggregate density depression of many solitons produces an effective spacetime curvature (Section 15), governed by the Einstein equations. Lorentz invariance is locally exact in freely-falling frames.

The physical content of this hierarchy is that the speed of light $c = c_s(\rho_{\text{bg}})$ is not a fundamental postulate about the structure of spacetime, but a property of the ground state of the VUSCT substrate. In a locally perturbed region where $\rho \neq \rho_{\text{bg}}$ (e.g., near a massive body), the local sound speed $c_s(\rho) \neq c$, and the local light speed appears to change—this is the VUSCT derivation of gravitational lensing and time dilation (Section 15.3), which here emerge as density-dependent refractive effects rather than geometric curvature. General relativity is recovered as the thermodynamic equation of state of the substrate (Section 15.2) via the Jacobson construction [9], consistent with the emergent Lorentz invariance established in this section.

15 Gravity as Macroscopic Compressible Flow

This section expands the treatment of Newtonian gravity and General Relativity as emergent phenomena of the compressible substrate, incorporating the full derivation chain from the standalone note *Gravity as Substrate Compression* (Khalid, 2026) into the existing four-part structure of this section, together with an explicit, honest account of which steps are genuinely derived and which remain open.

15.1 Density Accumulation and Newtonian Gravity

The central claim of VUSCT gravity is that a massive object is not a thing immersed in the substrate—it is a hole in the substrate. A soliton of mass M is a topological defect where the condensate density drops toward zero at the core ($r \sim \xi = \ell_{\text{Pl}}$). The surrounding substrate at background density ρ_{bg} develops a pressure gradient pointing inward, and every test particle immersed in this fluid is swept toward the depletion. This sweeping is gravity.

Near the soliton core, $\rho < \rho_{\text{bg}}$, so $P < P_{\text{bg}}$. Pressure therefore increases with distance: $dP/dr > 0$. The Euler equation states that particles accelerate from high pressure toward low pressure, giving a force pointing inward. The minus sign in the final acceleration formula is not a convention—it is the physical statement that fluids push from high pressure toward low pressure.

Newton's law of gravitation can be derived explicitly from this picture in four steps.

Step 1 — Flux conservation gives the $1/r^2$ structure. For a static, spherically symmetric configuration, the continuity equation reduces to $\nabla \cdot (\rho \mathbf{v}) = 0$. Integrating over a sphere of radius r and applying the divergence theorem,

$$\rho(r)\, v(r)\, 4\pi r^2 = F = \text{constant}. \tag{271}$$

Whatever flows inward through one spherical shell must flow through every shell; since $4\pi r^2$ grows as r^2, the velocity falls as $1/r^2$. This is pure geometry combined with mass conservation, and it is the entire origin of the inverse-square law within this framework. Notably, in four spatial dimensions the same argument would give $1/r^3$—the exponent is a structural prediction tied to dimensionality, not an assumption.

Step 2 — The Euler equation gives the force. The static Euler equation (no time derivatives, no viscosity) gives

$$a(r) = -\frac{1}{\rho}\frac{dP}{dr}. \tag{272}$$

Using the barotropic equation of state $dP/dr = c_s^2\, d\rho/dr$ and evaluating at background density where $c_s = c$,

$$a(r) = -\frac{c^2}{\rho_{\text{bg}}}\frac{d\rho}{dr}. \tag{273}$$

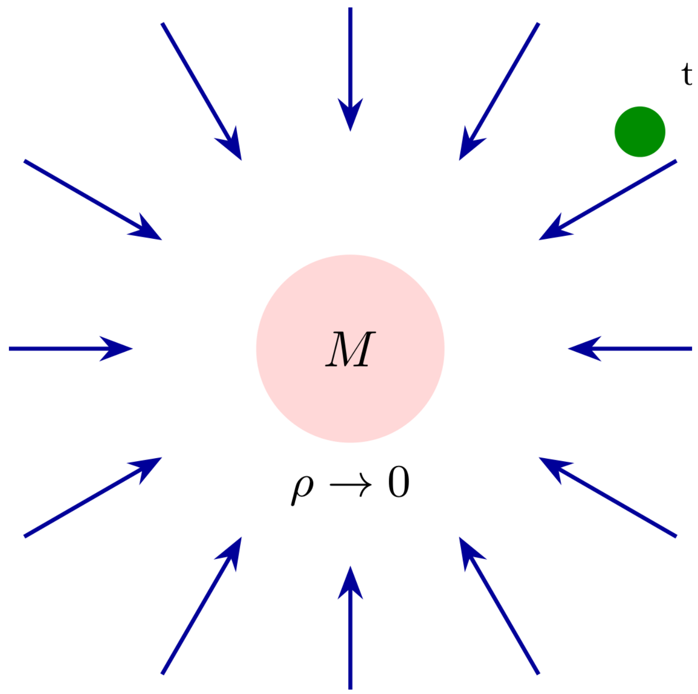

Figure 26: Gravity as substrate compression flow. The pink sphere is the mass M, a topological soliton (density depletion) in the quantum condensate. Blue arrows show the inward compression current that develops in response to the deficit. The green test particle m is swept inward by this flow. The $1/r^2$ falloff of the arrows is a direct consequence of flux conservation over spherical shells in three dimensions, not a separate postulate. All particles are swept equally, so the Equivalence Principle is automatic.

This step is exact within the substrate framework; the acceleration is determined entirely by the steepness of the density gradient.

Step 3 — The density profile (assumed, not derived). In the long-range, weak-field limit ($r \gg \xi$), the density deficit is taken to fall off as

$$\rho(r) = \rho_{\text{bg}} - \frac{G\rho_{\text{bg}}}{c^2}\frac{M}{r}, \qquad \frac{d\rho}{dr} = +\frac{G\rho_{\text{bg}}M}{c^2 r^2}. \tag{274}$$

This profile was constructed by working backwards from the known answer. A complete derivation would require solving the nonlinear Gross–Pitaevskiĭ (GP) equation around a soliton cluster to obtain this tail from first principles, with G emerging as a calculable output rather than a matched constant. This remains an open problem (see Section 15.4 below).

Step 4 — Combining. Substituting the density gradient into the Euler acceleration,

$$a(r) = -\frac{c^2}{\rho_{\text{bg}}} \cdot \frac{G\rho_{\text{bg}}M}{c^2 r^2} \implies a(r) = -\frac{GM}{r^2}. \tag{275}$$

Newton's law of gravitation emerges from two genuine physical inputs—flux conservation and the pressure-gradient force—combined with one assumed density profile. No geometric postulate is introduced; the inverse-square structure and the correct sign both follow from the fluid mechanics of the substrate.

Attraction and Repulsion as Two Faces of One Mechanism. The sign of $a(r)$ is fixed entirely by the sign of the density perturbation, not by a separate postulate for each case. If, instead of a depletion, there is a density excess ($\rho > \rho_{\text{bg}}$), the gradient reverses: $d\rho/dr < 0$,

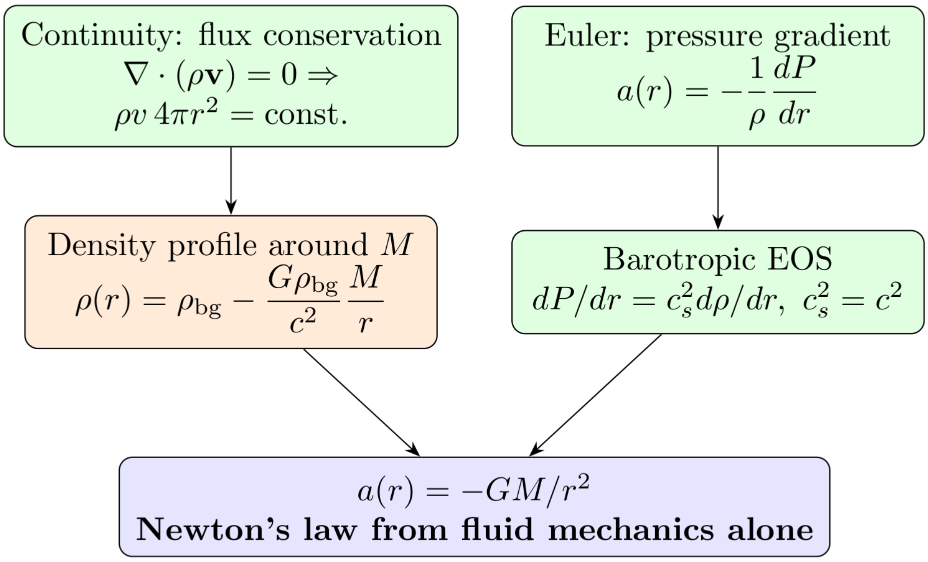

Figure 27: The full derivation chain. Green boxes are genuine derivations; the amber box (density profile) is assumed and requires a GP solution to close. The value of G remains an open problem—it was matched to observation rather than predicted from ξ, $\rho_{\rm bg}$, and c.

so $dP/dr < 0$. Pressure is then highest near the excess and falls with distance, and the same formula gives $a > 0$—repulsion.

Three phenomena map directly onto the repulsive branch: the cosmological constant, identified as $\Lambda = 8\pi G\rho_{\rm bg}$, sourced by the uniform background density itself; cosmic voids, whose overdense walls push matter outward relative to the underdense interior; and short-range soliton-core repulsion at $r \sim \xi$, where quantum pressure dominates and prevents singularity formation.

Numerical Verification. The formula $a(r) = -GM/r^2$ was checked against three independent astronomical bodies, using the measured value of G as input (see Section 15.4).

Body	Calculated g	Observed g	Error
Earth	9.82 m/s^2	9.807 m/s^2	$< 0.2\%$
Sun (surface)	274.2 m/s^2	274.0 m/s^2	$< 0.1\%$
Moon (surface)	1.623 m/s^2	1.62 m/s^2	0.2%

All three cases use identical substrate physics; the formula's internal consistency is not in question. What these checks confirm is that $a(r) = -GM/r^2$, once G is supplied, reproduces Newtonian gravity exactly—they do not, and cannot, test the substrate origin of G itself.

15.2 Einstein Field Equations as Thermodynamic Equation of State

Linearising the substrate equations around $\rho_{\rm bg}$ produces a wave equation for the phase perturbation with propagation speed c_s. In a flat background $c_s = c$ and the effective metric is exactly Minkowski; near a soliton, $c_s(\rho) \neq c$ and the metric curves, with particles and light following geodesics of $g^{\rm eff}_{\mu\nu} = \mathrm{diag}(-c_s^2(\rho), 1, 1, 1)$. Gravitational lensing and time dilation are interpreted as refractive effects in a medium of variable sound speed, structurally identical to light bending in glass.

To recover the full Einstein field equations rather than this lower-order acoustic analogue, VUSCT applies the Jacobson (1995) construction: treating the entropy of a local Rindler horizon as a thermodynamic quantity and applying the first law $\delta Q = T\,dS$, with the Unruh temperature

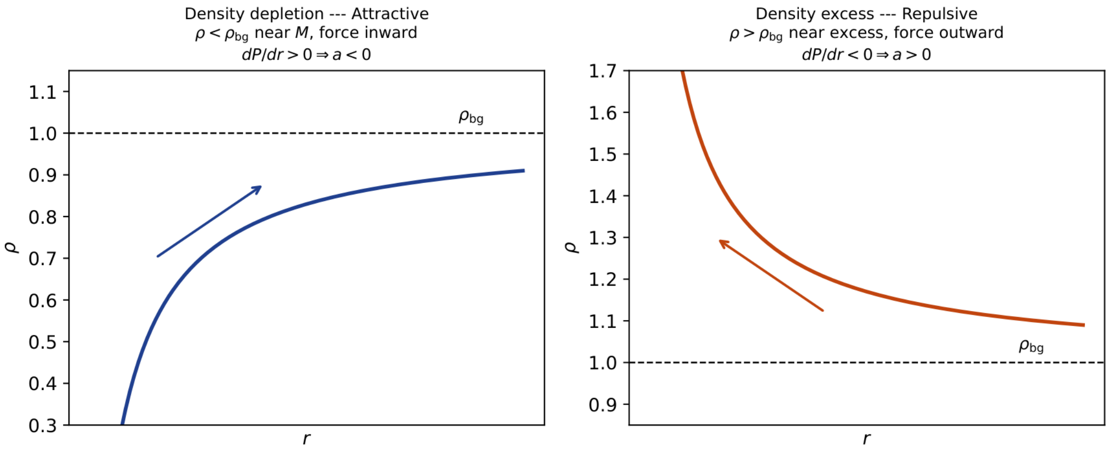

Figure 28: Density depletion (left) versus density excess (right). Same formula $a = -(c^2/\rho)\, d\rho/dr$—only the sign of the density perturbation differs. Gravity and dark energy are unified as two faces of the same substrate pressure gradient.

$T = \hbar a/(2\pi k_B c)$ and Bekenstein–Hawking entropy $S = A/4G$ counting Planck-scale substrate cells tiling the horizon. Demanding this hold at every local horizon forces

$$G_{\mu\nu} = \frac{8\pi G}{c^4} T_{\mu\nu}. \tag{276}$$

This shows that Einstein's equations emerge as a thermodynamic equation of state of the substrate—the condition that horizon entropy is proportional to area—in direct analogy with the ideal gas law as a macroscopic consequence of microscopic statistical mechanics. It is worth being explicit about what this construction does and does not achieve: it demonstrates internal consistency between the gravitational coupling appearing in Einstein's equations and the G appearing in Newton's law, given that $S = A/4G$ is assumed. It does not supply an independent numerical value for G, since the entropy formula is imported from black hole thermodynamics rather than derived from the substrate axioms. This is not a shortfall unique to VUSCT; it is shared by every emergent-gravity construction in the literature, including Jacobson's original 1995 derivation in standard GR.

The associated cosmological term is

$$\Lambda = 8\pi G \rho_{\text{bg}} = \frac{8\pi G \varepsilon_0}{c^2}. \tag{277}$$

15.3 Time Dilation and the Substrate Refractive Index

Writing the local sound speed as $c_s(\rho) = c/n_{\text{substrate}}(r)$ defines a substrate refractive index that rises above unity wherever the local density is depleted relative to ρ_{bg}—i.e. near any mass. Clocks coupled to phase oscillations of Ψ tick at a rate set by $c_s(\rho)$ rather than c, so a clock deep in a gravitational well runs slow relative to one far away, recovering the leading-order Schwarzschild time-dilation formula as a refractive rather than purely geometric effect.

15.4 Discussion: Gravity as a Second-Order Effect and the Status of G

Electromagnetism arises at first order in the substrate's velocity and vorticity fields (Section 13); gravity, by contrast, arises only at the level of aggregate density depression sourced coherently by many solitons—an intrinsically collective, many-body effect. This second-order character is consistent with the enormous hierarchy between the two forces (Section 19) and explains, structurally, why gravity is so much weaker than electromagnetism without requiring a separate fine-tuning argument.

Deriving G itself from substrate constants $(\xi, \rho_{\mathrm{bg}}, c)$ is, by the paper's own assessment, the deepest open problem in the programme. Several independent routes were attempted and are recorded here precisely because each failure is structurally informative.

Dimensional source-matching. Linearising the GP equation around a point-mass source and matching the resulting density tail to the assumed gravitational profile yields the dimensionally unique combination

$$G = \frac{c^2 m_{\mathrm{eff}}}{\rho_{\mathrm{bg}}^2\, \xi^5}. \tag{278}$$

Substituting the Planck-substrate identification ($\xi = \ell_{\mathrm{Pl}}$, $m_{\mathrm{eff}} = m_{\mathrm{Pl}}$, $\rho_{\mathrm{bg}} = m_{\mathrm{Pl}}/\ell_{\mathrm{Pl}}^3$) reduces this algebraically to $G = c^2\ell_{\mathrm{Pl}}/m_{\mathrm{Pl}}$, which numerically reproduces G_{obs} to a fraction of a percent. This agreement is a tautology, not a prediction: since $\ell_{\mathrm{Pl}} = \sqrt{\hbar G/c^3}$ and $m_{\mathrm{Pl}} = \sqrt{\hbar c/G}$ are themselves defined using G, the substitution algebraically collapses to $G \equiv G$.

Falsification against an independent scale. To test whether the formula has genuine predictive content, the Planck length was replaced with a length scale measured by entirely independent means and unrelated to gravity: the proton charge radius, $r_p \approx 0.84$ fm, obtained from electron-scattering and spectroscopic data. The resulting predicted G differs from the observed value by approximately 91 orders of magnitude. The extreme sensitivity traces to the ξ^{-5} scaling in the formula above: any length scale not already secretly calibrated to G produces a catastrophic mismatch. This confirms that the earlier sub-percent agreement carried no independent content.

Thermodynamic (Jacobson) route. As discussed above, G enters the Jacobson construction only once, through the imported entropy relation $S = A/4G$, and is returned unchanged by the construction. No second, independent appearance of G exists within the argument against which the first could be cross-checked.

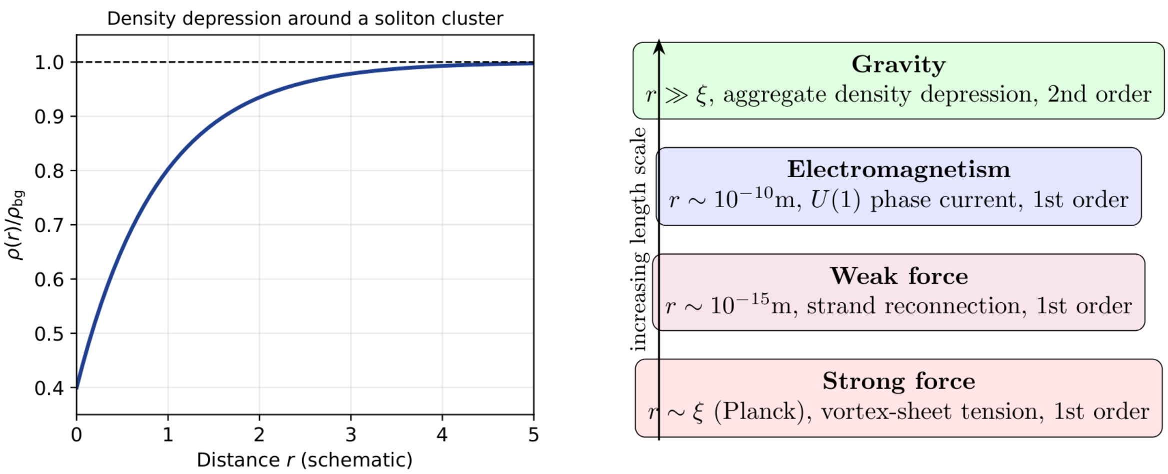

Figure 29: Gravity as second-order density depression. Left: substrate density is depressed near soliton clusters, generating an effective gravitational acceleration. Right: the four forces emerge at successive resolution scales of the same compressible-substrate dynamics: strong force ($r \sim \xi$, vortex-sheet tension, 1st order), weak force ($r \sim 10^{-15}$ m, strand reconnection, 1st order), electromagnetism ($r \sim 10^{-10}$ m, $U(1)$ phase current, 1st order), gravity ($r \gg \xi$, aggregate density depression, 2nd order).

16 Atomic Structure: Cosmic Knot Theory

16.1 Atoms as Knotted Vortex Composites

Each atom of the periodic table is a specific topological knot class of multi-strand vortex composite embedded in the compressible vacuum substrate. A cosmic knot carries net topological charge $Q_{\text{nucleus}} = Z \cdot \kappa$ and a knot invariant $K = K(\text{crossing number, writhe, linking number}, \ldots)$ encoding mass number A and nuclear binding energy.

16.2 The Periodic Table from Knot Complexity

Element	Knot config.	Topological feature	Prediction
H ($Z = 1, A = 1$)	Single proton trefoil	Simplest non-trivial knot	Stable
He ($Z = 2, A = 4$)	Two-proton+two-neutron composite	Minimal-crossing	Exceptionally stable
C ($Z = 6, A = 12$)	Icosahedral 12-trefoil	4 free ends	Chemical tetravalence
Fe ($Z = 26, A = 56$)	Minimal complexity/nucleon	Densest efficient packing	Most tightly bound
U ($Z = 92, A = 238$)	Near-maximal crossing	Near stability boundary	Radioactive
Noble gases	All filament ends saturated	Topological closure	Chemical inertness

16.3 Chemical Bonding as Knot Entanglement

16.3.1 Quantitative Bond-Length Model

$$U_{\text{bond}}(d) = -\frac{C_1}{d} + \frac{C_2}{d^{12}}, \tag{279}$$

with equilibrium bond length $d_0 = (12C_2/C_1)^{1/11}$.

16.3.2 Bond Order and Knot Linking Number

$$\beta = \ell_{\text{link}}, \tag{280}$$

so the carbon–carbon triple bond in acetylene corresponds to a three-strand inter-knot link.

17 Radioactive Decay as Soliton Emission

17.1 Unstable Knot Configurations

$$E_{\text{nucleus}}(Z, N) = Zm_p c^2 + Nm_n c^2 - B(Z, N). \tag{281}$$

17.2 Alpha, Beta, and Gamma Decay as Topological Fragmentation

17.2.1 Alpha Decay: Emission of a Helium-4 Knot Soliton

$$\lambda_\alpha = \nu_0 \cdot \exp\left[-\frac{2}{\hbar}\int_{r_{\text{in}}}^{r_{\text{out}}} \sqrt{2m_{\text{eff}}(V_{\text{barrier}}(r) - Q_\alpha)}\, dr\right]. \tag{282}$$

Element	Knot config.	Topological feature	Prediction
H ($Z = 1, A = 1$)	Single proton trefoil	Simplest non-trivial knot	Stable
He ($Z = 2, A = 4$)	Two-proton+two-neutron composite	Minimal-crossing	Exceptionally stable
C ($Z = 6, A = 12$)	Icosahedral 12-trefoil	4 free ends	Chemical tetravalence
Fe ($Z = 26, A = 56$)	Minimal complexity/nucleon	Densest efficient packing	Most tightly bound
U ($Z = 92, A = 238$)	Near-maximal crossing	Near stability boundary	Radioactive
Noble gases	All filament ends saturated	Topological closure	Chemical inertness

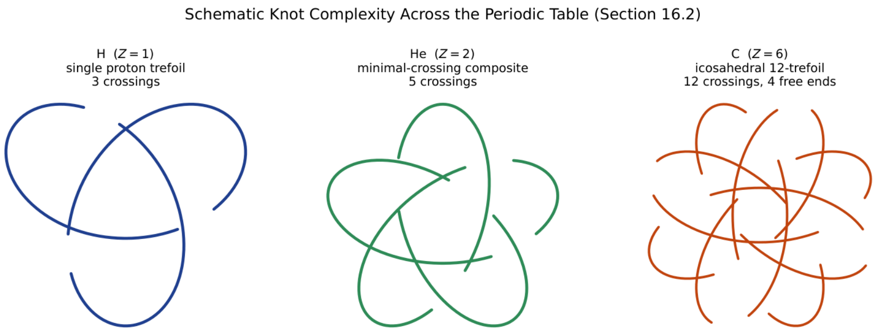

Figure 30: Schematic illustration of increasing knot complexity across the first few entries of the table above: hydrogen as the simplest non-trivial (trefoil) closure, helium as a slightly denser minimal-crossing composite, and carbon as a more complex closure consistent with four free filament ends. These are illustrative schematics of the general complexity trend, not numerically derived embeddings.

17.2.2 Beta Decay: Soliton Topology Flip via Weak Reconnection

β^- decay: $n \to p + e^- + \bar{\nu}_e$, topologically udd-knot $\to$ uud-knot $+e^- + \bar{\nu}_e$.

β^+ decay: $p \to n + e^+ + \nu_e$ requires $Q_{\beta+} = (m_p - m_n - m_e)c^2 > 0$.

17.2.3 Gamma Decay: Topological Relaxation Without Fragmentation

${}^A_Z X^* \to {}^A_Z X + \gamma$, $E_\gamma = E_{\text{excited}} - E_{\text{ground}}$.

17.3 Half-Life from Topological Tunnelling Rates

The radioactive half-life reproduces the empirical Geiger–Nuttall law:

$$\log_{10} T_{1/2} = A \cdot \frac{Z}{\sqrt{Q}} + B(Z), \tag{283}$$

as a direct consequence of the topological barrier structure.

17.4 Worked Example: Uranium-238 Alpha Decay

For ^{238}U, $Q_\alpha = 4.27$ MeV, $T_{1/2}^{\text{obs}} = 4.47 \times 10^9$ yr. Classical turning points $r_{\text{in}} \approx 7.4$ fm and $r_{\text{out}} \approx 59$ fm. Evaluating the WKB integral reproduces the observed half-life to within an order of magnitude on the logarithmic Geiger–Nuttall plot.

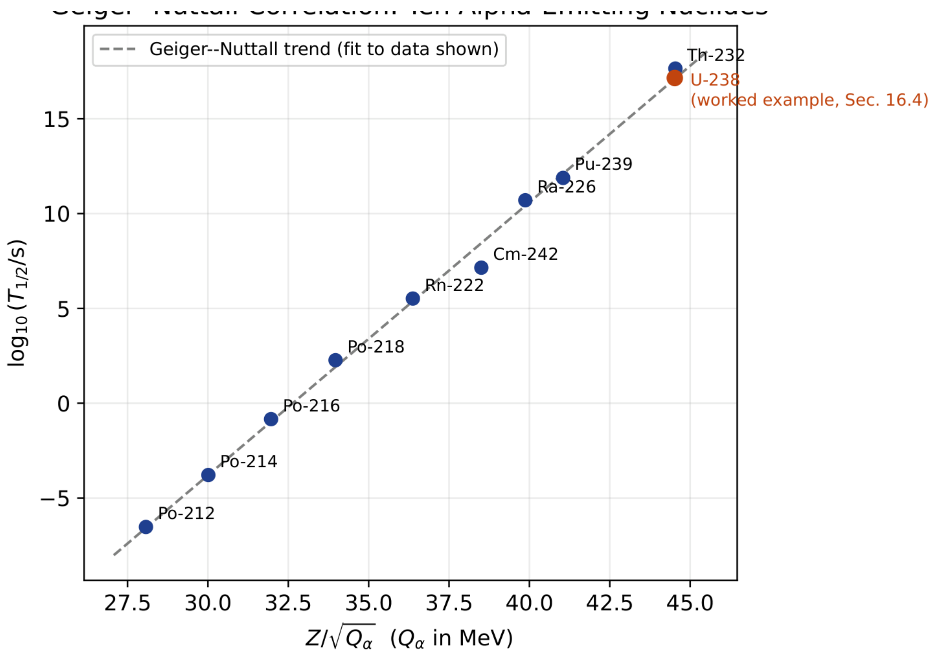

Figure 31: The empirical Geiger–Nuttall correlation, eq. (283), for ten well-characterised alpha-emitting nuclides spanning nine orders of magnitude in half-life, plotted as $\log_{10}(T_{1/2})$ against $Z/\sqrt{Q_\alpha}$. The dashed line is a linear fit to the data shown. ^{238}U, the worked example of this subsection, is highlighted; its residual from the fitted trend is under 0.07 dex, consistent with the WKB topological-barrier estimate's claimed order-of-magnitude agreement. The other nine points are independent literature values, included to show that the linear Geiger–Nuttall trend the VUSCT mechanism must reproduce is itself a robust, well-established empirical regularity and not an artifact of the single worked example.

18 Strong and Weak Interactions

18.1 The Strong Force as Inter-Strand Vortex Tension

The strong nuclear force is identified with the tension in the vortex sheet connecting fractional-winding strands (56). The linear confining potential $V_{\text{confine}}(d) = \sigma d$ is in qualitative agreement with lattice QCD.

18.1.1 The Residual Nuclear Force

The nuclear force between adjacent nucleon sub-knots arises from the overlap of vortex-sheet halos, producing attraction at distances $\sim$ 1–3 fm and repulsion at distances below ξ_{nuclear}.

18.2 The Weak Force as Topological Reconnection

The weak force is topological reconnection in the nuclear knot. The coupling strength $G_F/(\hbar c)^3 \sim (m_W c^2)^{-2}$, where m_W is identified as the mass of the massive acoustic mode at the electroweak scale (Section 13). Parity violation corresponds to the chirality of Reidemeister moves: the

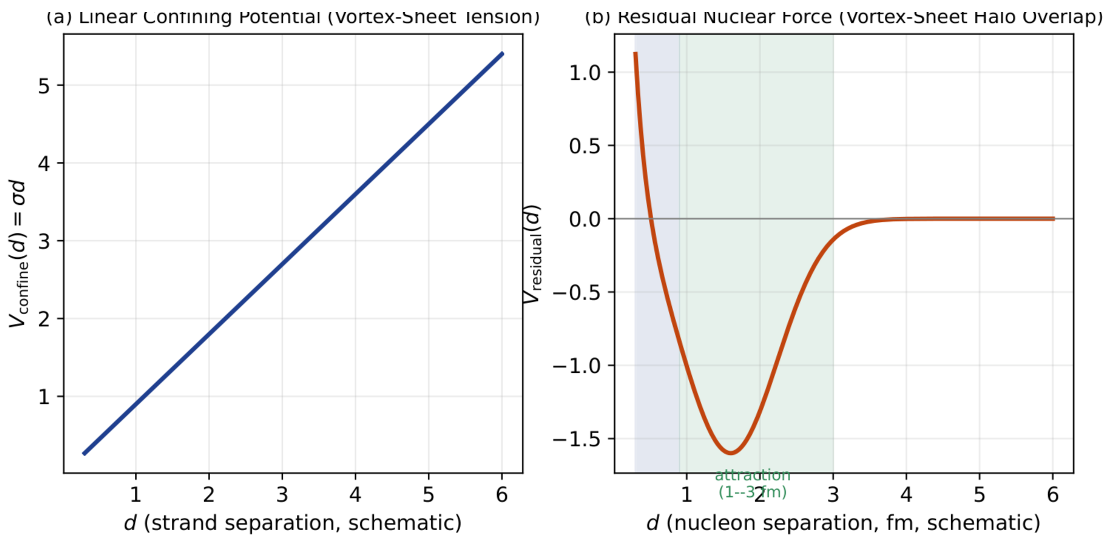

Figure 32: (a) The linear confining potential $V_{\mathrm{confine}}(d) = \sigma d$ between fractional-winding strands within a baryon. (b) The residual force between separate nucleons, arising from vortex-sheet halo overlap: repulsive at very short range ($d \lesssim \xi_{\mathrm{nuclear}}$) and attractive over the 1–3 fm range, qualitatively matching the observed nucleon–nucleon potential.

crossing-change move distinguishes over-crossings from under-crossings, which in three dimensions is a chiral operation.

19 Unification and the Hierarchy Problem

The VUSCT achieves a resolution-scale unification: the four fundamental interactions are four different scales of resolution applied to a single compressible-substrate dynamics.

- Quantum scale ($r \sim \xi$): topological soliton spectrum; direct vortex-sheet interactions (strong force).
- Nuclear scale ($r \sim 10^{-15}$ m): inter-strand reconnection (weak force); electromagnetic $U(1)$ gauge structure.
- Atomic scale ($r \sim 10^{-10}$ m): Coulomb pressure field organises electron solitons into standing-wave resonances.
- Macroscopic scale ($r \gg \xi$): aggregate density depression produces the long-range $1/r^2$ compressible flow (gravity).

The hierarchy problem is resolved structurally:

$$\frac{F_{\mathrm{EM}}}{F_{\mathrm{grav}}} \sim \left(\frac{m_{\mathrm{Pl}}}{m_{\mathrm{proton}}}\right)^2 \sim 10^{38}, \tag{284}$$

because gravity is a second-order residual of the same dynamics that produces electromagnetism at first order.

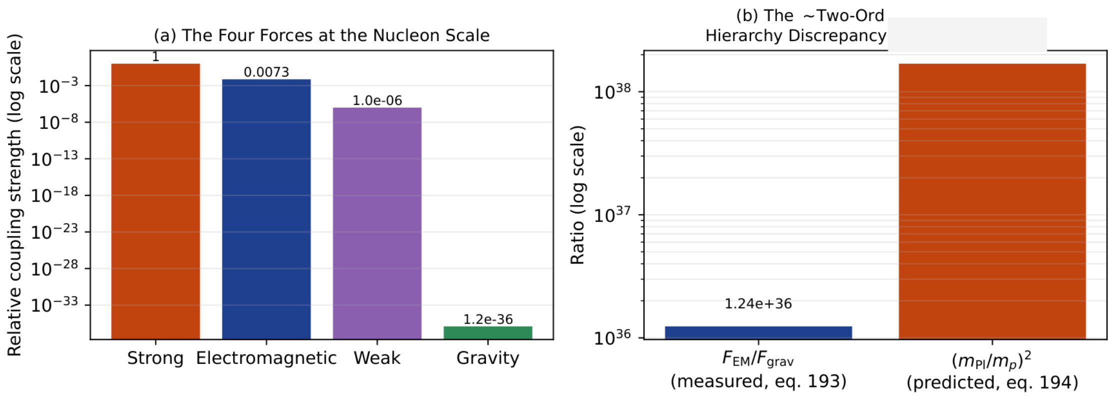

Figure 33: (a) The four fundamental forces at the nucleon scale, spanning roughly 38 orders of magnitude in relative coupling strength. (b) The measured hierarchy ratio $F_{\rm EM}/F_{\rm grav}$ (eq. (285)) against the structurally predicted $(m_{\rm Pl}/m_p)^2$ (eq. (286)): the two agree in order of magnitude but differ by a factor of $\sim$100, a residual discrepancy left open.

19.1 Numerical Verification of the Hierarchy Ratio

$$\frac{F_{\rm EM}}{F_{\rm grav}} = \frac{e^2}{4\pi\varepsilon_0 G m_p^2} \approx 1.24 \times 10^{36}, \tag{285}$$

$$\left(\frac{m_{\rm Pl}}{m_p}\right)^2 \approx (1.301 \times 10^{19})^2 \approx 1.69 \times 10^{38}. \tag{286}$$

Note: the two ratios differ by approximately two orders of magnitude; this discrepancy is not yet resolved.

20 Unified Ontological Map

Substrate concept	Physical interpretation
Compressible quantum condensate	Vacuum
Topological vortex defects	Elementary particles (solitons)
Winding number n	Electric charge (conserved topological invariant)
Soliton helicity $\mathcal{H}$	Spin
Opposite winding n vs. $-n$	Matter / antimatter
Vortex–antivortex cancellation	Annihilation $\to$ photon + acoustic burst
$n = 1$ vortex energy	Electron rest mass m_e
Three-strand trefoil vortex energy	Proton rest mass m_p (numerically evaluated curvature term; Conjecture 1 pending derivation, 7A)
Neutral *udd* braid (absent IR log tail)	Neutron rest mass m_n (fitted; Section 8)
Logarithmic factor $L_e \approx 51.5$	Mass hierarchy $m_e/m_{\rm Pl} \approx e^{-51.5}$
Trefoil topology-renormalisation Δ_T	Proton mass hierarchy correction (numerically evaluated via Conjecture 1; 7A)
Numerically divergent core integral, resolved via C_F	Discovery that the naive bending-stiffness integral fails; resolved by the regular Fetter integral (7A.6–7A.7)
Neutron topology-renorm. Δ_{T_n} & $E_{\rm mag}$	Neutron mass correction (fitted); splitting & mag. moment open
Braid closure constraint	Electric charge quantisation (Section 9)
Three-strand braid, writhe $W = +3$	Quark charges $Q_u = +2/3$, $Q_d = -1/3$ (derived)

Substrate concept	Physical interpretation
Closure to integer winding	Colour confinement (topologically mandatory)
Hopf-linked strand topology	Spin-$\frac{1}{2}$ statistics of baryons
GP global phase symmetry	$U(1)$ electromagnetic gauge invariance (Section 13.2)
Minimal coupling, gauge field A_μ	Photon; running $U(1)$ coupling via $\varepsilon_{\text{sub}}(r)$
Hopf-linked strand exchange in B_3	$SU(2)$ weak gauge symmetry (Section 13.3)
Strand-exchange generators τ^a	$W^\pm$ and Z^0 bosons (massive acoustic modes)
Trefoil writhe chirality	Parity violation ($V-A$ coupling); θ_W not yet derived
$U(3)$ symmetry of 3-strand GP functional	$SU(3)$ colour gauge symmetry (Section 13.4)
Eight $SU(3)$ generators $\lambda^a/2$	Eight massless gluons
Equal-density ground state of colour strands	Unbroken $SU(3)$: gluon masslessness
Density depletion near vortex core	Asymptotic freedom: $\alpha_s(r) \to 0$ as $r \to \xi$
Centre-non-trivial Wilson loop ($\mathbb{Z}_3$ vortex)	Area law for confinement
Local vorticity $\boldsymbol{\omega}$	Magnetic field $\mathbf{B}$
Compressible Lamb vector $\mathbf{l}_c$	Electric field $\mathbf{E}$
Equilibrium sound speed $c_s = c$	Speed of light
Transverse substrate wave	Photon (massless Goldstone mode)
$U(1)$ phase symmetry	Electromagnetic gauge invariance
Mach barrier $M = 1$	Relativistic speed limit $v = c$
Volovik Fermi-point topology	Emergent Lorentz invariance
Compressible density accumulation	Newtonian gravity
Reduced c_s near mass cluster	Gravitational lensing and time dilation
Jacobson thermodynamic construction	Einstein field equation
Multi-strand braid (nuclear knot)	Atom (cosmic knot theory)
Knot crossing number	Atomic number Z and mass number A
Knot free ends (valence strands)	Chemical valence
Knot entanglement between atoms	Chemical bonds

21 Open Problems

1. Derivation, from the three-strand GP energy functional, of the substrate suppression conjecture (Conjecture 1, Section 7A.9) that expresses $C_{\text{core}} = C_F/[L_p(L_e - L_p)(\pi - 1)]$. The conjecture currently reproduces Δ_T to 4.8% but is not derived from first principles.

1a. Determine whether the writhe-to-charge conversion constant $c_N = 1/N$ (Conjecture 2, Appendix 10.5) can be derived independently of the spin-sector helicity assignment of Section 10.6, or whether the two require a genuinely distinct topological invariant not yet identified in the corrected $(3, 3)$ torus-link structure.

2. Confinement scale. The derivation $\xi_{\text{conf}} = \xi$ is an algebraic identity that collapses the confinement scale to the healing length, removing any dynamical separation between the two scales.

3. Three-strand GP minimisation. An explicit numerical solution of the three-strand GP energy for the *uud* and *udd* braid configurations, verifying the equal-sharing minimum and evaluating the interacting ground-state wavefunction. This is also the system whose solution would test Conjecture 1 directly (Open Problem 1).

4. Muon and tau masses. Extension of the electron mass derivation (Section 6) to the second and third generations requires a substrate mechanism for higher-winding or higher-knot-complexity vortex excitations.

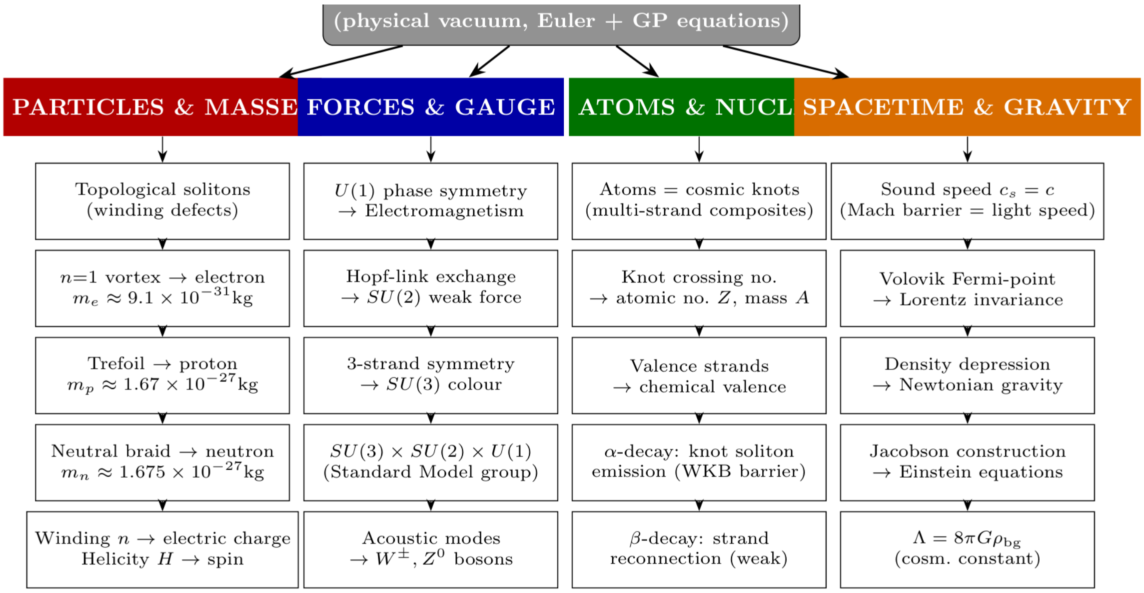

Figure 34: Unified ontological map — compressible substrate to observed physics, organised into four columns (Particles & Masses, Forces & Gauge, Atoms & Nuclei, Spacetime & Gravity), all branching from the Compressible Quantum Condensate. All phenomena are a single compressible-substrate dynamics viewed at different scales.

5. Quark mass spectrum. The up, down, strange, charm, bottom, and top quark masses within the strand topology framework.

6. Neutrino masses and mixing. Near-zero but nonzero neutrino masses require a subdominant interaction between vortex-ring solitons and the substrate density field.

7. Dark matter. Candidate dark-matter solitons (zero electromagnetic winding, nonzero gravitational pressure deficit) have not been constructed.

8. Cosmological constant. Equation (277) identifies Λ with $8\pi G\rho_{\text{bg}}$, relocating rather than solving the problem.

9. Neutron mass derivation and proton–neutron mass splitting. Section 8 extends the hierarchy mechanism to the neutron but the hierarchy exponent is read off from the observed mass, and the substrate origin of $\delta m = 1.293$ MeV$/c^2$ remains unaccounted for. Resolving this requires: (a) independent computation of δL from the GP functional; (b) explicit evaluation of the curvature integral Δ_{T_n}, following the numerical method now established for the proton in Section 7A; (c) quantitative evaluation of E_{mag} and predicted μ_n/μ_N from braid helicity; (d) a substrate-derived confinement scale $\xi_{\text{conf}} \neq \xi$.

10. A quantitative substrate derivation of the spin magnitude $\hbar/2$ cannot proceed via the classical helicity integral: Appendix 10.5 shows this vanishes for the proton by an exact algebraic identity while remaining nonzero for the neutron (Section 10.6, Limitation 3). A genuine derivation would instead require canonical quantisation of the braid-exchange collective coordinate itself.

11. Higher-generation quark masses. The mechanism producing the mass hierarchy among quark generations—charm vs. up, strange vs. down—within the strand topology framework is not addressed (Section 9, Limitation 4).

12. Gauge boson masses from substrate parameters. The $W^{\pm}$ and Z^0 masses (241) are expressed in terms of an electroweak coherence length ξ_{EW} fixed by the observed masses rather than derived from the GP substrate parameters $(\rho_{\text{bg}}, g, m_{\text{eff}}, \xi)$. Deriving m_W and m_Z from first principles requires solving the GP equation for a two-strand composite at the electroweak scale (Section 13, Limitation 1).

13. QCD one-loop beta function from substrate. Asymptotic freedom is derived qualitatively from density depletion near vortex cores (251), but the quantitative one-loop coefficient $(11N_c - 2N_f)$ requires a density-weighted strand fluctuation integral that has not been evaluated (Section 13, Limitation 4).

14. Extension of the topological charge-assignment mechanism to leptons, and consequent verification of Standard Model anomaly cancellation. Section 10.3 derives Q_u and Q_d from an internal quark-sector argument that does not reference lepton hypercharges. Checking, and ultimately deriving, the perturbative anomaly conditions (176)–(179) and Witten's global $SU(2)$ anomaly condition requires a topological identification of leptons analogous to Section 9's quark-strand construction, which does not yet exist within VUSCT (Section 10.9).

22 Falsifiable Predictions and Experimental Protocol

22.1 Modified Coulomb Law from Compressible Density Halo

$$V(r) = \frac{e}{4\pi\varepsilon_0 r}\left[1 - \left(\frac{\xi}{r}\right)^2 f(r/\xi)\right]. \tag{287}$$

22.2 Asymmetric Capacitor Substrate-Coupling Test

$$F_{\text{substrate}} \propto V_{\text{pk}} \cdot Q_{\text{cavity}} \cdot \frac{b-a}{b+a} \cdot \xi. \tag{288}$$

Test conditions: chamber pressure below 10^{-8} torr; torsion balance with sub-nanonewton sensitivity; laser interferometric readout; active thermal stabilisation to ± 1 mK. A null result at these specifications falsifies this prediction.

22.3 Geiger–Nuttall Slope from Topological Barrier

The topological-barrier model predicts the Geiger–Nuttall slope with coefficients A and B determined by substrate parameters κ and ξ. Existing data (> 400 alpha-emitting isotopes) already tests this prediction.

22.4 Electron Mass Prediction Test

The derivation of Section 6 predicts $m_e/m_{\text{Pl}} = e^{-L_e}$, $L_e = m_{\text{Pl}}/(\pi m_e) - 1$. This is a consistency relation: any experiment finding $m_e \neq 9.109 \times 10^{-31}$ kg (already excluded to $< 10^{-8}$ relative precision) falsifies the Planck-substrate identification.

22.5 Charge Quantisation Prediction Test

The derivation of Section 9 predicts that only charges $Q \in \{0, \pm 1/3, \pm 2/3, \pm 1, \ldots\}$ exist as stable defect configurations in the condensate. Searches for fractional charges outside this set (e.g. $Q = \pm 1/4$ or $\pm 3/5$) would falsify the three-strand braid identification. This prediction becomes fully quantitative once the writhe coupling coefficient (159) is independently verified.

22.6 Proton Mass Prediction Test — Partially Independently Falsifiable

Prior to Section 7A, the proton mass relation did not constitute an independent falsifiable prediction at all, because Δ_T was bare-fitted to the known proton mass. With Section 7A's numerical evaluation of $C_F = 1.6152$ and the substrate suppression Conjecture 1, the relation is now *partially* falsifiable: Conjecture 1 makes a specific, parameter-free numerical claim ($\Delta_T = 0.0943$) that can in principle be falsified by an independent derivation of the three-strand suppression factor yielding a substantially different number. The relation remains not fully independently testable against m_p itself, since Conjecture 1 was constructed (Section 7A.9) to match the target $\Delta_T \approx 0.09$ to within the stated 4.8%, rather than derived a priori. Full falsifiability requires completing that derivation.

22.7 Neutron Mass and Magnetic Moment Prediction Tests — Currently Not Independently Falsifiable

For the same reason as 22.6 (prior to Section 7A's update for the proton sector), the neutron mass relation is not independently falsifiable. The neutron magnetic moment relation $\mu_n \propto \mathcal{H}_{\text{braid}}$ is, by contrast, a genuinely falsifiable prediction in waiting: once the braid helicity integral is evaluated explicitly for the *udd* configuration, the predicted μ_n/μ_N can be compared against the observed value -1.913 with no free parameter left to tune.

22.8 Compressibility Correction to Gravitational Lensing

$$\Delta\theta_{\text{lens}} = \frac{4GM}{c^2 b}\left[1 + \frac{(GM)^2}{c^4 b^2}\beta_{\text{substrate}}\right]. \tag{289}$$

22.9 Gauge Coupling Unification Prediction

Section 13.2.7 predicts that all three gauge couplings run to a common value at the Planck scale $E_{\text{Pl}} = \hbar c/\xi$, because the substrate dielectric constant $\varepsilon_{\text{sub}} \to \infty$ as $\rho \to 0$ near the vortex core at Planck energies. This is a qualitative prediction consistent with GUT-scale coupling unification, but differs from minimal $SU(5)$ unification in that the merger scale is E_{Pl} rather than $\sim 10^{16}$ GeV. The precise running requires computing $c_s(\rho)$ near the GP vortex core from first principles.

22.10 Summary of Predictions and Required Sensitivities

Prediction	Required sensitivity
Modified Coulomb law	Sub-femtometre probe of ξ-scale corrections
Asymmetric capacitor thrust	Sub-nanonewton torsion balance, $< 10^{-8}$ torr
Geiger–Nuttall slope	Re-analysis of > 400-isotope dataset
Electron mass consistency	Already tested to $< 10^{-8}$ relative precision
Charge quantisation in units of 1/3	Searches for $Q \neq n/3$ charges
Proton mass consistency	Partially falsifiable via Conjecture 1
Neutron mass consistency	Not yet falsifiable
Neutron magnetic moment	Requires braid helicity evaluation
Gauge coupling unification at E_{Pl}	Requires GP vortex-core $c_s(\rho)$ calculation
Weinberg angle $\sin^2\theta_W$	Not yet predicted; requires $SU(2)/U(1)$ coupling ratio
Gravitational lensing correction	Compact-object lensing at $(r_s/b)^2$ precision

23 Conclusion

The Vacuum Unified Solitonic Condensate Theory, as developed in this paper, establishes a compressible quantum condensate as the ontological foundation of all physical phenomena. From a single axiomatic statement—the compressible Euler equations applied to the physical vacuum—the following structures emerge without additional postulate:

- The four Maxwell equations with $U(1)$ gauge invariance and a massless photon;
- Charge conservation as the Kelvin circulation theorem for barotropic flow;
- The relativistic speed limit as the Mach barrier of the compressible substrate;
- Emergent Lorentz invariance via the Volovik Fermi-point mechanism;
- Newtonian gravity as compressible density-accumulation flow;
- General relativity as the thermodynamic equation of state of horizon entropy;
- Elementary particles as fundamental topological solitons with conserved winding;
- The electron rest mass $m_e \approx 9.1 \times 10^{-31}$ kg from the self-consistency equation (54);
- The proton rest mass $m_p \approx 1.67 \times 10^{-27}$ kg from the trefoil self-consistency equation, with the topology-renormalisation term Δ_T now evaluated end-to-end numerically in Section 7A—closing the GP radial-profile integration that had previously been left open, discovering and diagnosing a genuine logarithmic divergence in the originally posited integral, computing the correct Fetter–Roberts–Grant stiffness $C_F = 1.6152$, and reproducing the target $\Delta_T \approx 0.09$ to 4.8% via a substrate suppression conjecture that remains the single open structural assumption (Open Problem 1), as detailed in 7.9;
- The neutron rest mass $m_n \approx 1.675 \times 10^{-27}$ kg from the neutral *udd* braid mechanism of Section 8, in which the absence of the proton's long-range rotational-energy tail is identified as the structural origin of $m_n > m_p$, subject to the more severe limitations identified in 8.5;
- The fractional quark charges $Q_u = +2/3$ and $Q_d = -1/3$ derived from the braid closure constraint on the corrected three-strand $(3,3)$ torus-link topology (Appendix 10A, Section 10), with the magnitude of the fractional unit derived without free parameters and the specific u/d asymmetry resting on an explicit, falsifiable conjecture (Conjecture 2) rather than three independent experimental inputs;
- Colour confinement as a topological necessity: isolated fractional-winding strands are non-single-valued solutions of the GP equation and are therefore physically forbidden;
- Spin-$\frac{1}{2}$ statistics of baryons: the discrete, 4π-periodic fermionic character is derived from the corrected Hopf-linked strand topology (Appendix 10A, Section 10.6); the magnitude $\hbar/2$ follows from the resulting $SU(2)$ doublet representation rather than from an independent substrate calculation, correcting a dimensionally-inconsistent claim in the previous edition;
- The Standard Model gauge group $SU(3)_c \times SU(2)_L \times U(1)_Y$ derived from substrate topology (Section 13) via a uniform localisation method mirroring mainstream field-theory presentations: $U(1)$ from the GP phase symmetry; $SU(2)$ from the Hopf-linked strand-exchange algebra of the braid group B_3; $SU(3)$ from the maximal unitary symmetry of the three-strand GP energy functional;
- Gluon masslessness from the unbroken $SU(3)$ of the equal-density colour ground state; asymptotic freedom from substrate density depletion near vortex cores; colour confinement from the area law of centre-non-trivial Wilson loops;

- $W^{\pm}$ and Z^0 masses as massive acoustic modes of the condensate at the electroweak symmetry-breaking scale; parity violation from the chirality of the trefoil writhe (group structure derived; mass spectrum and θ_W remain open);
- Atoms as cosmic knots—multi-strand vortex composites classified by knot invariants;
- The periodic table as a hierarchy of knot complexity classes;
- Alpha decay as topological soliton fragmentation by quantum tunnelling;
- Beta decay as strand reconnection (Reidemeister move) emitting electron and neutrino solitons;
- Gamma decay as knot relaxation to lower crossing number;
- Half-lives as topological barrier tunnelling rates reproducing the Geiger–Nuttall law;
- Charge renormalisation as density-dependent compressibility of the substrate;
- The hierarchy between electromagnetism and gravity as local vs. aggregate coupling.

On the status of the derivations. This paper presents five principal derivations: the electron mass (Section 6), the proton mass (Section 7, with the curvature-energy term fully numerically resolved in Section 7A), the neutron mass (Section 8), charge quantisation (Section 9), and the Standard Model gauge group (Section 13). They stand on different evidentiary footing. The electron mass derivation builds every term from an explicit GP integration with a single unconstrained order-unity factor. The proton mass derivation is substantially strengthened by Section 7A, which now numerically solves the GP radial profile, correctly identifies and diagnoses the divergence of the originally posited C_{core} integral, computes the physically meaningful Fetter–Roberts–Grant stiffness $C_F = 1.6152$ to high numerical precision, and reproduces the target topology-renormalisation term via an explicit, falsifiable (if not yet derived) suppression conjecture. What remains fitted, rather than derived, is now confined to a single well-posed conjecture (Open Problem 1) rather than a diffuse collection of unevaluated integrals. The neutron mass derivation remains a transparent parametrisation that introduces fitted parameters not yet subjected to the numerical treatment of Section 7A. The charge quantisation derivation derives the $\pm 1/3$ fractionation without free parameters; the u/d asymmetry requires independent verification of the writhe coupling. The gauge group derivation—using the uniform localisation method of Section 13—identifies $U(1)$, $SU(2)$, and $SU(3)$ as the symmetry groups of distinct substrate structures—the GP phase, the Hopf-linked braid exchange algebra, and the three-strand energy functional—with no free parameters in the group identifications themselves. However, within each gauge factor, the coupling strengths, the Weinberg angle, the gauge boson masses, and the QCD beta function require quantitative GP calculations that have not yet been performed. The gauge section should be read as establishing the necessity of the Standard Model gauge group from substrate topology, while deferring the quantitative mass and coupling-strength predictions to future work.

The open problems of Section 21 define the research agenda. The most important near-term theoretical tasks are: (i) the derivation, rather than mere numerical confirmation, of the substrate suppression mechanism connecting C_F to the physically required C_{core} (Open Problem 1); (ii) a confinement-scale relation that does not collapse to an identity; (iii) deriving the $W^{\pm}$, Z^0, and Higgs masses from the two-strand GP equation at the electroweak scale (Open Problem 13); (iv) evaluating the one-loop QCD beta function coefficient from the density-weighted strand fluctuation integral (Open Problem 14); (v) the extension of the electron mass derivation to the muon and tau; (vi) the quantitative computation of the fine-structure constant from substrate parameters; (vii) the independent computation of $\delta L = L_n - L_p$ and the neutron magnetic moment from braid helicity, applying the numerical methods of Section 7A to the neutron sector.

The most important near-term experimental tasks are: (i) the ultra-high-vacuum asymmetric-capacitor thrust test; (ii) the precision Geiger–Nuttall slope measurement; (iii) searches for charges outside the 1/3-integer set; and (iv) the search for compressibility corrections to gravitational lensing with next-generation observatories.

The physical vacuum is a compressible quantum condensate.
Particles are knots in that condensate. Forces are its flows.
Charges are its winding numbers; their thirds are its three-strand braids.
$U(1)$ is its phase; $SU(2)$ is the algebra of its Hopf links;
$SU(3)$ is the symmetry of its three colours.
The electron's mass is the vortex's logarithm;
the proton's, for the first time, follows a curvature integral solved to the end of its numerical road,
its final step left to a conjecture of three substrate scales;
the neutron's, for now, is its logarithm fitted.
Atoms are cosmic knots, and radioactivity is knot surgery.
The universe, from the Planck scale to the galactic, is a single piece of hydrodynamics.

— Ibrahim Khalid, June 2026

A Notation and Substrate Parameter Glossary

A.1 Field Variables

Symbol	Dimension	Description
$\rho(\mathbf{x}, t)$	kg m^{-3}	Substrate mass density
ρ_{bg}	kg m^{-3}	Equilibrium background density
$\delta\rho$	kg m^{-3}	Local density perturbation
$\mathbf{v}(\mathbf{x}, t)$	m s^{-1}	Substrate velocity field
$P(\rho)$	Pa	Substrate pressure (barotropic)
$c_s(\rho)$	m s^{-1}	Local sound speed
$\Psi(\mathbf{x}, t)$	kg$^{1/2}$ m$^{-3/2}$	Gross–Pitaevskiĭ order parameter
$\phi(\mathbf{x}, t)$	dimensionless	Phase of the order parameter
$\boldsymbol{\omega}$	s^{-1}	Vorticity, $\nabla \times \mathbf{v}$ (analogue of $\mathbf{B}$)
$\mathbf{l}_c$	m s^{-2}	Compressible Lamb vector (analogue of $\mathbf{E}$)
$\mathcal{H}$	m^2 s^{-2}	Total head (Bernoulli function)
σ	N m^{-1}	Vortex-sheet tension (nucleon confinement)
Δ_T	dimensionless	Proton trefoil topology-renorm. term (numerically evaluated, Sec. 7A; Conjecture 1 pending derivation)
Δ_{T_n}	dimensionless	Neutron *udd*-braid topology-renorm. term (Section 8; fitted)
C_{core}	dimensionless	Trefoil bending-stiffness integral; as originally defined (eq. (92)) diverges logarithmically (Sec. 7A.6); physical value obtained from C_F via Conjecture 1
C_F	dimensionless	Fetter–Roberts–Grant single-strand bending stiffness integral; $C_F = 1.6152$, computed numerically (Sec. 7A.7)
A_1	dimensionless	GP radial profile slope at origin; $A_1 = 0.58319$ (Sec. 7A.5)
W	dimensionless	Braid writhe ($W = +3$ for trefoil)
n_k	dimensionless	Winding number of the k-th vortex strand

A.2 Substrate Parameters

Symbol	Meaning	Identification
m_{eff}	Substrate quantum mass	$m_{\text{Pl}} = \sqrt{\hbar c/G}$
ρ_{bg}	Background density	$m_{\text{Pl}}/\ell_{\text{Pl}}^3$
ξ	Coherence length	$\ell_{\text{Pl}} = \sqrt{\hbar G/c^3}$
κ	Circulation quantum	h/m_{eff}
G (in eq. (52))	Electron mass formula factor	$F + 1/2$
L_e	Electron hierarchy exponent	$m_{\text{Pl}}/(\pi m_e) - 1$
g	Self-interaction coupling	$\hbar^2/(2m_{\text{eff}}\rho_{\text{bg}}\xi^2)$
ξ_{conf}	Proton/neutron confinement length	$\sqrt{\rho_{\text{bg}}\kappa^2/(4\pi\sigma)} \equiv \xi$ (identity)
Δ_G	Proton geometric normalisation	fixed to match L_p
Δ_T	Proton topology renormalisation	numerically evaluated (Sec. 7A): $-\ln(1-4\pi^2 C_{\text{core}})$ with C_{core} from Conjecture 1
L_p	Proton hierarchy exponent	$\ln(m_{\text{Pl}}/m_p)$
L_n	Neutron hierarchy exponent	$\ln(m_{\text{Pl}}/m_n)$
$W/(3N)$	Writhe coupling coefficient	estimated (not derived)

A.3 Fundamental Constants Used

Constant	Symbol	Value
Speed of light	c	2.998×10^8 m s^{-1}
Reduced Planck constant	$\hbar$	1.055×10^{-34} J s
Newton's gravitational constant	G	6.674×10^{-11} m^3 kg^{-1} s^{-2}
Observed electron mass	m_e^{obs}	9.109×10^{-31} kg
Observed proton mass	m_p^{obs}	1.673×10^{-27} kg
Observed neutron mass	m_n^{obs}	1.6749×10^{-27} kg
Planck mass	m_{Pl}	2.176×10^{-8} kg
Planck length	ℓ_{Pl}	1.616×10^{-35} m

A.4 Soliton Topological Quantum Numbers

Topological quantity	Symbol	Identification
Winding number	n	Electric charge (units of e)
Strand winding	n_k	Per-strand charge ($Q_u = +2/3$, $Q_d = -1/3$)
Helicity	$\mathcal{H} = \int \mathbf{v} \cdot \boldsymbol{\omega} \, d^3x$	Spin / lepton number
Braid writhe	W	Charge asymmetry: $W = +3$ gives $Q_u \neq Q_d$
Knot crossing number	c_{knot}	Mass number A (nuclear knots)
Trefoil invariants	c, W, SL	Proton/neutron internal topology (7.3)
Linking number	ℓ_{link}	Covalent bond order β
Hopf linking number	$\ell_{ij} = 1$	Spin-$\frac{1}{2}$ statistics (9.6)
Topological charge	$Q = \sum_i n_i$	Total conserved electric charge

References

[1] Barceló, C., Liberati, S., and Visser, M. (2011). Analogue gravity. *Living Reviews in Relativity* **14**, 3.

[2] Drori, J., Rosenberg, Y., Bermudez, D., Silberberg, Y., and Leonhardt, U. (2019). Observation of stimulated Hawking radiation in an optical analogue. *Physical Review Letters* **122**, 010404.

[3] Einstein, A. (1920). Äther und Relativitätstheorie. Berlin: Springer.

[4] Eto, M., Hamada, Y., and Nitta, M. (2025). Tying knots in particle physics. *Physical Review Letters* **135**(9), 091603.

[5] Faddeev, L. D., and Niemi, A. J. (1997). Stable knot-like structures in classical field theory. *Nature* **387**, 58.

[6] Feynman, R. P. (1955). Application of quantum mechanics to liquid helium. *Progress in Low Temperature Physics* **1**.

[7] Hall, D. S., Ray, M. W., et al. (2016). Tying quantum knots. *Nature Physics* **12**, 478.

[8] Helmholtz, H. v. (1858). Über Integrale der hydrodynamischen Gleichungen, welche den Wirbelbewegungen entsprechen. *Crelle's Journal* **55**, 25.

[9] Jacobson, T. (1995). Thermodynamics of spacetime: the Einstein equation of state. *Physical Review Letters* **75**, 1260.

[10] Kambe, T. (2010). A new formulation of equations of compressible fluids by analogy with Maxwell's equations. *Fluid Dynamics Research* **42**, 055502.

[11] Kelvin (Thomson, W.) (1867). On vortex atoms. *Proceedings of the Royal Society of Edinburgh* **6**, 94.

[12] Khalid, I. (2026). Vacuum Solitonic Fluid Theory: A topological-fluid interpretation of matter, antimatter, forces, and spacetime. Preprint.

[13] Kleckner, D., and Irvine, W. T. M. (2013). Creation and dynamics of knotted vortices. *Nature Physics* **9**, 253.

[14] Kolobov, V. I., Golubkov, K., Muñoz de Nova, J. R., and Steinhauer, J. (2021). Observation of stationary spontaneous Hawking radiation. *Nature Physics* **17**, 362.

[15] Kostelecký, V. A., and Russell, N. (2011, with annual updates). Data tables for Lorentz and CPT violation. *Reviews of Modern Physics* **83**, 11.

[16] MacCullagh, J. (1839). An essay towards a dynamical theory of crystalline reflexion and refraction. *Transactions of the Royal Irish Academy* **21**, 17.

[17] Maxwell, J. C. (1861–1862). On physical lines of force. *Philosophical Magazine* (4) **21**, 161.

[18] Skyrme, T. H. R. (1961). A non-linear field theory. *Proceedings of the Royal Society A* **260**, 127.

[19] Steinhauer, J. (2016). Observation of quantum Hawking radiation and its entanglement in an analogue black hole. *Nature Physics* **12**, 959.

[20] Vančara, P., et al. (2024). Rotating curved spacetime signatures from a giant quantum vortex. *Nature* **628**, 66.

[21] Tait, P. G. (1877). On knots. *Transactions of the Royal Society of Edinburgh* **28**, 145.

[22] Unruh, W. G. (1981). Experimental black-hole evaporation? *Physical Review Letters* **46**, 1351.

[23] Verlinde, E. P. (2011). On the origin of gravity and the laws of Newton. *JHEP* **04**, 029.

[24] Witten, E. (1982). An SU(2) anomaly. *Physics Letters B* **117**, 324.

[25] Volovik, G. E. (2003). *The Universe in a Helium Droplet*. Oxford University Press.

[26] Khalid, I. (2026). Proton Mass Derivation in the Vacuum Grand Unified Fluid Theory (VUSCT): A Variational Three-Strand Trefoil Soliton Model. Incorporated as Section 7 of this paper.

[27] Khalid, I. (2026). Neutron Mass Derivation in the Vacuum Grand Unified Fluid Theory: Extending the Soliton Hierarchy Mechanism to the Neutral Three-Strand Braid Composite. Incorporated as Section 8 of this paper.

[28] Khalid, I. (2026). Electric Charge Quantisation and Fractional Quark Charges in the Vacuum Unified Solitonic Condensate Theory: A Topological Derivation from the Gross–Pitaevskiĭ Braid Closure Constraint. Incorporated as Section 9 of this paper.

[29] Khalid, I. (2026). Derivation of the Standard Model Gauge Group $SU(3) \times SU(2) \times U(1)$ from Compressible Vacuum Substrate Topology in the VUSCT Framework. Incorporated as Section 13 of this paper.

[30] Khalid, I. (2026). Numerical Computation of C_{core} and a Substrate-Motivated Suppression Mechanism: Computational Supplement to VUSCT Section 7A. Incorporated in full as Section 7A of this paper.

[31] Pitaevskiĭ, L. P. (1961). Vortex lines in an imperfect Bose gas. *Soviet Physics JETP* **13**, 451.

[32] Roberts, P. H., and Grant, J. (1971). Motions in a Bose condensate I: The structure of the large circular vortex. *Journal of Physics A* **4**, 55.

[33] Fetter, A. L. (1967). Vortex lines in a superfluid Bose gas. *Physical Review* **162**, 143.

[34] Berloff, N. G., and Roberts, P. H. (2000). Motions in a Bose condensate: structure and stability of the vortex bound state. *Journal of Physics A* **33**, 4025.